universität wien

MASTERARBEIT / MASTER'S THESIS

Titel der Masterarbeit / Title of the Master's Thesis

Semi-automatic documentation of PV-plant inspections using GNSS RTK and IMU modules through multidimensional Kalman filtering

verfasst von / submitted by

Paul Dreher, BSc

angestrebter akademischer Grad / in partial fulfilment of the requirements for the degree of

Master of Science (MSc)

Wien, 2017 / Vienna, 2017

Studienkennzahl lt. Studienblatt / degree programme code as it appears on the student record sheet:	A 066 876
Studienrichtung lt. Studienblatt / degree programme as it appears on the student record sheet:	Masterstudium Physik
Betreut von / Supervisor:	Ass.-Prof. Dr. Viktor Schlosser

Acknowledgement

I would like to thank my supervisor from AIT Bernhard Kubicek, who is one of the most dedicated and smartest persons I have ever met and who made this thesis and its outcome possible. It has always been a pleasure talking to him about delicate challenges on physics and programming, as he is capable of breaking down the most complex issues to easily understandable relations.

Also, I would like to thank my supervisor from the University of Vienna Prof. Viktor Schlosser who has always been available for my tricky questions and took his time to discuss my precarious subjects with a very helpful attitude.

Special thanks go to my good friend and English student Mathias, who helped me out with some grammatical issues in my work.

I would like to give a high five to my little cousin Lenz, who initially brought me to the idea of using a differential GNSS system and who has always been one of the most curious people around me.

My deepest gratefulness deserve my aunt and close friend Sabine, who has inspired me many times in my life, and most of all my parents, Ingrid and Wolfgang, who have motivated me from my first day with their generous support and loving confidence.

Paul Dreher

Abstract

The aim of this work was to develop a low cost tracking device for thermographic cameras, which could be used for PV plant inspections. As it is very difficult to keep track of similar looking modules, it would be beneficial to know where exactly the pictures were taken and how the camera was orientated in space, to make it possible to backproject the images to a certain plane and build a three-dimensional evaluation geometry. In order to achieve this concept, an inertial measurement unit (IMU) containing several sensors (3d-magnetic, 3d-acceleration, 3d-gyroscope, barometer) was combined with an evolved RTK GNSS system and programmed using Teensy microcontroller boards. Several methods were tested to use the different sensors as navigation tools, furthermore a Kalman filter was developed to compare and improve the barmometric with the RTK altitude measurements.
For a static measurement, position accuracies of $\sigma_E = 0.0050\,m$, $\sigma_N = 0.0046\,m$ and $\sigma_U = 0.0110\,m$ could be reached, but as soon as the camera was moved, many difficulties appeared and the best achievable accuracies were in the range of $\sigma_E = 0.15\,m - 0.30\,m$, $\sigma_N = 0.15\,m - 0.30\,m$ and $\sigma_U = 0.40\,m - 0.80\,m$. Particularly difficult and not achievable was a stable and good GNSS altitude measurement. The magnetic and acceleration measurements were used to evaluate the camera's orientation, and the pictures were turned and projected fairly correctly. The system works and can be used for PV plant inspections where the distance to the modules is supposed not to exceed 5 m. The most significant difficulties remaining are the vulnerability to failures of the magnetic sensor from electromagnetic stray radiation, GNSS altitude measurements and so-called cycle slips which corrupt the carrier phase measurement.

Kurzzusammenfassung

Die Zielsetzung dieser Arbeit war die Entwicklung eines preisgünstigen Ortungssystems für Thermographie Kameras, welches zur Inspektion von PV-Anlagen verwendet werden kann. Da in großen Anlagen mit sehr vielen Modulen eine hohe Verwechslungsgefahr besteht und es schwierig ist den Überblick zu behalten, wäre es wertvoll für jedes aufgenommene Bild zu wissen, wo genau es enstanden ist und wie die Kamera dabei gedreht war. Mit diesen Informationen ist es möglich die Bilder auf eine definierte Fläche rückzuprojizieren und eine dreidimensionale Geometrie als Grundlage der Auswertung zu bauen. Um dieses Konzept zu verwirklichen wurden IMUs (inertial measurement unit), welche sich aus mehreren Sensoren (3D-Magnetometer, 3D-Beschleunigungssensor, 3D-Gyroskop, Drucksensor) zusammensetzen, mit RTK GNSS Systemen kombiniert und über Teensy Mikrocontroller programmiert. Es wurden verschiedene Methoden getestet, um herauszufinden in welchen Kombinationen die Sensoren als Navigationsysteme dienen können. Weiters wurde ein Kalmanfilter entwickelt, welcher die Ausgabe der Höhenmessungen durch das RTK, mit der Höhenberechnung über die Druckmessung vergleicht und gewichtet.
Für statische Messungen konnten Positionsgenauigkeiten von $\sigma_E = 0.0050\,m$, $\sigma_N = 0.0046\,m$ und $\sigma_U = 0.0110\,m$ erreicht werden, wobei diese stark reduziert wurden, sobald die Kamera in Bewegung gesetzt wurde ($\sigma_E = 0.15\,m - 0.30\,m$, $\sigma_N = 0.15\,m - 0.30\,m$ und $\sigma_U = 0.40\,m - 0.80\,m$). Vor allem die Höhenmessung durch das RTK hat sich bei Bewegung als kaum zu bewältigende Aufgabe herausgestellt. Die Magnetfeld- und Beschleunigungsmessungen konnten benutzt werden, um die Orientierung der Kamera zu bestimmen und in Folge die Bilder richtig gedreht rückzuprojizieren. Das System funktioniert und kann für Insepktionen von PV-Anlagen verwendet werden, jedoch nur für kleine Distanzen (bis 5 m) zwischen Kamera und Modulen, da die Ungenauigkeiten sonst zu groß und die Rückprojektionen fehlerhaft werden. Die verbleibenden signifikanten Schwierigkeiten setzen sich aus der Fehleranfälligkeit des Magnetfeldsensors auf elektromagnetische Streustrahlung, der Ungenauigkeit in der Höhenmessung und den auftretenden Phasensprüngen in der Auswertung der differentiellen Phasenmessung der GNSS Signale zusammen.

Abbreviations

(D)GPS	(Differential) Global Positioning System
CS	Cycle slip
DOP	Dilution of Precision
GNSS	Global Navigation Satellite System
IMU	Inertial Measurement Unit
INS	Inertial Navigation System
IRT	Infrared thermography
MEMS	Microelectromechanical system
MP	Multipath
PV	Photovoltaic
RTK	Real time kinematic
SBAS	Satellite Based Augmentation System

Nomenclature

α	Total absorbtance (irradiation)
ϵ	Released energy from surface
θ	Angle between $\vec{J}$ and $\vec{M}$
μ	Mean value
$\hat{\xi}$	Parameter vector (image transformation)
$\varrho_{\parallel}$	Parallel component of resistivity
$\varrho_{\perp}$	Perpendicular component of resistivity
σ	Standard deviation
σ_E	Standard deviation of horizontal position (east)

σ_N	Standard deviation of horizontal position (north)
σ_U	Standard deviation of vertical position
ψ	Electron wave function
w	Weighing factor
Ω	Angular velocity tensor
C	Atmospheric temperature gradient ($0.65\,K/100m$)
DoG	Difference of Gaussians
$\vec{g}$	Gravitational acceleration ($9.807\,ms^{-2}$)
$h(p)$	Altitude as a function of pressure
$I(x, y)$	Image point
$\vec{J}$	Electrical current
k	Kalman gain
$L(x, y, \sigma)$	Scale space of picture
M	Mean molar mass of atmospheric gases ($0.02896\,kg\,mol^{-1}$)
$\vec{M}$	Internal magnetization
m_i	Affine rotations, scales and stretches
$\vec{p'}$	Central projection
R	Universal gas constant ($8.314\,JK^{-1}mol^{-1}$)
S_l	Local system
$s(t)$	Position of two times integrated acceleration
S_g	Global system
T	Translation matrix
$\vec{x_g}$	Unit vector of global IMU system in x-direction
$\vec{y_g}$	Unit vector of global IMU system in y-direction
$\vec{z_g}$	Unit vector of global IMU system in z-direction

Contents

1 Introduction

Planet earth is on the move for an energy revolution while renewable energies are becoming more and more important. Photovoltaic (PV) plays a major role in this global change and will be one of the major energy sources at the end of the 21st century. The annual global installed capacity is rising every year. In 2015, 50 GW of solar PV were installed, which is equivalent to an estimated 185 million solar modules. Germany, China and Japan are the top contributors to the global installed capacity, see Fig. 1.1, where Austria still has a lot of potential for expansion [1]. In 2014 a total capacity of 785,25 MW was installed in Austria. The positive aspect is that the market is stable and growing about 160 MW annualy [2].

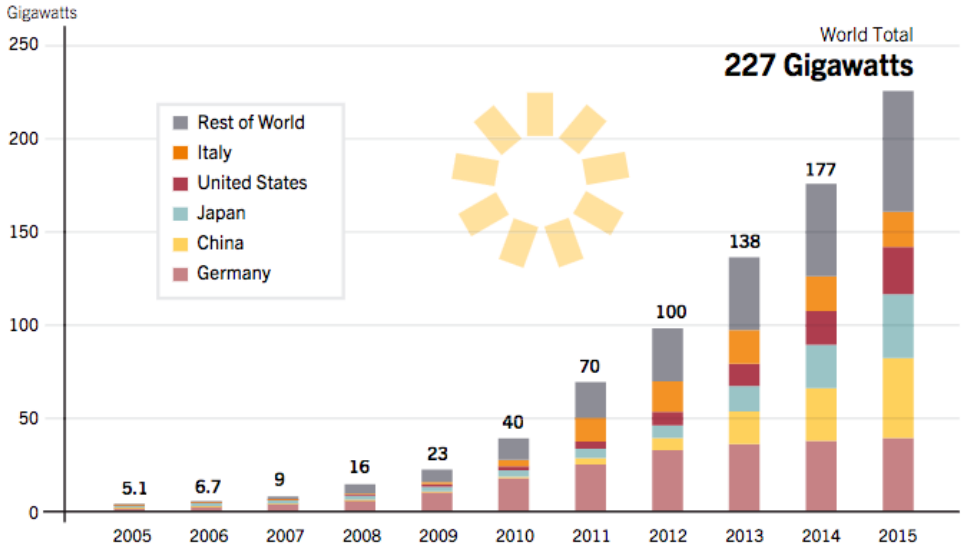

Figure 1.1: The annual growth of PV capacity for different areas on earth [1].

For that reason, it is very important to develop better and more efficient instruments to control and monitor the performance of photovoltaic systems, especially for large photovoltaic power plants, which can contain several ten thousands of modules. With the worldwide energy demand increasing, the PV plants sizes are also going to increase a lot in the future.

At the day of writing this thesis, PV plant inspections are very inconvenient, as inspectors are passing through the modules using visible, thermal and photographic imaging systems and simultaneously have to note which exact module and solar cell corresponds to the module or the cell in a given thermography or photo. This is usually done by a second person, who has the challenging task to locate landmarks in the uniformly built PV park. The standard size of a solar cell is 156 mm square. Hence it is very difficult to get accurate location determinations, even if the cameras are equipped with conventional global navigation satellite system (GNSS) devices, their position resolution is only in the range of 2-10 m and therefore not good enough

to pinpoint individual cells.

In order to guarantee long lifetimes of PV modules in the range of 20 years, it is essential to perform quality inspections repetitively, change defect cells, and by that, avoid downtimes of the systems and ensure maximum power output over their lifetimes. Theoretically, it would be possible to mark every single module with an identifier, hence it would be achievable to execute the quality inspections without any GNSS system. In contrast to that, the method developed in this work, has the benefit that no technical requirements or any local conditions have to be provided. That is what makes it unique. It could be used in any PV plant all over the world.

The described circumstances are very significant considering that the largest PV plant in Austria, the 2 MW_p (power output under standard conditions) plant in Guntramsdorf, consists of 8136 modules on an area of around 50,000 m^2. Worldwide China, USA, and India are pushing and building lots of giant PV power plants at the scale of hundreds of MW_p. The largest PV plant worldwide is the Longyangxia Dam Solar Park in China with a capacity of 850 MW_p [3].

Figure 1.2: The 61 MW_p solar park in Denmark contains 250,000 solar modules and is capable of supplying 30,000 private households [4].

1.1 Definition of key concepts

The intention of this work was to build a low cost tracking system, which is capable of storing the tracks, locations and directional information to a SD card and later process it with a computer. This tracking device can be mounted e.g. onto a thermographic camera and by using timestamps from GNSS and camera, position and view direction of the image aquisition times are known. In a 3d visualization envi-

ronment, it is possible to show the satellite or constructions plans in xy-direction as a texture. Using an additional pre-processing step, the plans can be used to define the 3d geometry of the mounting planes of the modules. Using simple projection, the acquired plant images can now be back-projected onto this 3d geometry. This results in a 3d virtual geometry and can serve as a documentation of the plant investigation.

As personal use drones have become increasingly popular, GNSS modules as well as inertial measurement units (IMUs) have become readily available for less than 20 € each. While typical GNSS update frequencies are between 10 and 0.1 Hz, IMUs can be read at 100 Hz. Typically IMUs include 3d-magnetometers, 3d-accelerometers (gravitational vector + acceleration), 3d-gyroscopes, and highly sensitive barometers. It is well known that Kalman filters can be used to increase position accuracy, using defined location information (e.g. barometer, accelerometer, magnetometer) [32, 33, 35, 36]. New readily available microcontroller development boards (e.g. Teensy 3.6, 180Mhz, 256k RAM, floating point support, micro-SD) are powerful enough to directly perform the Kalman filtering. The high resolution track is then stored onto a SD card. All electronics used for this work are low cost components at a total amount of approximately 150 €.

1.2 Structure of the thesis

The following work is divided into a theoretical framework (section 2) at the beginning, which contains the most important concepts and significant mathematical principles for the success of the implementation. In the second part, the electronics are specified and different experimental methods and techniques are represented and discussed (section 3). In addition, the section of methodology also contains the characterization of the different sensor signals and the calibration methods or results, respectively. Further on, the section of results (section 4) is divided into measurements of the developed RTK system, the implemented Kalman filter, the method of integrating acceleration signals, and the combining of pictures at the end. The last part of this thesis consists of a discussion of the results (section 5) and suggestions for improvements, as well as an outlook to possibilities the implemented system could offer (section 6).

2 Theoretical framework

The section is seperated into the fundamental principles of PV cells, the essentials of infrared thermography, and the emerging error sources. Then the theoretical background and measuring principles of the inertial measurement unit and its sensors are explained. At the end of the section the focus lies on the elements and substructures of GNSS and again the very important error sources.

2.1 Photovoltaic cells

In this chapter the basic physics of solar cells are discussed. The explanations mainly follow [5–7].

Semiconductors are capable of absorbing light and passing a portion of the energy to carriers of electrical current, namely the electrons and the holes. In principal, a solar cell separates and collects carriers and causes a current flow into an internal prefered direction. This process is illustrated at the structure of a conventional solar cell in Fig. 2.1. Basically the solar cell acts like a semiconductor diode which absorbs energy in form of photons and converts it to electrical energy [5].

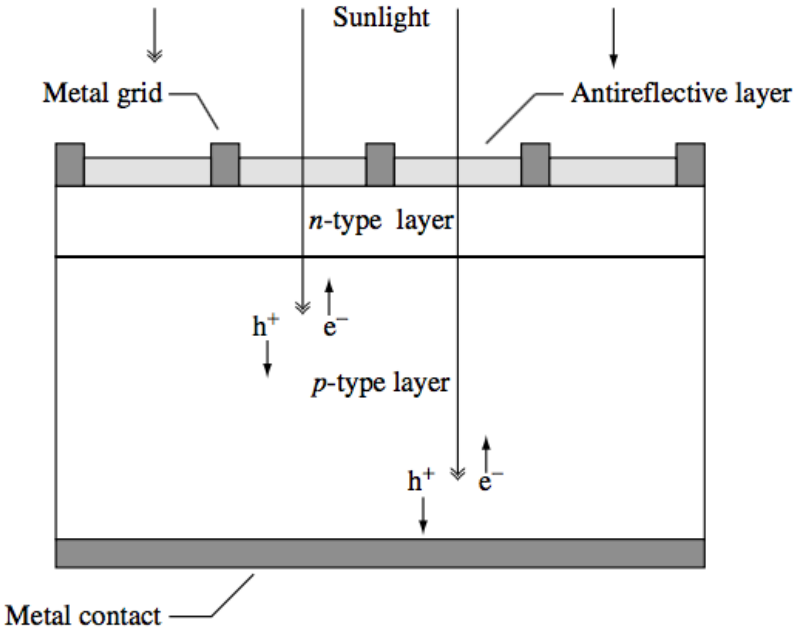

Figure 2.1: The basic components and realisation of a photovoltaic cell involving the creation of electron-hole pairs by the absorption of photons [5].

A metallic grid is used as electrical contacts on the top of the diode. An antireflective layer, implying a gradual change in the effective refractive index, is needed to

guarantee the highest possible amount of photons reaching the semiconductor. It is important to bring together a n-type and p-type semiconductor to form a metallurgical junction, which is explained in section 2.1.1. Usually this is done by diffusion or implementation of impurities, called dopants. On the back of the diode another metallic layer is placed as the second electrical contact.

2.1.1 Energy band structure

An impinging photon to a semiconductor material at an energy of

$$E = h\,\nu\,, \tag{1}$$

larger than the bandgap energy E_G, is capable of exciting electrons from the valence band to condcution band, creating electron-hole pairs. In equation (1) $h = 6.626 \cdot 10^{-34}\,Ws^2$ is the Planck constant and ν the frequency of the photon in Hertz (Hz). The difference of the incoming photon energy and the bandgap energy is lost and wasted in form of heat or thermalisation [7]. A simplified energy band diagram with its characteristics is represented in Fig. 2.2. In a more realistic scenario, like for example it is the case for silicon solar cells, an additional amount of energy has to be transferred to a phonon, to make the transition possible.

Moving electrons in the periodic crystalline structure of semiconductors can be described as confined particles moving in a three-dimensional box, which has a complex structure in consequence of potential fields originating by the component atoms nuclei and tightly bond electrons [5]. The dynamics or the state ψ of the moving electrons can be described by the solution of the time-independet Schrödinger equation

$$\bigtriangledown^2\,\psi + \frac{2m}{\hbar}\,[E - U(\vec{r})]\,\psi = 0\,, \tag{2}$$

where m is the electron mass, E the energy of the electron and U the periodic potential energy inside of the semiconductor depending on position. The equation shall not be solved here, as there are many other very good ressources, for example [8]. The solution of equation (2) describes the band structure of the semiconductor and how the electron is moving inside of the crystall to a good approximation. It has to be considered, that the electron behaves like its mass is not constant within each energy band, therefore the mass has to be exchanged to the parameter of electron effective mass, which is defined as

$$m^* \equiv \left[\frac{d^2E}{dp^2}\right]^{-1} = \left[\frac{1}{\hbar^2}\frac{d^2E}{dk^2}\right]^{-1}\,. \tag{3}$$

In equation (3) $p = \hbar k$ is the crystall momentum and k the wave vector, represented as a scalar for simplicity [5]. The band structure is showed in Fig. 2.2, where the allowed energies of the electrons are plotted against the crystall momentum.

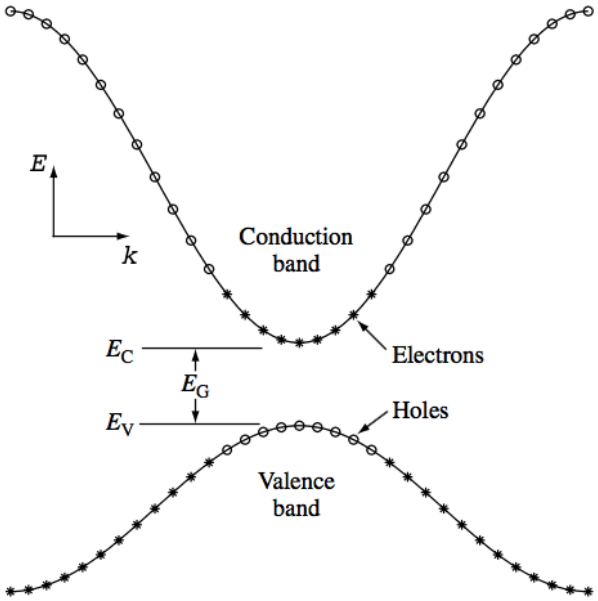

Figure 2.2: The bandgap of a semiconductor at temperature T=0 K in momentum representation. The electrons near the top of the valence band have been excited to the conduction band and have left holes behind [5].

The states are filled from the bottom to the top, where at the top of the valence band they are empty, because some electrons are thermally excited to the conduction band. These empty states, the so-called holes, are regarded as positive charged carriers and follow the same mathematical models as negative charged carriers, but with the opposite sign.

The amount or the densities of electrons (n) and holes (p) in their respective band and therefore the conductivity can be controlled with dopants, that can be donors as well as acceptors. Donors are for example phosphorus impurity atoms in silicon, because phosphorus atoms have five valence electrons and thus one too many in the silicon latice, which is then only poorly bound. Already at room temperature it will detach and move freely inside the silicon semiconductor. The area in the silicon semi conductor is then called a n-doped layer. Similarly, Bor atoms are used as acceptors, because they only have three valence electrons and therefore a free electron hole.

2.1.2 PN-Junction diode electrostatics

Where a n-type semiconductor and a p-type semiconductor get into contact, the pn-junction forms the depletion region for carriers. Because of a surplus of electrons in the n-region and holes in the p-region, they diffuse to the other type of region to compensate the deviation of concentration. As the dopants get uncovered, an electric field is built up, which induces an additional drift current. The diffusion and drift currents balance each other out and there is no net current flow, after

a thermal equilibrium is reached. A resulting electrostatic potential difference is remaining, which is called the built-in voltage V_{bi} [5]. This electrostatic field is necessary to guide the released electrons and holes into the right direction, which is the opposite direction of the diffusion current. The process is illustrated in Fig. 2.3.

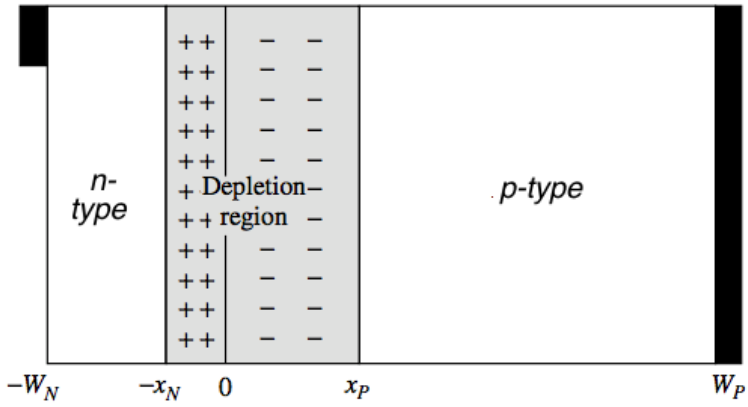

Figure 2.3: Electron and holes have freed themselves from dopants and diffused across the junction (x=0). They left behind ionized donors in the n-area and ionized acceptors in the p-area forming the depletion region and thus an inner electrical field [5].

In summary, it can be stated that the basic solar cell structure is a pn-junction diode containing two quasi-neutral areas on both sides of the depletion region and two metallic contacts on either side to deflect the electrical current. Usually, the region, which is more strongly doped, is called the emitter, where the other quasi-neutral region is called the base. For crystalline silicon, most of the light absorption happens in the base (p-type in Fig. 2.3), where the electrons are freed and lifted to the conduction band.

2.1.3 Solar cell current-voltage (I-V) characteristics

PV cells can be modeled as a current source in parallel to a diode. When there is no light, the PV cell is acting as a diode. At increasing light intensity, current is produced by the PV cell as it is shown in Fig. 2.4. Subfigure (a) represents a typical current-voltage I-V-curve for a simple one diode model, where I_{ph} stands for the photon induced current [9]. In reality, at high voltages, the recombination process in the device is dominated by the bulk regions and the surfaces. At low voltages recombination dominates in the junction. This fact is established in the two diode model and shown in Fig. 2.4 (b). As the goal of this chapter is to explain the theoretical working principles of the solar cell, the one diode model is consulted for further discussions

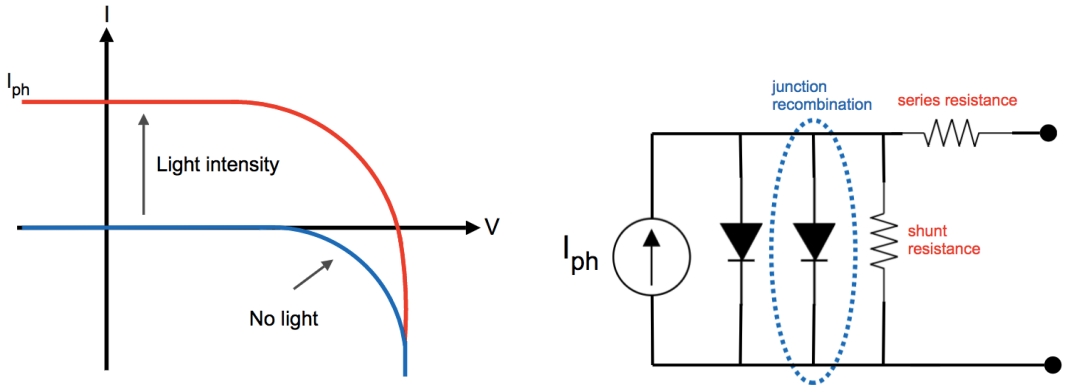

(a) (b)

Figure 2.4: (a) Comparison of two I-V-curves with and without light. (b) Two diode model circuit.

For an ideal cell, the total produced current I is equal to the difference of the photon induced current I_{ph} and the diode current I_d:

$$I = I_{ph} - I_d = I_{ph} - I_0 \left[exp\left(\frac{qV}{kT}\right) - 1 \right] \tag{4}$$

In equation (4) I_0 is the saturation current, q the charge of an electron, k the Boltzmann constant, V the generated voltage and T the cell temperature in K. Another important parameter is the short circuit current I_{sc}. It is the maximal achievable current. For an ideal cell I_{sc} corresponds to I_{ph}. On the other side, there is the open circuit voltage V_{oc} which describes the maximum achievable voltage. It appears when there is no net current flow [9].

What a user is the most interested in, is the maximum power a cell can generate. Power is expressed as $P = I \cdot V$, where the maximum power point P_{max} can be calculated from the $I - V$-curve (see Fig. 2.5). Therefore the current and voltage at this point are defined as I_{mp} and V_{mp}. Another important parameter is the fill factor FF, which is a measure of the quality of the solar cell:

$$FF = \frac{P_{max}}{P_{theo}} = \frac{I_{mp} \cdot V_{mp}}{I_{sc} \cdot V_{oc}} \tag{5}$$

where P_{theo} is the theoretically possible maximal power output. It is graphically illustrated in Fig. 2.5 (b). Typical fill factors are in the range of 0.5-0.82.

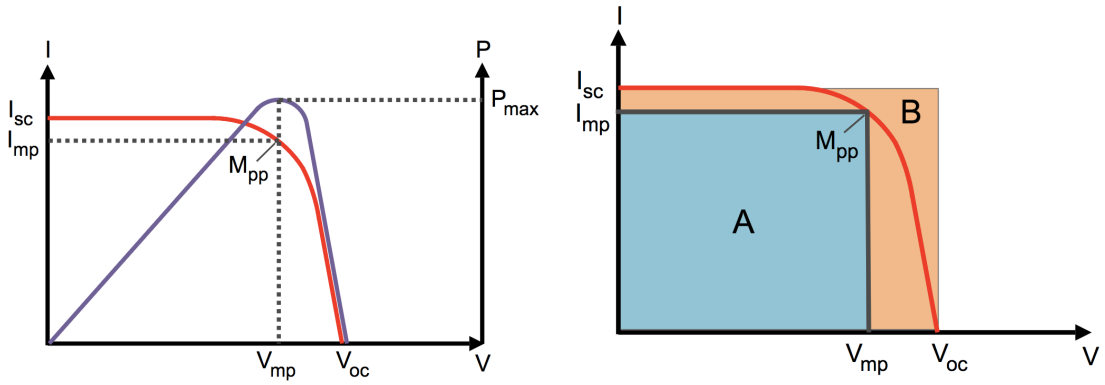

Figure 2.5: (a) The $I-V$-curve (red) and its corresponding power output plot (blue). The illustration on the right side (b) shows the areas of maximal output (blue) and theoretically possible output (orange), which is used to calculate the fill factor.

Probably the most important parameters of a PV cell is the efficiency η. It is defined as

$$\eta = \frac{P_{out}}{P_{in}} \Rightarrow \eta_{max} = \frac{P_{max}}{P_{in}} \tag{6}$$

where P_{out} is the electrical produced power and P_{in} the incident light intensity [6].

2.1.4 Effect of irradiance and temperature

The shape of $I-V$-curves change because of different effects, not only because of varying amplitudes of irradiance, but also because of the cells temperatures (compare to eq.(4)). Higher irradiation will lead to a higher current I_{ph}, also the voltage increases slightly, following that there is more power output, see Fig. 2.6 (a). High temperatures will lead to high currents, but simultaneously the voltage decreases much more, see Fig. 2.6 (b). As a result, the power output decreases with increasing temperature. These effects of course have to be taken into account when designing PV cells. Especially for very hot areas or building integrated PV it is therefore very important to design efficient cooling systems.

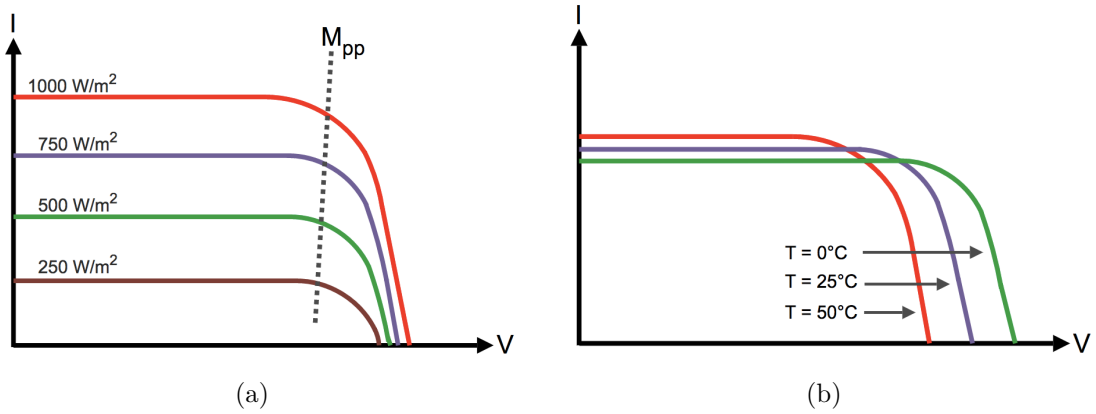

Figure 2.6: In (a) the change of the $I-V$-curve for different irradiances is illustrated, where the current increases at higher amplitudes of irradiation. Fig. (b) shows the effect of temperature, where at lower temperatures the voltage increases much more than the currenct decreases.

2.1.5 Cells, modules, arrays

PV modules are built up from PV cells, furthermore multiple modules are arranged to PV arrays, what is shown in Fig. 2.7. The whole system consisting of all PV arrays, connected in series or parallel, is called the PV generator.

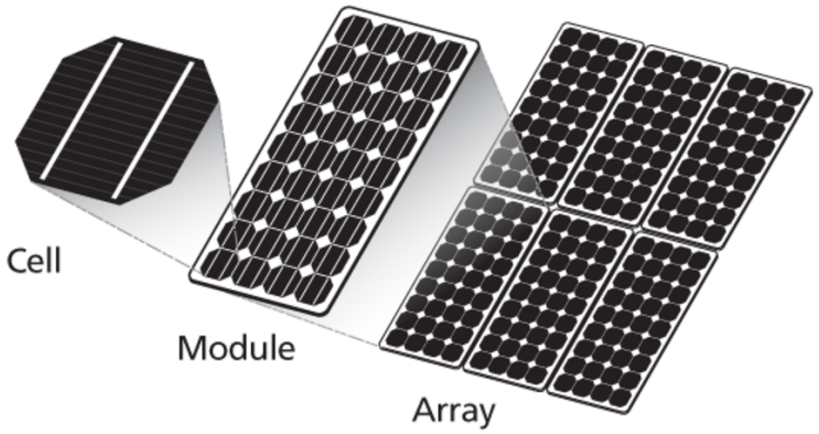

Figure 2.7: The convention of PV-cells, -arrays and -modules [10].

As the PV cells are direct current voltage sources, the voltage is summed up when they are connected in series. Simultaneously the total current intensity does not change. When they are connected in parallel the opposite effect appears, that means the total voltage stays the same, where the currents through every single cell are summing up. Commonly what is done is that around 34 to 144 cells are connected in series to reach a total voltage of around 20-80 V. The modules are then connected

to arrays in series. A problem with series connection is, that when one module is shaded, the string is interrupted and no current can flow. Theoretically, PV modules could be connected in three different ways, as it is shown in Fig. 2.8. In reality, most commonly, the arrays are series-connected.

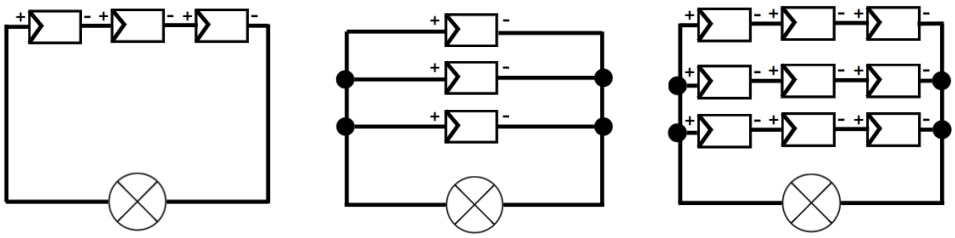

Figure 2.8: The different possibilities of how to connect solar cells: (a) series, (b) parallel, (c) combined series/parallel [11].

2.2 Infrared thermography

In the manufacturing process of PV cells it is not managable not to produce any defects or cracks in the materials structural systems' components. Such defects have to be detected for an optimum and secure performance of the solar cells over their whole lifetime [12]. The capital costs of PV systems are composed of PV modules to 70%, which is why the payback period significantly depends on the implementation of quality assurance through examination and to reduce the sources of malfunction due to surface defects, as cracks and discontinuities. To put it another way, it is very important to review surface defects to guarantee highest possible power outputs and long lifetimes of the modules, which is not feasible with the naked eye.

In order to identify heat differentials on solar cells and determine if specific cells are damaged or defective the method of infrared thermography (IRT) is used. What is required is an IR detecting device, which is sensitive for the radiation of thermal energy in the IR band, what is then transformed into a video signal and finally converted to a surface temperature map. The device in use at the Austrian Institue of Technology is a thermal detector camera. These devices directly absorb the energy in form of photons and warm up the sensor arrays. Each pixel in the array acts like a single element detector with its own thermal response. These temperature-dependet electrical resistances measure voltage drops induced by variations of temperature [12].

In the following section the basic physical principals of IRT analysis and error treatments are discussed. The book by C. Meola, S. Boccardi and G. M. Carlomagno about Infrared Thermography in the evaluation of Aerospace composite and materials ([13]) provides very good explanations, which is very much consulted for the following explanations.

2.2.1 Thermal radiation of objects

As Planck and Boltzmann described it at the beginning of the 20th century, every object at a temperature above $0\,K$ emits a certain amount of energy in specific frequencies depending on its actual temperature. Different objects have different abilities to absorb, reflect and transmit energy, this relationship is mathematically described as the energy conservation rule (7):

$$\alpha + \rho + \tau = 1 \ , \tag{7}$$

where α is the total absorbance, ρ the total reflectance and τ the total transmittance. An object's surface behaves selectively not only with respect to the frequency of the incoming radiaton, but also with respect to the angle of incidence. To be more precise, the absorbed energy comes from particular directions ϕ. In local thermodynamic equilibrium, it follows that the release of energy ϵ from the surface to a specific angle is the same as the absorbed from the same direction. This circumstance was found by Kirchoff and is desribed by Equation (8) (Kirchoffs law).

$$\alpha_\phi = \epsilon_\phi \tag{8}$$

The important conclusion of this law is that the object remains at constant temperature at the rate, whereat it is absorbing the same amount of energy as it is emitting. If this law wasn't valid, the object would cool or warm contrary to the assertion of thermodynamic equilibrium [13].

2.2.2 Objects characteristics

Every object, except a perfect black body, reflects parts of the incoming radiation. This radiation can origin from surroundings such as buildings, PV-modules or for example people who are investigating the cells. Two different effects appear, specular - and diffuse reflection, which are shown in Fig. 2.9. A specular reflector (Fig 2.9 (a)) reflects almost all of the incoming energy I_{inc} to a single direction as I_{out}. This effect appears when a surface is very smooth, where for a perfect mirror $\rho = 1$, following that $I_{inc} = I_{out}$. On the other side, a rough surface reflects the incoming radiation in all possible directions, see Fig. 2.9 (b). The total reflectance ρ depends on the surface structure and the wavelength of the radiation. That is why smaller values of ρ produce more accurate temperature measurements with IRT.

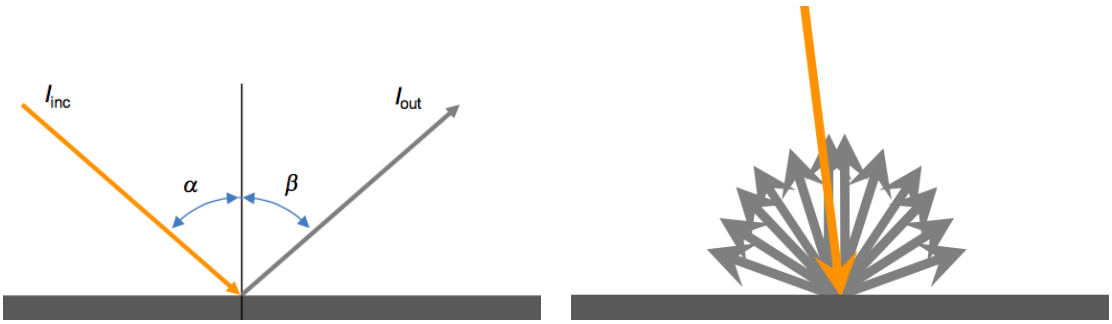

Figure 2.9: Image (a) shows a specular reflector for a smooth surface. Conversely to that, a Lambertian surface produces diffuse reflection raditions to all directions (b) [13].

Considering the explained surface effects, assuming zero-transmittance, the total energy E_d which makes it into the thermographic camera, can be written as

$$E_d = E_\epsilon + E_\rho \tag{9}$$

where E_ϵ is the emitted energy from the surface caused by its specific temperature and E_ρ the reflected part. The conditions are shown in Fig. 2.10.

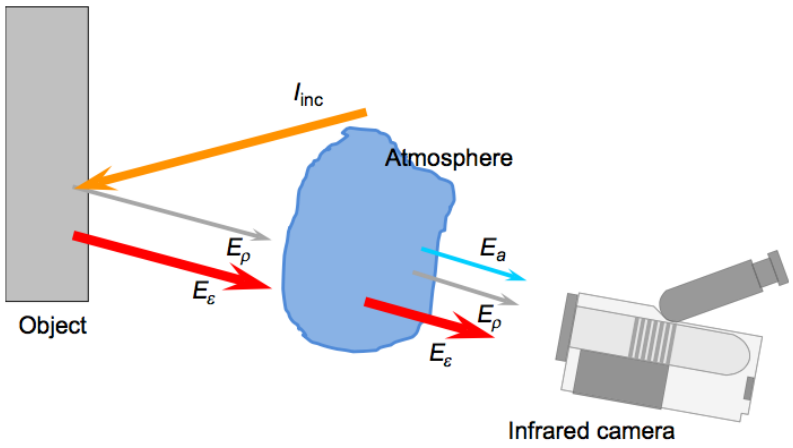

Figure 2.10: Three different energy sources are reaching the IR camera [13].

Of course it is important to know the exact temperature of an object or a PV cell in order to perform accurate IR measurements. Another fact which has to be considered is the angle distribution of emitted radiation, which is not uniformly in all directions in reality.

2.2.3 Errors in IR images

It was already mentioned that the sensor of the used thermographic camera consists of a 2d array, where every pixel is acting like a single element detector (bolometer). If an object with a uniform temperature was held in front of the camera, every pixel should heat to the same temperature. That is not the case, as different nonuniformities appear and corrupt the image. Fortunately there is powerful software which can deal with most of these issues. The most prominent effects are:

- Fixed pattern noise, which appears as gridlike- or stripping patterns laid on top of the image.
- Bad pixels can either lead to dark (dead) pixels or hot pixels, which appear white.
- The effect of vignetting is the darkening of the edges and especially the corners of the image, while there is a lightening effect in the middle. The reason for this is reflection on the lens.
- Different pixels have different offsets and gains, because of irregularities in the production process.

These error sources are controlled pretty well by statistical evaluation of appropriate software on the thermographic camera, however, there are effects which have to be considered by the operator of the camera, while taking the images. Especially reflections play a major role in the quality of images. Fig. 2.11 and Fig. 2.12 represent thermographic pictures taken from a PV roof system.

Sometimes it can be very difficult to differentiate between the radiation of a PV module and unwanted stray radiation. There are many backgrounds with high emissitivities, like the atmosphere, clouds, the sun, walls from buildings or even PV modules, which can lead to failures on images. In Fig. 2.11 on the left bottom side are reflections from a nearby tree. This is identifiable from the white hazes. In the fourth and sixth module the bypass diode is active, therefore only half of the module contributes to the power generation. The white points are the connection sockets. Fig. 2.12 is the second part of the same PV power station, also containing some errorneous modules. On the top of the roof is a chimney. Its reflection is visible on the module beneath it. Such reflections can be detected by taking images from multiple angles.

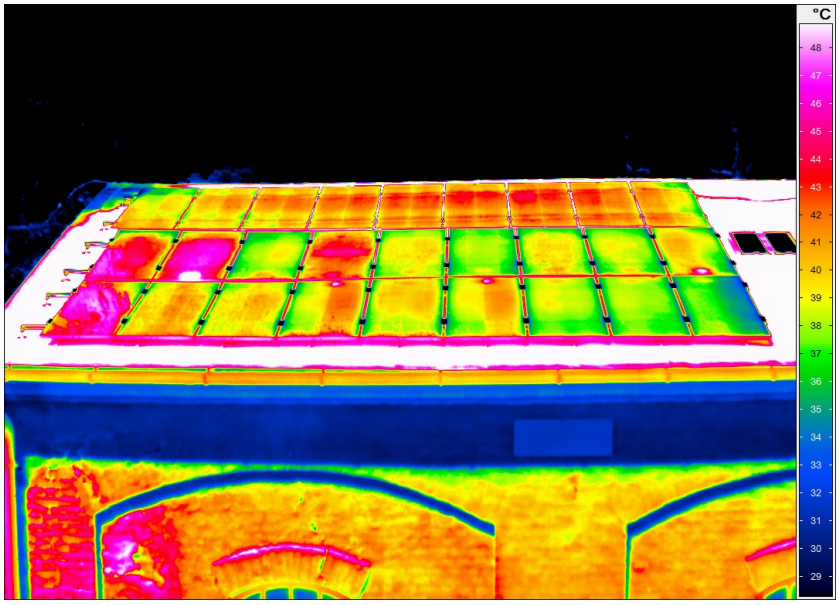

Figure 2.11: Thermograhic representation of a PV roof system containing some major error sources and module failures. Overheated modules like the fourth in the middel row decrease the power output. Furthermore, the fourth and sixth modules of the first rows have active bypass diodes, which leads to only half of the possible power output of a single module [14].

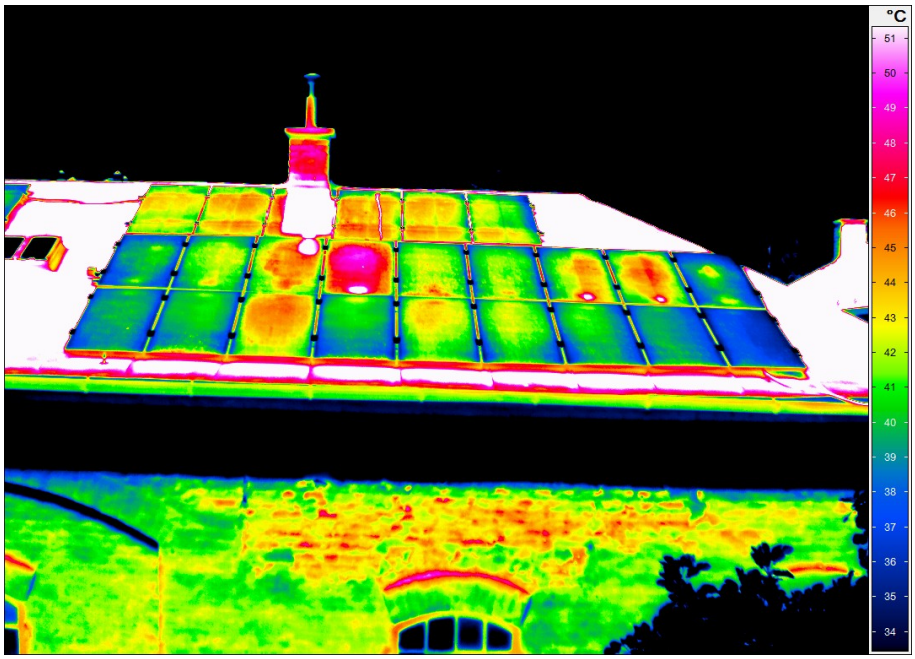

Figure 2.12: Additional part of the PV roof system containing one dysfunctioning module (fourth in middle string) [14].

2.3 Inertial measurement unit

An inertial measurement unit (IMU) or inertial navigation system (INS) is a combination of multiple inertial sensors, typically consisting of three orthogonal rate-gyroscopes and three orthogonal accelerometers. In the scope of this work, the inertial measurement unit also contains two different 3-axis magnetometers, a barometer, a temperature sensor and multiple GNSS-sensors, which are used for positioning tracking and are, therefore, capable of measuring velocity. With all the information gained from the sensors it is possible to measure an approximation of position and orientation in 3-dimensional space and also the temporal progress of the state.

Inertial navigation is used in many different applications including navigation of aircraft, spacecraft, submarines and ships [15]. It is very important to consider the difference between the local and the global system, where the local one is basically the body frame. These values always have to be transformed into the global system to get the true values of movement. The transformation is graphically illustrated in Fig. 2.13.

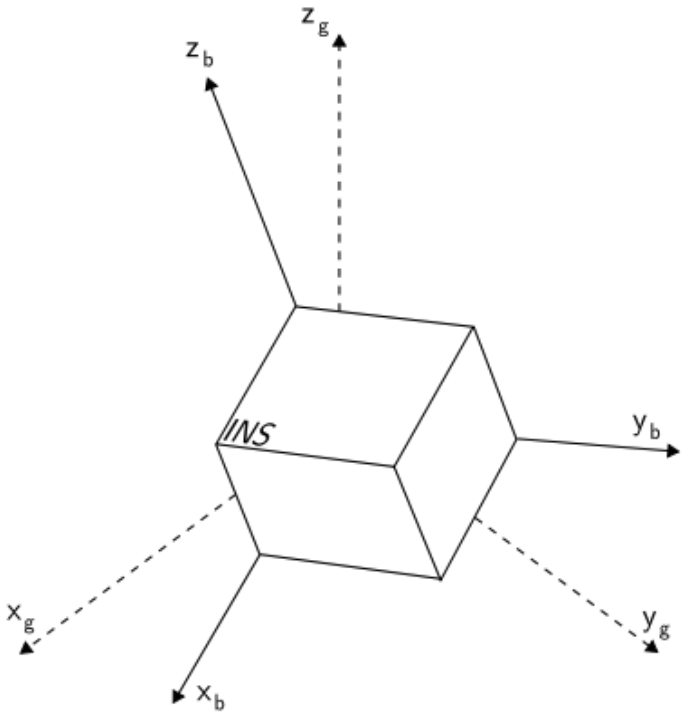

Figure 2.13: Coordinate transformation from body- to global system, which are indicated by the indexes of b and g (dashed axis) [15].

A global system was defined by introducing three unit vectors $\vec{x_g}$, $\vec{y_g}$ and $\vec{z_g}$. The vector $\vec{z_g}$ was defined as the normalized acceleration vector, when the INS was held still. This is why it always points downwards into the direction of gravitation $\vec{g}$.

The unit vector in x-direction $\vec{x_g}$ was defined as the normalized cross product of $\vec{z_g}$ and the magnetic field vector $\vec{m}$, which points to the magnetic north. The third unit vector $\vec{y_g}$ simply was defined as the cross product of $\vec{z_g}$ and $\vec{x_g}$:

$$\vec{z_g} = \frac{1}{|\vec{g}|}\,\vec{g} \tag{10}$$

$$\vec{x_g} = \frac{\vec{z_g} \times \vec{m}}{|\vec{z_g}|\,|\vec{m}|} \tag{11}$$

$$\vec{y_g} = \vec{z_g} \times \vec{x_g} \tag{12}$$

These unit vectors are used to build a matrix, which describes the current system $S_g(\vec{x_g}, \vec{y_g}, \vec{z_g})$ of the INS. The idea behind this is, that by multiplying a random vector in the body frame system with S_g, the vector is transformed to the global system, what is necessary for calculating the movements.

2.3.1 Accelerometer

For the study an ADXL345 three-axis acceleration measurement system is used. It is an MEMS technology based sensor with selectable ranges of $\pm 2g$, $\pm 4\,g$, $\pm 8\,g$ or $\pm 16\,g$. The measurement output is dynamic acceleration coming from shock, but also the static acceleration of gravity. The unit consists of 3 micro differential capacitors, which are built up from independet fixed plates, attached to a moving mass. A shematic illustration for one axis is shown in Fig. 2.14. While acceleration is present, the mass is moving to one direction and the capacity change can be measured. The amplitude is proportional to the acceleration.

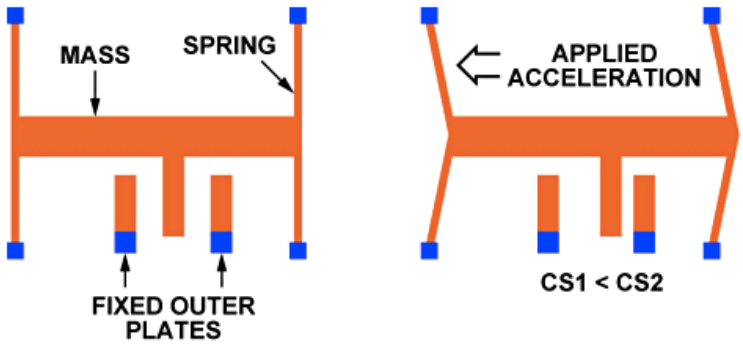

Figure 2.14: On the left image the MEMS accelerometer is shown, when there is no force. On the right image an acceleration is applied and thus the capacities change, which is measured and proportional to the applied acceleration [16].

Constant bias

The constant bias ζ is the offset of the accelerometer signal in m/s^2. It is very important to perform an accurate calibration to eliminate this error, because when

integrating the acceleration, the error in position $s(t)$ will grow quadratically with time t, as

$$s(t) = \zeta \cdot \frac{t^2}{2} \,. \tag{13}$$

The bias can be computed by multiple long term measurement at different orientations of the sensor, taking the average value, when it was held still. This process is very sensitive, because of the gravitational force, which will always appear as bias. Therefore a requirement is to know the exact orientation of the sensor, when measuring the bias [15].

Thermo-mechanical white noise / velocity random walk

The output of MEMS accelerometers is overlayed by thermo-mechanical white noise, which fluctuates at much higher rates than the sampling rate of the sensor. This pertubation is called a white noise sequence, which basically is a sequence of zero-mean uncorrelated random variables. Integrating white noise produces a random walk with a standard deviation that grows proportionally to $\sqrt{t}$ [15].
Therefore, the effect of calculated position is even worse, because after double integration of acceleration, the accelerometer white noise creates a second order random walk in position with mean equals zero and a standard deviation of

$$\sigma_s(t) \approx \sigma \cdot t^{3/2} \cdot \sqrt{\frac{\delta t}{3}} \tag{14}$$

which grows proportionally to $t^{3/2}$. A more precise deriviation of alteration of the standard deviation can be found in [15]. There are even more effects causing errors as flicker noise and temperatue instabilities, but as the main sources are the bias offset, and the white noise, they will not be discussed here.

2.3.2 Magnetometer

The magnetometer which was used in this work is a Honeywell HMC5883L surface-mount, multi-chip sensor designed for low magnetic field measurements and applications like low cost compassing and magnetometry. It is based on the anisotropic magnetoresistive effect (AMR) shown in Fig. 2.15. In principal it describes the dependeny of the resisitivity of ferromagnetic material on the angle between the direction of electric current and the orientation of magnetization. The effect occurs in $3d$ transition metals, because these materials have magnetic anisotropies. On the atomic level, what happens is that the $3d$ band is not fully filled and $4s$ electrons can reach $3d$ subbands, when a magnet field is applied. The anisotropy of the magnetoresistance is explained by the asymmetry of the electron orbits. The consequence of asymmetry are varying cross-sections of electrons, conducting either in parallel or perpendicular to the direction of magnetization [17].

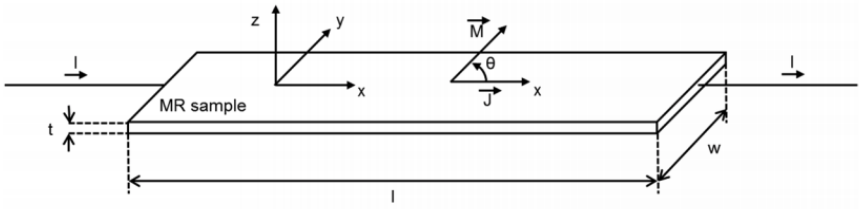

Figure 2.15: Schematic of an AMR element, sensing the magnetic field through a changing resistivity [17].

All ferromagnetic materials have strong internal magnetizations, which are homogeneously directed in very limited volumes, the so-called domains. If regarding ferromagnetic thin films, the thickness is very small against the expansions of the domains. That is why it is possible to consider the change of the magnetoresistance as a two-dimensional problem [17]. Therefore, a resistivity tensor ϱ can be introduced as

$$\varrho = \begin{bmatrix} \varrho_{\parallel} & 0 \\ 0 & \varrho_{\perp} \end{bmatrix} \tag{15}$$

where $\varrho_{\parallel}$ is the parallel component and $\varrho_{\perp}$ the perpendicular component of the resistivity. The only parameter affecting the magnitude of resistance is the angle θ between direction of electrical current $\vec{J}$ and the orientation of the internal magnetization $\vec{M}$. The outer magnetic field is changing the inner magnetization in to the direction of the field from outside. The change of resistivity can be explained as

$$\varrho(\theta) = \varrho_{\perp} + (\varrho_{\parallel} - \varrho_{\perp})\, cos^2\theta = \varrho_{\perp} + \Delta\varrho\, cos^2\theta \tag{16}$$

where $\varrho = \varrho_{\parallel}$ for $\theta = 0°$ and $\varrho_{=}\varrho_{\perp}$ for $\theta = 90°$. The resistivity reaches its maximum level when the direction of the current flow is the same as the direction of the inner magnetization (cos(0)=1) [17].

2.3.3 Gyroscope

A three-axis L3G4200D gyroscope MEMS motion sensor was used in this work to measure the change of angular position in three dimensions. The working principle is based on the Coriolis effect, which is shown in Fig. 2.16. Two springs and dampers are attached to a mass m in two directions x and y. The working principle is illustrated for one direction. In the depicted example, the mass is forced to oscillate in the x-direction at an angular frequency ω_x, by applying an electromagnetic force.

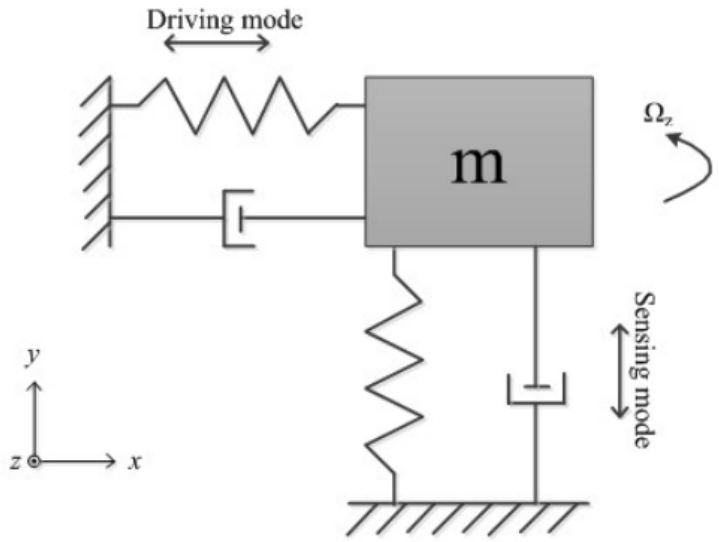

Figure 2.16: The principle of the MEMS gyroscope at a present angular rate in z-direction [18].

That is why the x-axis is called driving mode. The displacement along the x-axis can be stated as

$$x(t) = A_x \, cos(\omega_x t) \tag{17}$$

where A_x is the amplitude. If a rotation is present at angular rate Ω_z around the z-axis, there will be a force around the y-axis, namely the coriolis acceleration

$$a_y = 2\,\Omega_z \cdot dx/dt = -2\,\Omega_z \, A_x \, \omega_x \, sin(\omega_x t) \; . \tag{18}$$

It will lead to a vibrating mass along the y-axis, where the displacement from the equilibrium state will provide the information about the angular rate of Ω_z.

2.3.4 Barometer

A BMP085 digital pressure and temperature sensor was used for the inertial altitude navigation. The inner structure is composed of four piezo-resistors R_{AB}, R_{BC}, R_{CD}, and R_{AD}, which are connected to a wheatstone bridge (see Fig. 2.17) placed on a membrane. Applied pressure leads to a deflection of the membrane and therefore to a resistance change of the piezo resistors. The resistances of R_{AB} and R_{CD} decrease induced by compression, where the other two R_{BC} and R_{AD} increase by stretching. The output voltage or differential voltage V_{BD} of the wheatstone bridge is changed and the pressure difference in reference to the environmental pressure can be calculated.

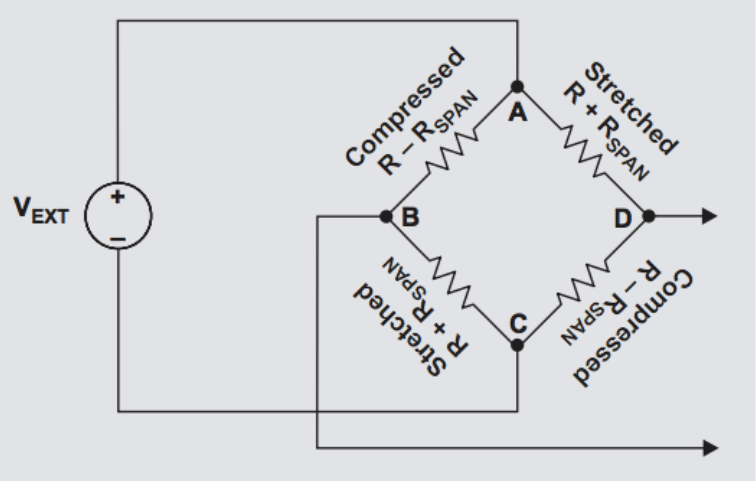

Figure 2.17: Four piezo resistors connected to form a wheatstone bridge [19].

2.4 Global navigation satellite system (GNSS)

GNSS is the shortcut for all operative navigation systems available on earth which provide three-dimensional positioning by analysing transmitted radio signals from orbiting satellites. At the present day many different systems from different countries are available. The most enlarged one is the well known navigation system by the U.S. Government called Global Positioning Systems (GPS). Another well elaborated system is the Russian GLONASS. Also, Europe is currently building up their own system called Galileo, which is already active, but more satellites are needed and will be brought to the orbit for better positioning accuracy. There are even more systems like for example the chinese Beidou and the Indian Regional Navigation System (IRNSS). The satellites have an orbital period of about 12 hours, that means, they approximately circle the earth two times a day. Their altitude is about 20000 km [20]. The following chapter contains the principles of satellite navigation with focus on specific characteristics, which were important for the outcome of this work.

2.4.1 System architecture

Basically, GNSS is built from three different components, the space-segment, the control-segment and a user equipment. An outline is shown in Fig. 2.18. The space segment contains the constellation of the satellites, where the control segment is defined as the stations responsible to interact with them.

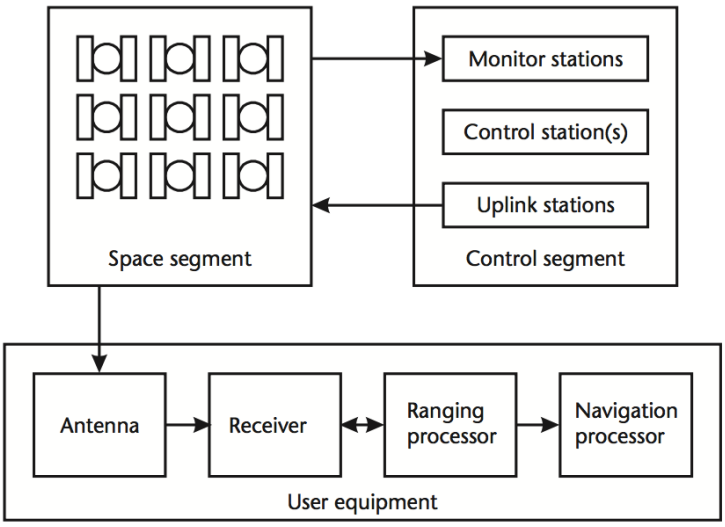

Figure 2.18: The architecture of a global navigation satellite system is split into three segments [21].

The user equipment, or the ground segment, is composed of all the components which are needed to process the signals. That are antennas, receivers and in the case of this work, microcontrollers which process the incoming data and store it on SD-cards.

A more specific description on the used equipment for this work can be found in section 3.

Blocking of signals

It is obvious that if a receiver is behind a building, it is not possible to get accurate positioning data. Usually, for location determination up to 30 different satellites are used, that means it is not necessarily a big problem when one side of the horizon is blocked by a building or terrain, like it is shown in Fig. 2.19. Only the satellites with the strongest signals are used for he positioning evaluation. However, it is important to make sure to think of the suroundings of a measuring site and how it could affect the results, as the best satellites could hide behind an obstacle. Also PV-modules can act as shielding.
Another effect similar in kind is the so called MP effect, which is the result from reflections on any kind of obstacles near the GNSS sensor. Again, PV modules can act as reflector and therefore worsen the evaluation. To counteract to this effect, only satellites with elevation angles higher than 15° are used for the evaluation. More information on how the different effects were handled can be found in section 3.3.

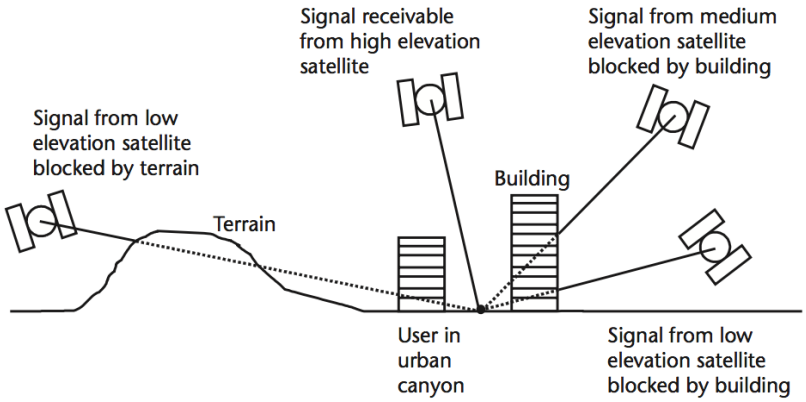

Figure 2.19: Effect of terrain, buildings and elevation angle on the received signals of GNSS [21].

2.4.2 Ionosphere and troposphere propagation errors

As GNSS signals are electromagnetic waves, they are disturbed by electrons, while traversing through the ionsosphere, which extends from about 50 to 1000 km above the Earth's surface [21]. Also, gases in the troposphere (0-12 km) play a role in modifying the signals. From a geometric perspective, as it is represented in Fig. 2.20, it is clear, that signals transmitted by satellites cloese to the horizon will experience much more refraction than signals from high orbiting satellites.

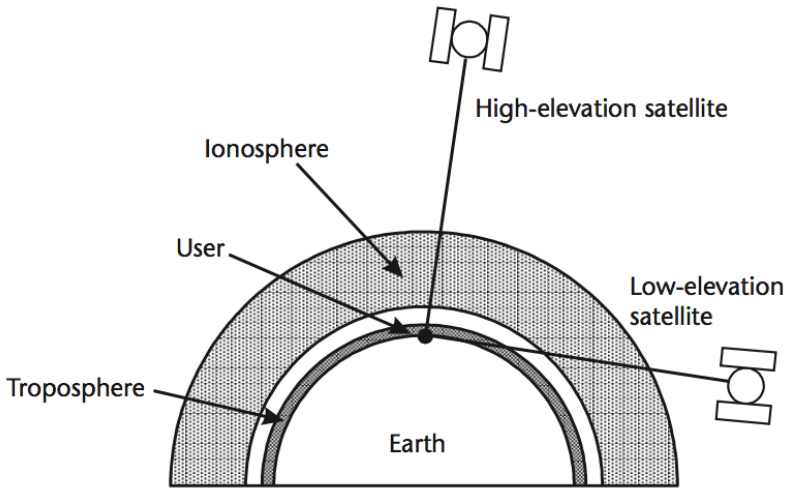

Figure 2.20: Transmitting GNSS signals from different satellites through the layers of Earth's atmosphere [21].

The problem with the ionosphere is, that its behaviour varies daily and depends a lot on the solar activity. Also, the state depends on geographic latitude, longitude and the earths magnetic field. Beside the preceding variations, defined as regular

variations, there are also irregularities which spontaneously intensify and constitute the so-called ionospheric perturbances.

The ionosphere consists of a high concentration of ions and electrons, which are responsible for dispersive effects on GNSS radiation frequencies. Basically, the speed of GNSS signal propagation depends on the frequency ($\sim f^{-1}$) and the concentration of electrons along the way [22]. The total electron content TEC is given by

$$TEC = \int_R^S N_e ds \tag{19}$$

where R is the receiver's position, S the sender's position and N_e the concentration of electrons. The unit of TEC is TECU, where 1 TECU corresponds to 10^{16} electrons/m^2. The state of the ionosphere depends on the sun's activity or the electromagnetic radiation, respectively, which leads to ionisation of atoms and molecules in the ionosphere, and can sometimes even lead to a satellite break down or power blackouts on earth [23]. The long-term behaviour of TEC is shown in Fig. 2.21.

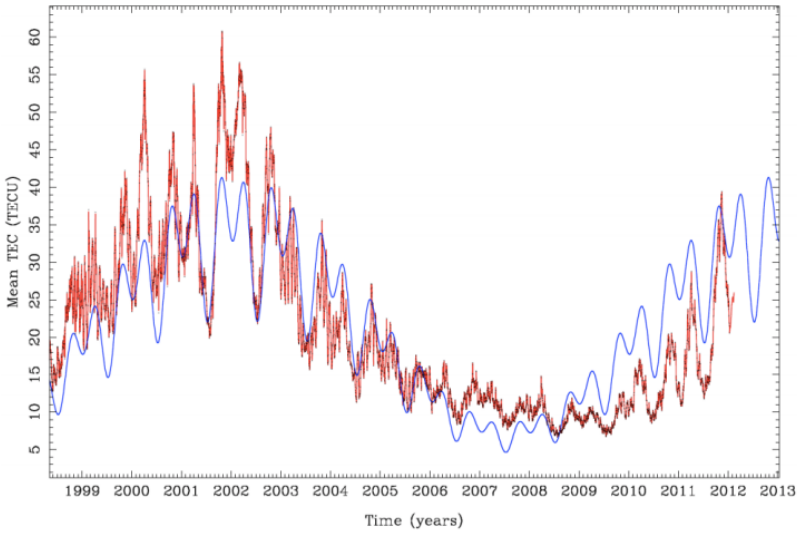

Figure 2.21: The red line indicates the mean global ionization, where the blue is the predicted one [24].

The larger problem for GNSS measurements are short time variances. Ionosphere structure changes, generated by very different radiation patterns of day and night, cause daily TEC variations. The highest values are detected, when the sun reaches its zenith and sends the highest energetic particles. This fact is interesting, as it is synonymous with highest inaccuracies at this time of the day [23].

Another effect appearing in the ionosphere is the so called ionospheric scintillation. These local perturbances cause amplitude fading and phase fluctuation of the

received signals. As in this work the phase of the signals is measured for higher accuracies (see section 2.5), this factor is especially important and interesting [23].

The tropospheric delay originates from constituent gases, which slow down electromagnetic signals, by refracting them. As a consequence, the signals need more time to reach GNSS receivers antennas. Refraction also bends and thereby lengthens the raypath, further increasing the delay. These effects are summarized as the tropsopheric delay [25].

2.4.3 Augmentation system

A satellite based augmentation system (SBAS) consists of multiple satellites, which complement a navigation system, by sending out correction signals and integrity alerts. The integrity alerts protect the user from errenous GNSS signals. If the turbulences are too high, it will be communicated to the user. There are the EGNOS (european geostationary navigation overlay service), WAAS (North-America) and MSAS (Japan). All of these correction systems are used by the receivers in this work when processing the data. The most important fact about SBAS is, that it corrects the time-of-arrival differences of the signals caused by turbulences in the ionsophere [26].

2.4.4 Differential GNSS

Differential positioning is a method which uses corrected signals from reference stations. These reference stations stay still and their positions are very precisely known. From the calculated position the actual inaccuracy of the signal can be found out and correlated with the signal from the moving reveiver, the so-called rover, which in this case would be the thermographic camera. Fig. 2.22 shows the principle of the process.

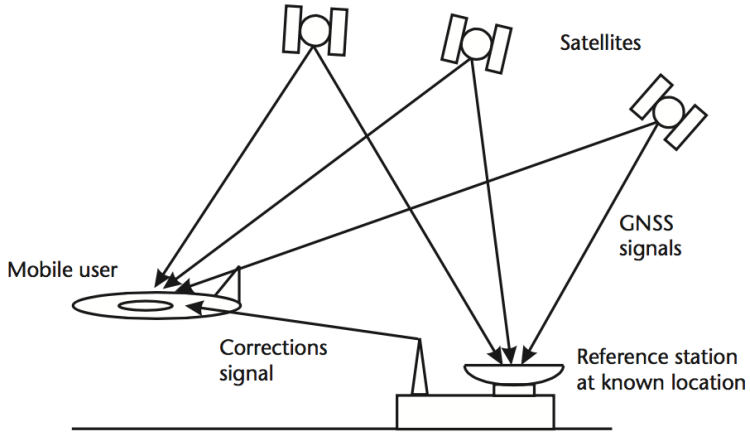

Figure 2.22: The basic structure of DGNSS, where a reference station sends correction signals to a moving receiver [21].

For the scope of this work, the reference station is another GNSS receiver of the same version. By keeping the distance of the two receivers small, it is ensured that they have the same variations in position through atmospheric effects. The difference between DGNSS as it was outlined above, and the method which was used for this work, is the fact, that the position of the reference station is not really fixed, but only fixed for the time, when the thermographic pictures are taken. Therefore, the mean of the fixed reference, or base stations position is used.

A measurement over 72 hours (Fig. 4.1) shows the deviation of the signal using one single GNSS receiver, when it was mounted at a fixed position. It is not possible to directly subtract the deviations of reference receiver from the rovers signal, as the deviations do not really correlate. The reasons for this are not entirely clarified, but potentially it is due multipath effects and different integer ambiguity resolutions (see section 2.5.2). To get this fixed a more sophisticated approach has to be established, which is discussed in the next section.

2.5 Differential carrier phase measurement

This kind of measurement is usually used in surveying to get position accuracy in the order of 2-50 mm. The method differs from the usual GNSS measurements, but has the same initial position as (D)GPS with a base station and a rover. It is important to measure the position of the base at a high precision, at first. This can be done, by measuring for a good amount of time and take the mean value. What is calculated in the end through the process of differential carrier phase measurement, is the distance between base and rover, the so-called baseline. Similar as for usual GNSS, at least four satellites are needed for a position fix (see section 2.5.1). The big difference is how the distance is calculated, for what it is neccessary to know and understand the components of the GPS signal [27]:

- **Carrier phase** is the sine wave of signal L1 and L2, which is produced by the satellite. The carrier of L1 is sent at 1757.42 MHz, L2 at 1227.6 MHz.
- **C/A-code** is the coarse acquisition code, which is modulated onto the L1 carrier phase at 1.023 MHz.
- **P-code** is the precise code, which is modulated onto L1 and L2 at 10.23 MHz.

By using the carrier phase for measurements, much higher accuracies can be reached. This becomes intuitively clear by looking at the illustration of the different components of the GPS signal in Fig. 2.23, as it is a basic physics priniciple, that with smaller structures, higher resolutions can be reached.

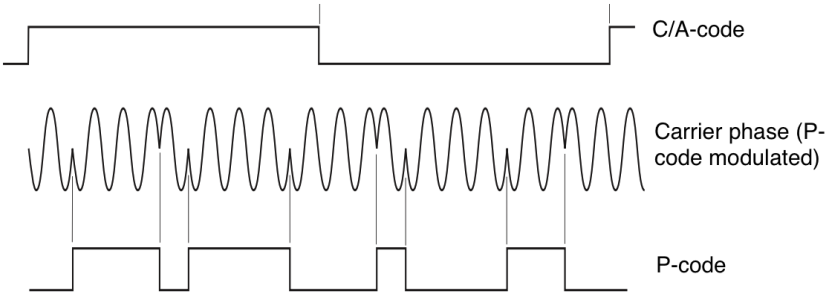

Figure 2.23: The GPS broadcast signal and its different components [27].

2.5.1 Pseudorange

Because GNSS signals travel at the speed of light, already small clock synchronization errors will lead to very big errors in distance measurements. That is why satellites use highly accurate atomic clocks ($10^{-14}\,s$) and synchronize among themselves in the process of pseudoranging. If the satellite clocks run perflectly synchronized, the travel distance from each satellite to receiver are incorrect by the same value $\Delta r_p = const.$

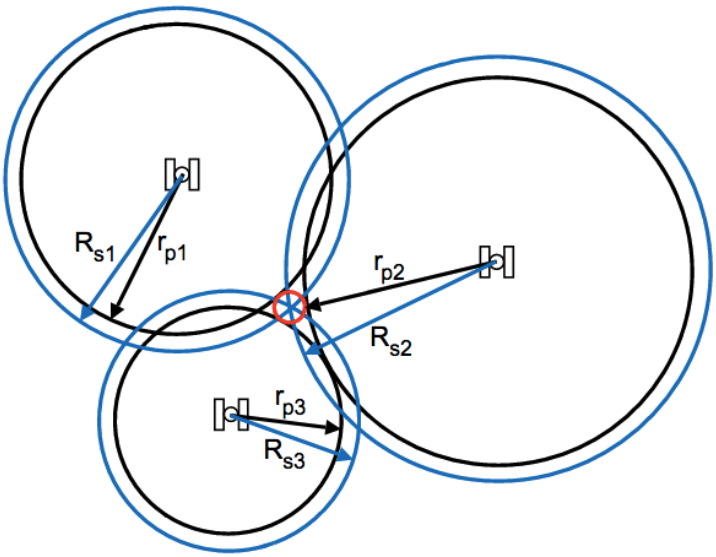

Figure 2.24: Through the method of pseudoranging, the clock synchronization error can be determined and included to the measurements to find the real position of the receiver.

The distance of satellite to reveiver R_s plus Δr_p, introduced by the clock synchronization error, is called the pseudorange r_p:

$$r_p = R_s + \Delta r_p \tag{20}$$

The process of pseudoranging and how to find the real position is graphically illustrated in Fig. 2.24 for a 2-dimensional problem. The processed GNSS signal delivers the initial distance from satellite to receiver (r_p), but not the direction, as it only measures travel time of the signal. When three satellites measure the distance, it will lead to three circles of distance (black). These circles do not intersect at a specific point, but form a triangle, where the middle is the position of the receiver. This is how Δr_p and finally the real position can be found.

Important parameters, characterizing the scatter range of measurement, are the variations of dilution of precision (DOP), which represent the ratio of the position- and range error. If zooming in into the center of Fig. 2.24, there would still be an error at intersection of the blue position measurement circles. The extent of this error is dependent on the constellation of satellites in space, where values smaller than 1 are standing for the best possible constellation and highest possible precision to measure position. This is graphically illustrated in Fig. 2.25 and Fig. 2.26.

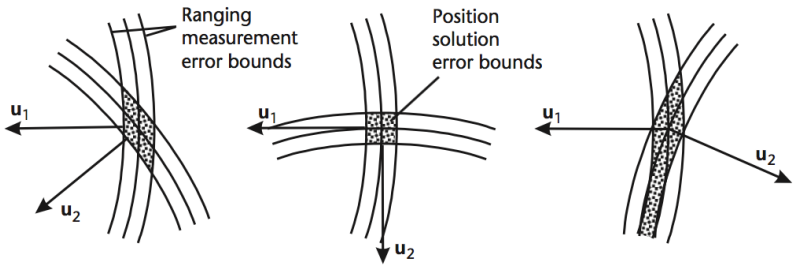

Figure 2.25: Signal geometry plays a major role in the reachable accuracy. For this case represented as a two-dimensional problem [21].

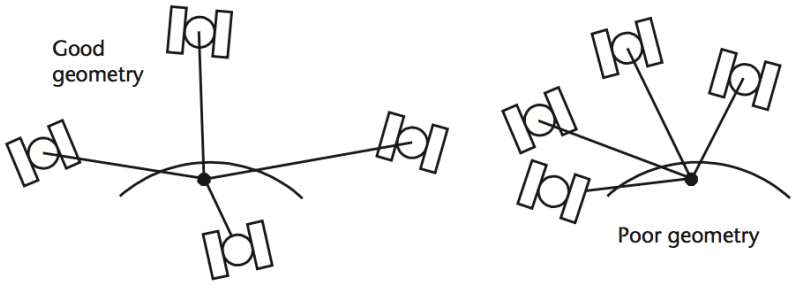

Figure 2.26: The geometry on the left side would lead to a position solution like in the middle example of Fig. 2.25, where the right example is a poor geometry which will lead to high DOP values [21].

It has a multiplicative effect on the range errors. DOP-values of 4 are still considered as good. Values over 10 don't really allow measurements anymore. It is distinguished between different kinds of DOP parameters, which are explained in table 1.

Table 1: Modifications of the DOP parameter.

VDOP	Vertical DOP	Vertical direction	1D
HDOP	Horizontal DOP	Horizontal direction	2D
PDOP	Positional DOP	Position accuracy	3D
GDOP	Geometric DOP	Total accuracy	3D + time

To compute the parameters a matrix E is defined, which consists of the unit vectors from receivers to satellites $i = 1, ..., n$.

$$E = \begin{bmatrix} \frac{x_1 - x}{R_{s1}} & \frac{y_1 - y}{R_{s1}} & \frac{z_1 - z}{R_{s1}} & 1 \\ \vdots & \vdots & \vdots & \vdots \\ \frac{x_n - x}{R_{sn}} & \frac{y_n - y}{R_{sn}} & \frac{z_n - z}{R_{sn}} & 1 \end{bmatrix} \tag{21}$$

The $R_{si} = \sqrt{(x_i - x)^2 + (y_i - y)^2 + (z_i - z)^2}$ vectors are the same as in Fig. 2.24, where the distance from receiver to satellite are already corrected for ionospheric and tropospheric effects. The fourth element describing the time dilution is always one for this case, because it was already corrected by double differencing of the signals in the process of pseudo ranging. A covariance matrix Y is defined, combining the standard deviations in all directions and time.

$$Y = \begin{bmatrix} \sigma_x^2 & \sigma_{xy} & \sigma_{xz} & \sigma_{xt} \\ \sigma_{yx} & \sigma_y^2 & \sigma_{xz} & \sigma_{yt} \\ \sigma_{zx} & \sigma_{zy} & \sigma_z^2 & \sigma_{zt} \\ \sigma_{tx} & \sigma_{ty} & \sigma_{tz} & \sigma_t^2 \end{bmatrix} \tag{22}$$

Finally, the DOP parameters are calculated as:

$$\begin{aligned} \mathbf{HDOP} &= \sqrt{\sigma_x^2 + \sigma_y^2} \\ \mathbf{VDOP} &= \sigma_z \\ \mathbf{TDOP} &= \sigma_t \\ \mathbf{PDOP} &= \sqrt{\sigma_x^2 + \sigma_y^2 + \sigma_z^2} \\ \mathbf{GDOP} &= \sqrt{\sigma_x^2 + \sigma_y^2 + \sigma_z^2 + \sigma_t^2} \end{aligned} \tag{23}$$

2.5.2 Measuring principle

Eventually, if the location of the base station is known in the first approximation after applying the method of pseudoranging, the receivers self-generated phase can be compared with the phase of the satellite's signal and it is tried to find a solution for the number of whole cycles N on the path from satellite to receiver. The method of pseudoranging already delivered some candidates of initial integer ambiguities within a small range, but to find a fix, the carrier phase data from multiple measurments

have to be processed. Changing geometry of the satellites is used to find the solution for the integer ambiguity. In Fig. 2.27 the important parameters are represented. At time $t = 0$ the initial phase ambiguity N_0 is not known, but a fractional phase ϕ_0 is measured. After some time t_1 the satellite travelled, the fractional phase changed to ϕ_1 and there is an accumulation of counted cycles $\sum_{t_0}^{t_1} N$. The initial phase ambiguity stays the same if no cycle slips (see section 2.5.3) occur.

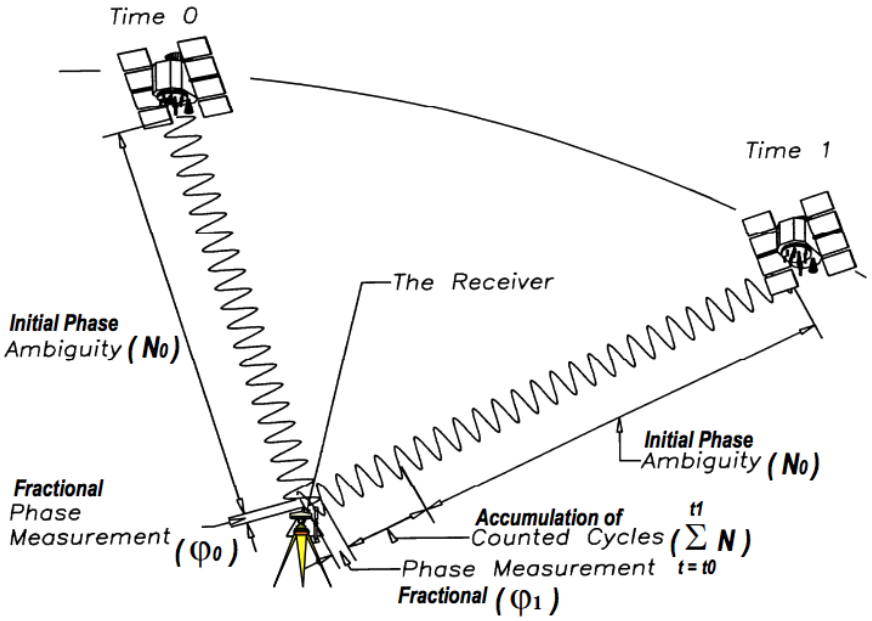

Figure 2.27: The initial phase ambiguity N_0 is not known at the beginning of the measurement. After some time t_1 the phase has changed and a number of N cycles have accumulated what is measured in the receiver [28].

The distance measurement (see eq. (20)) can then also be stated as a function of the phase as

$$R_s = N\lambda + \phi\lambda \ , \tag{24}$$

where N is the total unknown number of full cycles, λ the wavelength of the signal and ϕ the measured phase. It is clear that if N is known, the distance can be calculated very accurately. The best integer value for N_0 is found via the satisfaction of ILS (integer least square) condition. The strategy to solve this problem is known as the LAMBDA method (Least-squares AMBiguity Decorrelation Adjustement), first published by Teunissen [29]. A Z-transformation is used to decorrelate the ambiguities prior to the integer estimation and define an ellipsoidal region containing the integer candidates. The minimization problem is then solved by cyclical searching of this circumscribed region. A very precise mathematical description, for example, can be found in [30].

2.5.3 Cycle slips

A cycle slip is a discontinuity in the carrier-phase measurement due to a temporarily lost lock on the carrier of the GNSS signal. The integer number of cycles is lost in the measured carrier phase, what leads to high uncertainties in the position measurement. These cycle slips are caused by blocking of signals, multipath effects, failures in receiver software, or severe atmospheric conditions. When they appear, it can take a few minutes until a fixed position can be re-established [31]. As it is shown in Fig. 2.28, there is a jump in the instantaneous accumulated phase by an integer number of cycles. The initial phase ambiguity is unknown again.

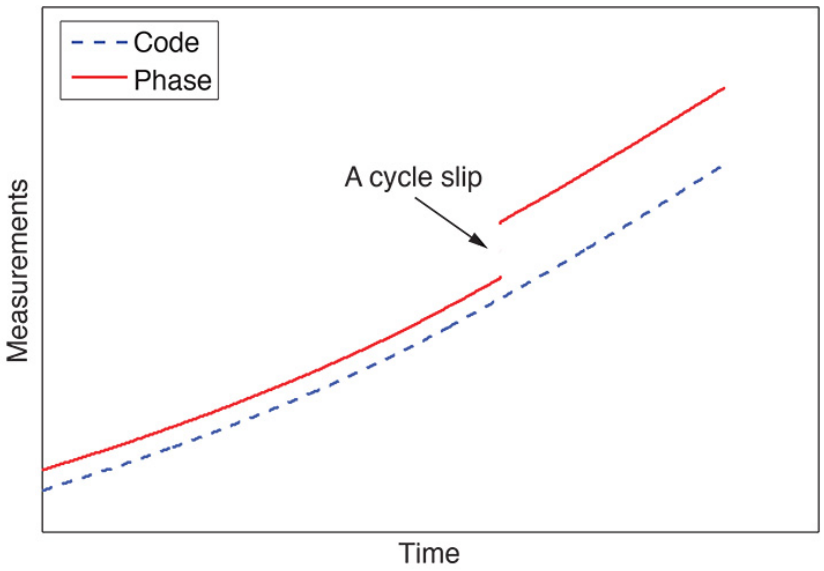

Figure 2.28: Cycle slips are affecting the phase measurements but not the pseudoranges. [31].

To avoid losing the position fix, in the position evaluation process, only satellites with strong signals and almost no cycle slips are used.

2.6 Kalman filter

The Kalman filter, invented by Rudolf. E. Kalman and first published in 1960, is a set of mathematical equations for estimating stochastic variables from noisy observations over time. By applying, the estimated error covariance can be minimized. Kalman first formulated his algorithm [32] for time-discrete systems, one year later he, together with Richard S. Bucy [33], extended the work to time-continous systems.

Following, a intuitively accesible description of the Kalman filter is represented (2.6.1), before a more mathematically detailed approach (2.6.2) is given. The explications for the mathematical description basically follow [32–36].

2.6.1 Combining gaussians

Before discussing the mathematics of the Kalman filter and how to implement it, the powerful consequences of applying it are graphically illustrated and explained for a one-dimensional problem in Fig. 2.29. Represented are three gaussian curves (25) with variance σ^2 and mean μ.

$$N(x, \mu, \sigma) = \frac{1}{\sigma\sqrt{2\pi}} e^{-\frac{(x-\mu)^2}{2\sigma^2}} \tag{25}$$

If there are two probability distributions $N(x, \mu_0, \sigma_0)$ and $N(x, \mu_1, \sigma_1)$, and one likes to know the chance that both of them are true, then they simply have to be multiplied, as it is shown in Equation (26). The result is the overlap of both, which is another gaussian distribution, with a new mean and covariance $N(x, \mu', \sigma')$ [37].

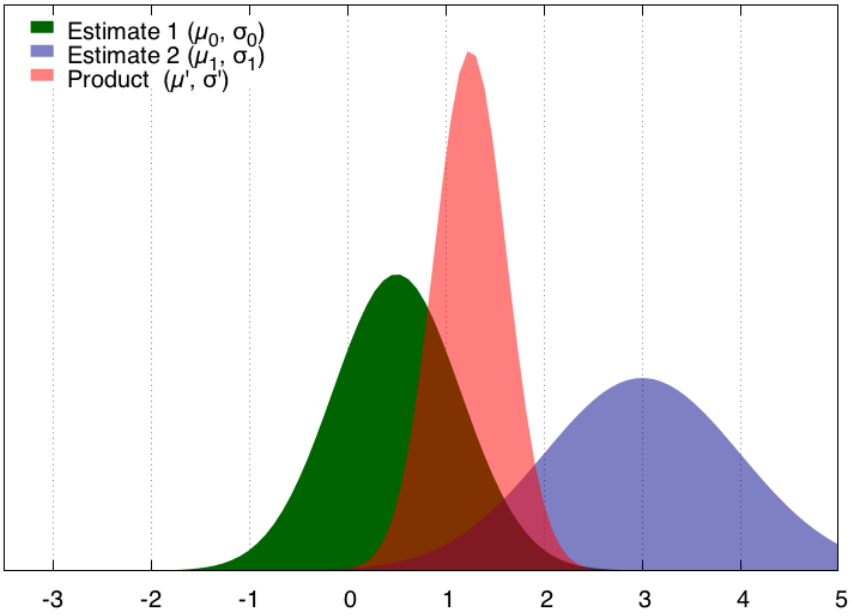

Figure 2.29: The green and blue gaussian curves are combined to get the new red distribution.

$$N(x, \mu_0, \sigma_0) \cdot N(x, \mu_1, \sigma_1) = N(x, \mu', \sigma') \tag{26}$$

Equation (26) will lead to a new mean and a new sigma in the form of

$$\begin{aligned} \mu' &= \mu_0 + \frac{\sigma_0^2(\mu_1 - \mu_0)}{\sigma_0^2 + \sigma_1^2} \quad \text{and} \\ \sigma'^2 &= \sigma_0^2 - \frac{\sigma_0^4}{\sigma_0^2 + \sigma_1^2} \,. \end{aligned} \tag{27}$$

By factoring out a part of these equations and name it k, it becomes clear what the Kalman filter actually does.

$$k = \frac{\sigma_0^2}{\sigma_0^2 + \sigma_1^2} \tag{28}$$

With the newly introduced factor k, equations (27) change to

$$\begin{aligned} \mu' &= \mu_0 + k(\mu_1 - \mu_0) \text{ and} \\ \sigma'^2 &= \sigma_0^2 - k\sigma_0^2 \ , \end{aligned} \tag{29}$$

which means that k is a weighing factor for deciding which of the two gaussian curves is more reliable. This factor is called the Kalman gain. In the illustrated example, the first gaussian distribution could be the position of a moving object after a time step t, where the second distribution could be the position after time t of the same object, communicated through a GPS signal. The Kalman filter combines the information about the same predicted state and weighs it considering the uncertainties.
Usually, there are more dimensions, therefore, it is necessary to use matrices and covariance matrices for the calculations.

2.6.2 Discrete Kalman filter

The first important equation, the so-called linear stochastic difference equation, describes the actual but unknown state x_t of a discrete-time controlled process at time t.

$$x_t = Ax_{t-1} + Bu_t + w_{t-1} \tag{30}$$

The state prediction is a linear function of the prior state x_{t-1} and a random comand or control input $u_t \epsilon \mathbb{R}^l$. What kind of linear function it is, depends on the variables or matrices A and B. In general, they might change with each time step. The $n * n$ matrix A relates the states between two time steps, where the $n * l$ matrix B stands for the relation between the state and the control input. Also, there is a gaussian distributed error fuction w_{t-1}. The other part of the equation is the sensor prediction or the current observation z_t, respectively.

$$z_t = Hx_t + v_t \tag{31}$$

The sensor prediction is a linear funtion of the state prediction plus the current noise measurement error v_t. The m*n matrix H relates the state x to the measurement z_t. The errors w_{t-1} and v_t are assumed to be independent and distributed normally:

$$p(w) \sim N(0, Q) \tag{32}$$

$$p(v) \sim N(0, R) \tag{33}$$

For practical implementation, it is important to keep in mind that the process noise covariance matrix Q and the measurement noise covariance matrix R, are changing after every time step.

2.6.3 The computational origins of the filter

For the following nomenclature, it is important to keep in mind that the actual but unknown state is x_t, whereas every variable with a hat indicates an estimate of the state.
Particularly advantageous is that the Kalman filter can be mathematically divided into two parts: The a-priori state estimate $\hat{x}_t^- \epsilon R^n$ and the a-posteriori state estimate $\hat{x}_t \epsilon \mathbb{R}^n$ at time t. In other words, these two variables are called the prediction state and the correction state at time t given measurement z_t. The a-priori state estimate $\hat{x}_{t-1}^- \epsilon \mathbb{R}^n$ considers all observations $[z_0, ..., z_{t-1}]$, but not the observation l_t at time t. The a-posteriori state estimate $\hat{x}_t \epsilon \mathbb{R}^n$, on the other hand, considers all observations including the one at time t. The a-priori and a-posteriori estimate errors can then be defined as

$$\begin{aligned} e_t^- &\equiv x_t - \hat{x}_t^- \quad \text{and} \\ e_t &\equiv x_t - \hat{x}_t \,. \end{aligned} \tag{34}$$

The apporpriate covariances, namely, the a-priori estimate error covariance and the a-posteriori estimate error covariance are then given as

$$\begin{aligned} P_t^- &= E\left[e_t^- e_t^{-T}\right] \quad \text{and} \\ P_t &= E\left[e_t e_t^T\right] \,. \end{aligned} \tag{35}$$

The described circumstances, the mathematical decomposition into the prediction step and the correction step are graphically illustrated in Fig. 2.30.

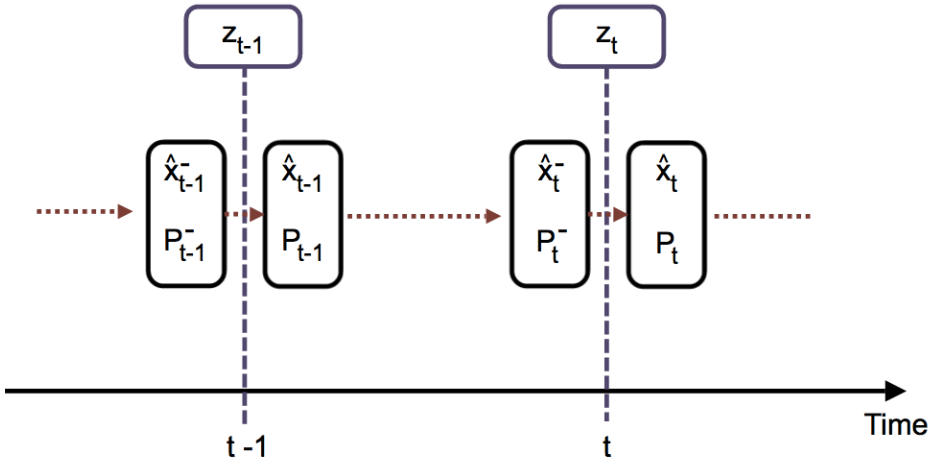

Figure 2.30: The temporal progress of a-priori and a-posteriori state prediction.

In the prediction step an a-priori estimate $\hat{x}_t^-$ is searched for the state status at time t. As for this step, no measurement z_t has been taken, the state is evaluated from the dynamics of the system. The wanted state of the system is evaluated from all estimations, including measured data right up to time $t-1$:

$$\hat{x}_t^- = A\hat{x}_{t-1} \,. \tag{36}$$

The covariance matrix of the a priori estimate P_t^- can be calculated by variance propagation [34].

For this, the covariance matrix of the a posteriori state P_{t-1}^+ is transformed by

$$AP_{t-1}^+A^T \,. \tag{37}$$

Because the process dynamic A is not error free but contains some noise (32), it has to be considered, that for the a-priori covarinace matrix one gets

$$P_t^- = AP_{t-1}^+A^T + Q \,. \tag{38}$$

Equations (33) and (35) represent the prediction phase of the Kalman filter. After this, an update or a correction is performed and the cycle of predict-update-predict-update should run as long as it is conceived.

In the correction step of the Kalman filter, the a-priori state measurement prediction is improved by the observation residue of prediction $z_k - A_t\hat{x}_t^-$ (innovation), what is weighed by a matrix K_t and calculated as

$$K_t = P_t^-H^T(HP_t^-H^T + R)^{-1}) = \frac{P_t^-H^T}{HP_t^-H^T + R_t} \,. \tag{39}$$

The other part of the correction step is to update the prediction error as

$$P_t^+ = P_t^- H_t^T (H_t P_t^- H_t^T + R_t)^{-1} H P_t^- = (I - K_t H_t) P_t^- \ . \tag{40}$$

Finally, the new state is weighed and calculated as

$$\hat{x}_t = \hat{x}_t^- + K(z_t - H\hat{x}_t^-) \ . \tag{41}$$

Figure 2.31 again comprises the cycle of processsing the information in the prediction and correction step.

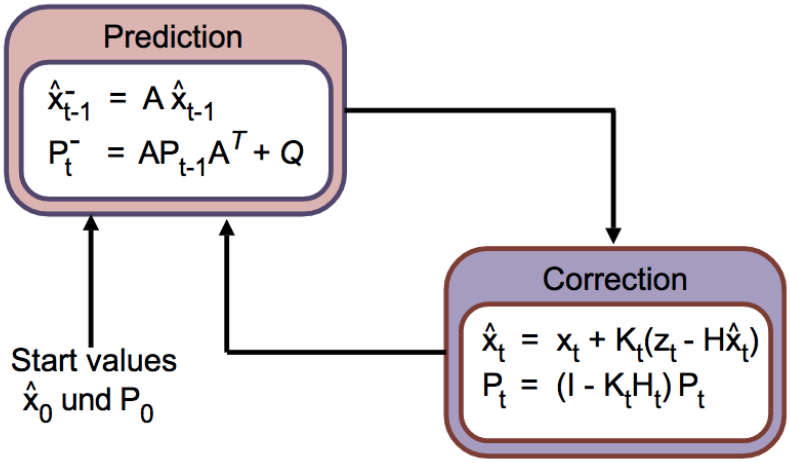

Figure 2.31: The principle steps of Kalman filtering [34].

3 Methodology

The process of building the microcontroller system in the course of this work comprises various different methods. It started with choosing the hardware and designing multiple boards. Following this, the sensors had to be calibrated. The biggest part of the work was to develop proper software, which is able to process the data from the IMU- and GNSS sensors and actually perform inertial navigation. In the end, an execution procedure was defined, pretending how to use the tool in the field of a PV-plant. The different steps and the background knowledge are discussed in the following sections.

3.1 Electronics

All electronics used for this work are low cost components at a total amount of approximately 150 €.

3.1.1 Hardware

The final system consists of two exactly similar boards, a base-station and a rover (see section 2.5), the most important components are represented in Fig. 3.1. The microcontrollers in use are Teensy 3.6 development boards. All programming is done via the USB port in the Arduino integrated development environment (IDE), based on C++. It features a 32 bit 180 MHz ARM Cortex-M4 processor with floating point unit and is therefore very powerful.
The used IMUs are GY-80 multi-sensor boards, therefore the theoretical principles of the different sensors are explained in section 2.3. The benefit of this IMU is that it is capable of measuring in ten degrees of freedom, as it contains a three-axis angular rate sensor (gyroscope), a three-axis digital accelerometer, a three-axis digital magnetometer and a barometric pressure sensor. At a size of only 25.8 mm · 16.8 mm and a I2C digital interface, it is very easily to handle.

(a) (b) (c)

Figure 3.1: The main components used for this work: (a) Teensy 3.6 (b) GY-80 IMU (c) GNSS (respectively GPS) module (Ublox Neo M8N).

The GNSS sensors are of the type *Ublox Neo M8N*. It is possible to receive data simultaneously from GPS, GLONASS, BeiDou and, theoretically, also the European system Galileo. After a firmware downgrade, which had to be done to measure the raw messages coming from the satellites, it was not possible to receive Galileo data anymore.

3.1.2 GNSS communication

The data transfer between GNSS sensor and the Teensy microcontroller is accomplished over a serial protocoll. That means the data is streamed as one bit at a time. One must consider that the serial protocol is highly configurable and that it is critical to ensure both devices on a serial bus are configured to use the exact same protocols. An important parameter is the baud rate, which defines how fast the data is transfered over a serial line. Its unit is bit per second [bps]. Both devices have to operate at the same rate to make sure the data is transfered correctly. It is possible to calculate the time needed for transmitting one single bit by inverting the baud rate. For example for 9600 bps, which is a common rate, it is 104 μs per bit. This is important, because the GNSS sensor in use receives much more bits per second. Therefore, the baud rate has to be higher, or data gets lost. On the other side, one shall not overstate the baud rate, because if it is too fast for the microcontroller, again, errors can appear [38].

Data transmission frame

Every block of transmitted data is sent as a packet or frame of bits. These frames are created through attaching a synchronisation- and a parity bit to the data. The size of the data part is not declared at first place, but certainly most common are 8-bit-byte. Again, both serial devices need to have the same size of data frames. Also, the order has to be clarified, that means, if the most-significant bit (msb) is first and then descending the others, or the other way around. Start- and stop bits, also called synchronization bits, close up a data frame. An exemplary serial frame is illustrated in Fig. 3.2.

Figure 3.2: The serial frame, where the segments have defined sizes [38].

The parity bit is there for fault checking, but not in use very often anymore, because it slows down the data transmission, and there are other, better ways to check error appearances.

The communciation between the IMU and the Teensy is accomplished over a I^2C

(Inter-integrated Circuit) serial protocol, which allows multiple integrated chips to communicate simultaneously. The main advantage over a conventional serial communication is that there is no theoretical limit in baud rate [39].

3.2 Inertial navigation

As the IMU contains multiple sensors, a lot of information is gained and it is possible to navigate in various ways. The different experimental methods are explained and discussed in the following section.

3.2.1 Calculating position by integrating acceleration

The first approach was to measure the orientation via the gyroscope and calcuate the covered way by integrating the acceleration signal twice. The process is graphically illustrated in Fig. 3.3. The idea was to compare the obtained position with the measured GNSS position in a Kalman filter. First, the acceleration signals have to be projected onto the global axes. The next important step is to correct the acceleration caused by gravity. At a value of $9.801\,m/s^2$ this is a crucial point. Furthermore, the error in position, shown in eq.(13), grows quadratically with time, which worsens the outcome of the measurement. The results are represented in section 4.3.

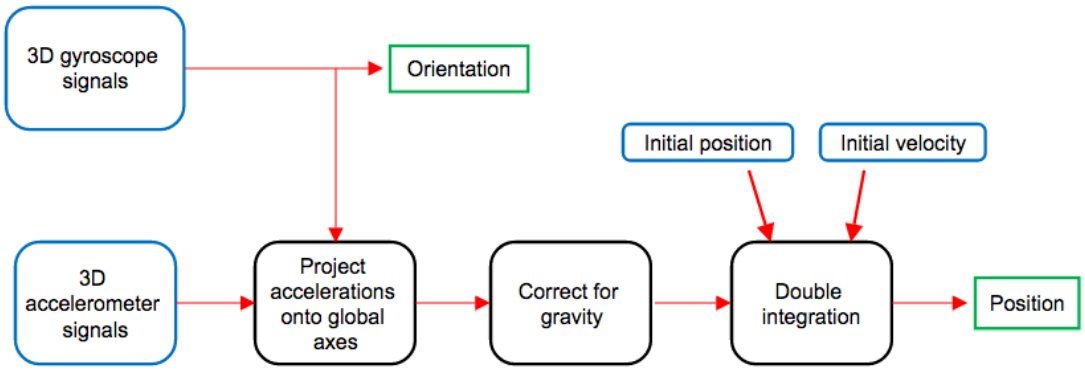

Figure 3.3: The change of orientation is measured through the angular rates of the gyroscope. After projecting the acceleration into the global system, gravitational acceleration has to be subtracted. The signal is then integrated twice and the position can be calculated.

3.2.2 Measuring altitude

The MEMS barometer output is air pressure in units of Pascal. By using the barometric formula (42) it is possible to calculate the pressure as a function of altitude. The constant C is a temperature gradient, which is assumed at a value of

$C = 0.65\,K/100\,m$, this is the mean value for all different kinds of weather conditions.

$$p(h_1) = p_0 \cdot \left(1 - \frac{C\Delta h}{T(h_0)}\right)^{\alpha} \tag{42}$$

Furthermore, Δh is the difference in altitude and $T(h_0)$ the temperature at a specific altitude h_0. The exponent is calculated as $\alpha = MgR^{-1}C^{-1}$, where M= $0.02869\,kg\,mol^{-1}$ is the mean molar mass of the atmosphere, g the gravitational acceleration and R= $8.314JK^{-1}\,mol^{-1}$ the universal gas constant . After some remodelling of equation (42), assuming international atmospheric standards ($T = 15°C = 288,15K$, $C = 0.65K\,(100m)^{-1}$), the altitude (43) can be stated as a function of pressure as

$$h(p) = \frac{288.15\,K}{0.0065\,\frac{K}{m}} \cdot \left[1 - \left(\frac{p(h)}{p_0}\right)^{\frac{1}{5.255}}\right] . \tag{43}$$

At this point another problem appeared, namely, the correlation of altitude measurement from GNSS and barometric sensor, because of the variability of the atmosphere's parameters. To figure out the constant of p_0, to correlate the two different measurement methods, altitudes are plotted against each other (Fig.3.4) and two outer points $h(p_1)$ and $h(p_2)$, including the corresponding pressures, are noted. By dividing them p_0 is found as

$$\frac{h(p_1)}{h(p_2)} = \frac{1 - \left(\frac{p_1}{p_0}\right)^{\alpha}}{1 - \left(\frac{p_2}{p_0}\right)^{\alpha}} \Longrightarrow p_0 = \sqrt[\alpha]{\frac{p_1^{\alpha} - \frac{h_1}{h_2}p_2^{\alpha}}{1 - \frac{h_1}{h_2}}} . \tag{44}$$

To get most accurate results, this process has to be performed before every measurement to include the current atmsopheric pressure condition.

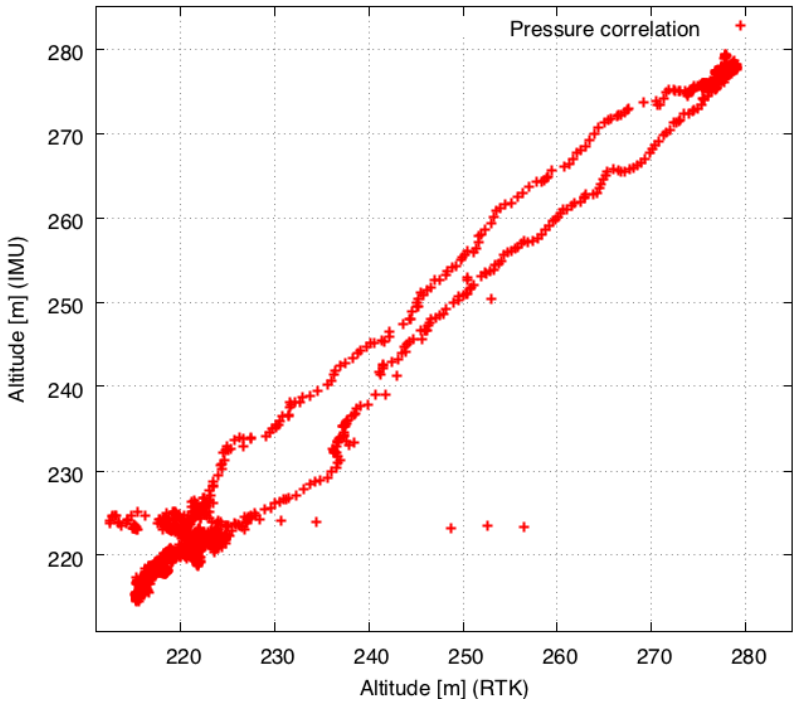

Figure 3.4: The low-hysteresis correlation of altitude measurement through RTK and IMU.

The hysteresis curve is supposed to arise from a slow response time of the RTK altitude measurement. As it is visible in the plot of 3.4, the slope of the curve approximately is linear with slightly lower altitude values for the RTK system. The source of error probably are fast, sudden altitude changes, as it was the case when the car was driven up and down the hill. The RTK system looses its position lock and have to perform multiple calculations to find a lock again. The error in these caluclations can then lead to over- or underestimated altitude measurements, which explain the jumps at the altitude changes and linear progressions after that.

3.2.3 Processing carrier phase measurements with RTKLIB

To get high resolution tracks and evaluate the phase measurements, the raw logged data has to be converted to so-called RINEX (Receiver Independet Exchange Format) files, which is a standard GPS/GNSS data format supported by many receivers and post-processing analysis software. The very powerful software used for processing the GNSS measurements in this thesis was the open source program package RTKLIB by Tomoji Takasu [40]. The application RTKCONV is used to transform the log files to RINEX .obs (observation data), .nav (navigation data) and .sbs (correction data) files. These files are then used for post processing. Each of them contains a header section and a data section, where global information for the entire files are presented in the header. In the observation file, the observations are devided in measuring epochs. Such an epoch is represented in Fig. 3.5 as a segment of

an observation file. Each epoch contains a line for every satellite, starting with the identification of the satellite. For the depicted example, twelve satellites were visible at a time, the ones starting with a ”G” are GPS satellites, whereas the ones starting with ”R” are GLONASS satellites. The second column represents the pseudorange in meters, the third the carrier phase in whole cycles (which usually is tracked off at zero when the rover is turned on), the fourth is the doppler shift of moving satellites and the fifth the signal to noise ratio (SNR).

```
425 G 5  24172534.617     -60362.99421      2403.447         40.750
426 G31  21497841.691     -13826.56621       545.625         47.250
427 G21  23756841.323     -57788.03423      3656.846         29.000
428 S20  24635940.505      -4528.18722       543.506         37.500
429 R15  19789838.687     -32516.680 1      2091.260         38.250
430 R24  19640267.513      29493.788 2     -1108.945         28.500
431 G29  20154868.466     -15275.11821       441.875         46.250
432 G 2  23507287.696      66688.36521     -2047.998         32.250
433 G25  21049218.877      41911.23821     -1295.908         48.250
434 G12  24064242.631      71286.18421     -2843.691         38.500
435 R23  22804414.669      71000.85122     -3427.949         31.250
436 R17  20296037.971     -20597.39921      2807.227         37.000
```

Figure 3.5: Example sequence of some measured data by different satellites in the observation file. From left to right the terms describe: Satellite identification, pseudorange, carrier phase, doppler shift and SNR in dBHz.

As this is an example epoch from the beginning of a measurement, cycle slips appeared, these are visible as the splitted carrier phase values (6th and 7th lines). The application RTKPOST included in RTKLIB is used for postprocessing. Several options have to be selected. The positioning mode was set to static-start, in which case the assumption of a fixed position at first helps to find a positioning fix quicker. The integrated Kalman filter was set to forward, as it is fast and the safest solution. The other options would be backwards or combined, where combined delivers good results, but only if the signal is very stable and no cycle slips appear. The elevation mask is set to 15° to make sure only satellites are used for the positioning solution, which have an elevation angle of more than 15°. In *options/Setting2* one has to decide between "fix and hold" and continuous mode of the integer ambiguity resolution. The risk of the "fix and hold" option is that the solution will be locked to a false position fix and the standard deviations of the positions are fairly underrated. However, the results are better in "fix and hold" mode.

3.3 Final implementation - Base-station and rover

For the final design of the system, involving the fixed base-station and the moving rover, many outside influences have to be considered. As the base-station is placed at a fixed position its design certainly is different than the one of the rover, which is attached to the thermographic camera and moved around. The following list contains the significant influences which were taken into consideration:

- **Gusting wind:** Wind is an important factor as it is not only capable of producing cycle slips in carrier-phase measurements through physically moving

the sensor, but also affects the pressure measurement. It was observed that a wind gust can lead to a pressure increase of about 0.25 hPa, which corresponds to an altitude change of ∼2 m.

- **Atmospheric pressure variability:** There is a daily atmospheric pressure progression, which can lead to huge altitude miscalculations. Already after some hours pressure changes in the range of an equivalent to several meters are possible (see. Fig. 3.11). As the base station is fixed at a specific altitude, its pressure behaviour can be used as an offset for the rovers altitude measurement and simply subtracted.
- **Temperature change:** Temperature is directly correlated to pressure through the ideal gas law $pVT^{-1} = const.$ and could, therefore, influence atmospheric pressure, if the system where the IMU is located would be closed. Thus, it is neccesary to ensure interaction of the system and its environment.
- **Multipath effects:** Reflexions of GNSS signals from the ground or other obstacles lead to MP effects. Especially mentionable are reflexions from the ground. Copper plates are used as shieldings and work as mirrors for GNSS signals in the range of GHz.
- **Humidity shift:** Water is capable of leading to a short circuit and destroying the electronics. Therefore, the IMUs have to be protected from increasing humidity during the night and possible condensation of water on the sensors.

The final rover design is represented in Fig. 3.6. It has an extension on one side to enable the fixation on the camera.

Figure 3.6: The rover from behind. In future measurements the single-lens reflex camera will be exchanged with a thermographic camera.

3.4 IMU-calibration

A ball of foam material (Fig. 3.7) was used to perform the calibration of the sensors. The ball was cut in the middle and some foam was taken out, so the board and the accumulator could be placed inside of it. In course of this method every angle was easily accesible.

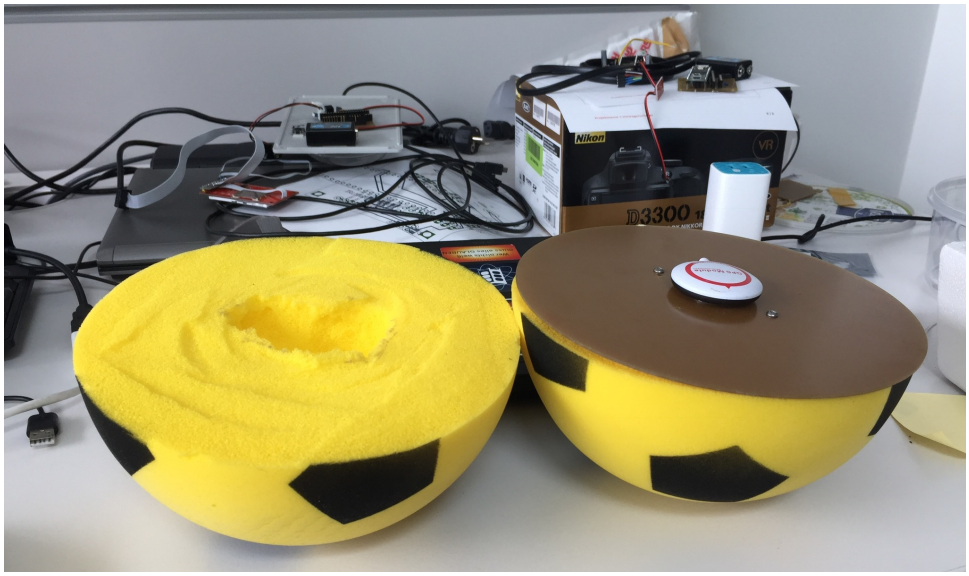

Figure 3.7: A foam ball served as a calibration tool to easily access all solid angles.

Accelerometer and magnetometer

The software used for calibrating accelerator and magnetometer can be stated as straightforward. Basically, the radius of the sphere produced by values in x-,y- and z-direction was calculated in multiple software loops for different offsets and scaling factors in all directions. The goal was to find the best, simultaneously the smallest standard deviations and the best fiting scaling factors. To make things clear the process is graphically illustrated in Fig. 3.8, where the three-dimensional problem was broken down to a two-dimensional one. Shown are real measured acceleration values. In plot (a) some points are at the edge of the delineated circles, that means there was roughly no acceleration in z-direction at that time. The sensor was orientated at an angle of 90° against z-direction, which is upwards in the system of the IMU. For the points inside of the circles, there was some amount of acceleration into z-direction. While conducting this method, it was important not to produce any significant physical accelerations by moving the ball, which would have worsened the calibration and produced deviations from gravitational acceleration. As it is shown in Fig. 3.8, the green circle has a higher standard deviation than the blue one. The software loops ran as long as standard deviations of $0.008\,m/s^2$ and $0.017\,gauss$ were found, what lead to an error in acceleration and magnetization measurements of $0.01\,\%$.

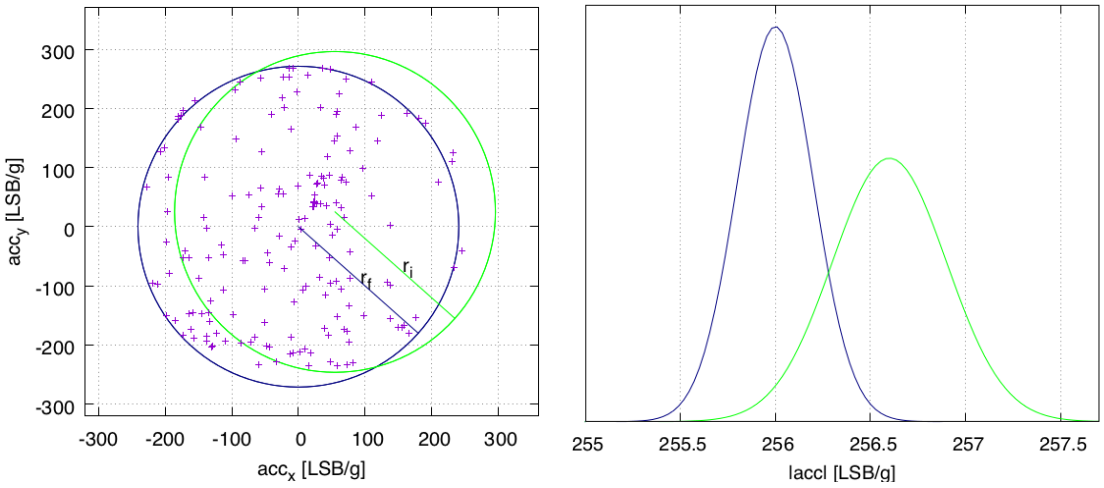

(a) (b)

Figure 3.8: The graphical illustration of the brute force calibration method, where the best fiting values for offsets and scaling factors were found through calculating the standard deviations in multiple loops.

Fig. 3.9 shows the calibrated acceleration values. The same was done with the magnetometer, where the scale of the sphere is not the gravitational acceleration, but the value of the earth magnetic field.

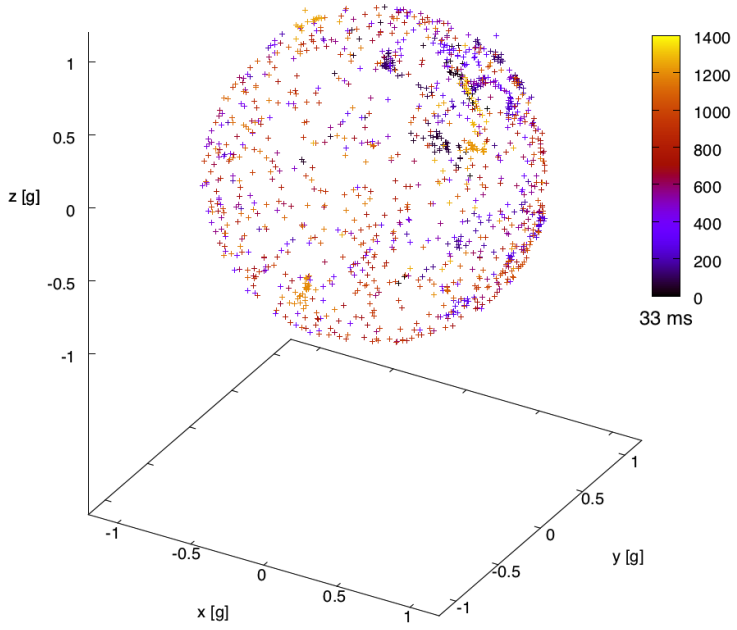

Figure 3.9: The calibrated acceleration values in three dimensions.

In the plot the colors indicate the time of the measurement. The measurement

frequency was 1 Hz. As it is shown, all solid angles in three-dimensional space could be reached.

Gyroscope

The most important aspect of calibrating the gyroscope was to figure out the angular drift when helding it still. To find it out, the gyroscope was shaked for some seconds and then placed on the table, where it was lying still. It immediately went into an equilibrium state and had some constant drifts in all directions.

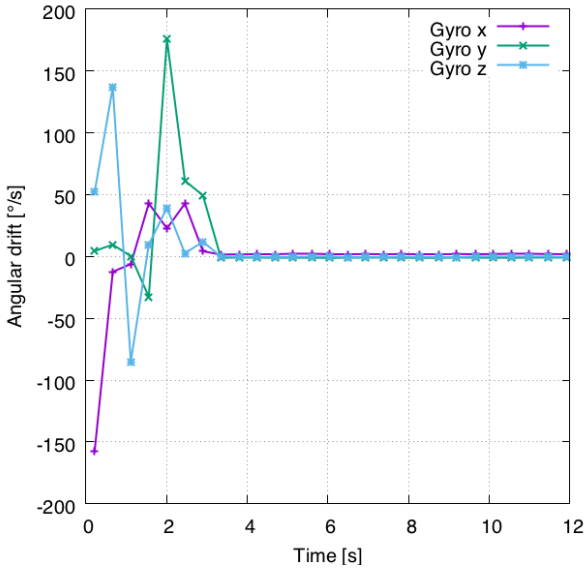

Figure 3.10: The angular drift of the gyroscpe in x-, y- and z-direction in units of $[^{\circ}s^{-1}]$.

It was found that the drifts in the different directions are constant and do not depend on the orientation the IMU is placed on the table. Angular drifts of $\omega_{dx} = 1.5\,^{\circ}s^{-1}$, $\omega_{dy} = -0.9\,^{\circ}s^{-1}$ and $\omega_{dz} = -1\,^{\circ}s^{-1}$ were found. These drifts have to be subtracted from the angular velocity measurements.

Pressure

The output from the barometric sensor is pressure in Pascal (Pa). The calibration process already came up in section 3.2.2. Because pressure is varying daily and even then it is not constant, the base station is used as a reference to subtract the hourly pressure changes, which is shown in Fig. 3.11. Given the fact that the yellow points in the graph are in the same altitude range than the RTK measurement in blue, the method of simple subtraction workes fine. As it is shown, the yellow curve has a slightly different progression than the green line, because there are some variations between the two different IMU pressure sensors of the base station

and the rover. By calculating p_0 from equation (43), it is possible to correlate the pressure measurement from the IMU with the one by the RTK. As for the task of this work, only relative pressures are interesting, there were no further steps perfomed to calibrate the sensor.

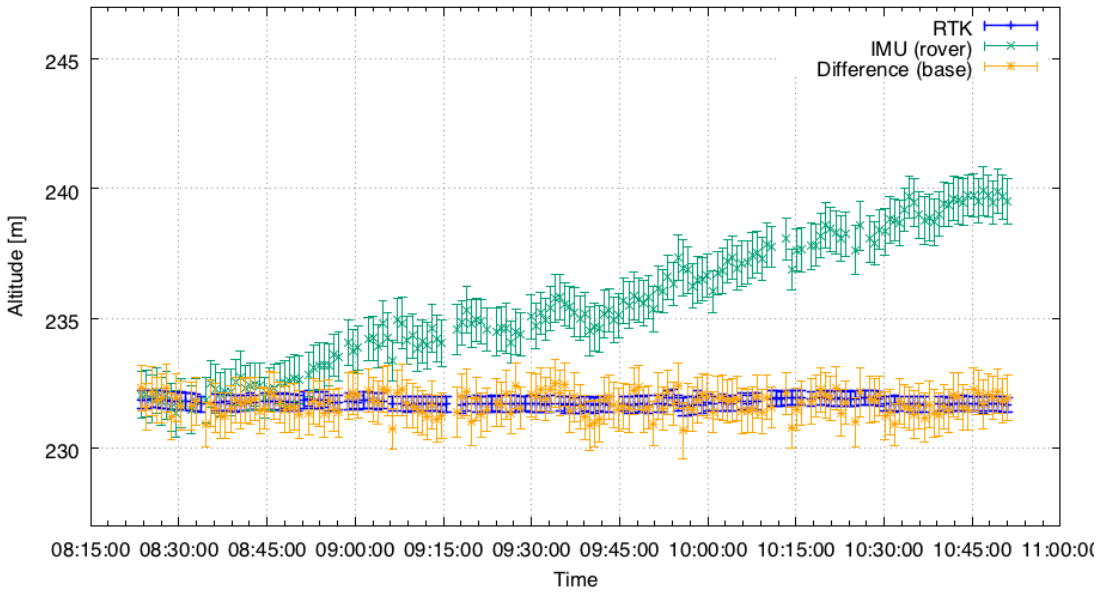

Figure 3.11: Output from the pressure sensor of the rover (green points), the RTK altitude measurement (blue points) and the subtracted base station pressure values from the actual rover measurement (yellow points), when helding the sensors fixed side by side. A low pressure area came up which lead to a pretended altidude increase of several meters in only a few hours. This could be corrected by using the data from the base station.

3.5 Combining images

The last but vital step of this work was to backproject pictures to a defined plane to later take pictures of different modules and combine them to a representation of the entire PV plant, so it is much easier to evaluate the pictures. Two different techniques were tested and compared. One of the possible approaches is the localization of keypoints in different pictures, which can then be used to combine the pictures through affine transformations in a linear least square solution. The method is called Scale-invariant feature transform (SIFT) wheras already multiple open source software packages do exist. The approach implemented in this work is a geometric one, where the variable positions and orientations of the camera are identified by the different sensors, so the pictures can then be transformed and backprojected to a defined plane. Lens distortions are corrected with help of a polynomial function 3.5.3.

3.5.1 Scale-invariant feature transform (SIFT)

The method of SIFT is used to identify keypoints in the pictures. It was first published by D.G. Lowe [41]. Specific features which can be found in multiple images are extracted, so the images can be combined. At first, candidates for key points of images are found with a cascade-filter approach. The second step is to determine positions and scales, which can be found in different views at a high probability. In other words, one wants to find positions which are invariant in terms of scale change of an image. To achieve this, a scale continuing function, the scale space is used. Because Gauss functions and also Laplacian of Gaussian functions have an isotropic kernel, what means that they are independet on direction (rotation invariance), they are used to define the scale space $L(x, y, \sigma)$ of a picture. It is written as a convolution of an Image $I(x, y)$ with a scale variable Gauss function in the form of

$$L(x, y, \sigma) = G(x, y, \sigma) * I(x, y) \ . \tag{45}$$

To find stable features, scale space extrema are evaluated by means of the Difference-of-Gaussian (DoG) function, which is defined as

$$\begin{aligned} D(x, y, \sigma) &= (G(x, y, q\sigma) - G(x, y, \sigma)) * I(x, y) && (46) \\ &= L(x, y, q\sigma) - L(x, y, \sigma) && (47) \end{aligned}$$

where q is a constant factor. It is looked for intensity changes at two nearby scales. The biggest advantage in choosing this function is that it is very efficient in computing, because the smoothed images L have to be computed in any case for space feature description and D can therefore be computed by simple image substraction [41].

How to approach $D(x, y, \sigma)$ is shown in Fig. 3.12, where on the left side it is represented that the initial image is convolved with Gaussians, which are seperated by the constant scale space factor q. Every octave is seperated into an integer number s of intervals, so that $q = 2^{1/s}$. For every octave $s+3$ images have to be produced in the stack of blurred images, therewith in the end extrema detection covers complete octaves. Image scales, which are beside each other, are subtracted (46) to produce the DoG images shown on the right in Fig. 3.12 [41].

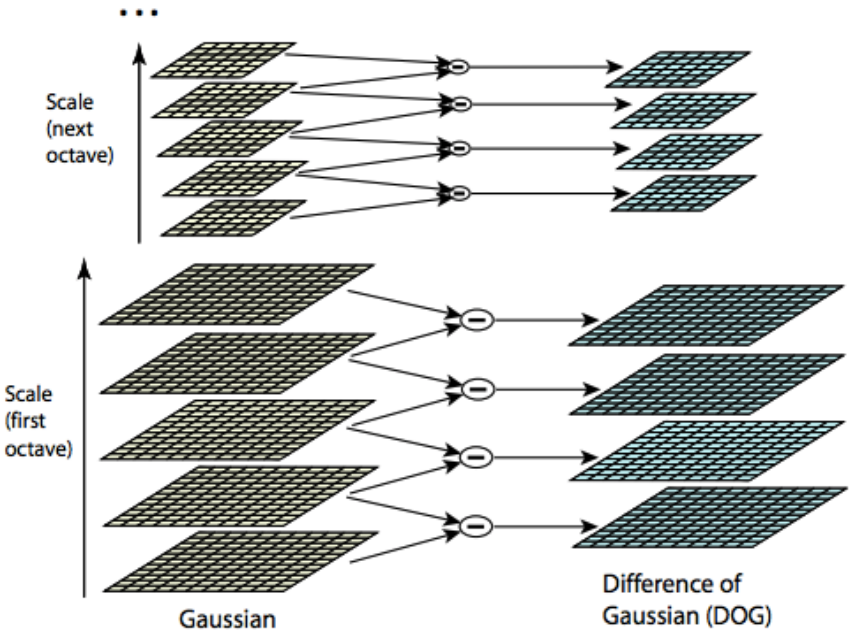

Figure 3.12: The image is repeatedly convolved with Gaussians for every octave to generate multiple scale space images, which are shown on the left. After that the adjoining Gaussian images are subtracted from each other to get the DoG images on the right. The sigmas of octaves are doubled up for every next octave and the process is repeated [41].

In addition the DoG function delivers a good approximation to the scale normalized Laplacian of Gaussian $\sigma^2 \bigtriangledown^2 G$. The derivation $dG/d\sigma$ can be approximated with the difference quotient pretty well, as the differences of the scales are taken, which are beside each other:

$$G(x, y, q\sigma) - G(x, y, \sigma)) \approx (q - 1)\sigma^2 \bigtriangledown^2 G \tag{48}$$

Because q is constant over all scales it does not influence the positions of extrema. The approximation error vanishes when q takes a value close to 1.

To identify the local maximas and minimas of $D(x, y, \sigma)$, every single sample point is compared to its eight neighbors in the current image and nine neighbors in the scale above and below, what is shown in Fig. 3.13. Only in the case of the specific sample is larger or smaller than all of its neighbors it is selected. For this step, not so much calculation has to be done, because most sample points are already sorted out after the first few checks [41].

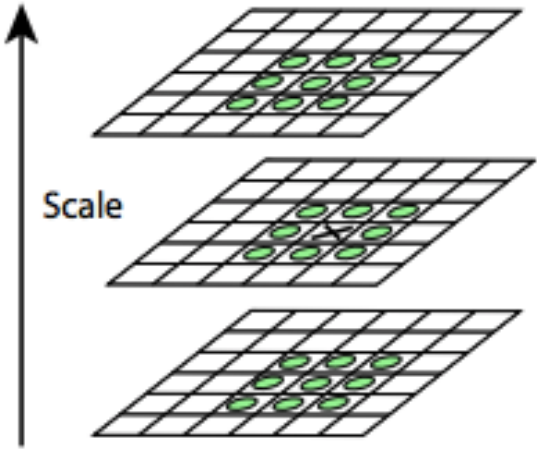

Figure 3.13: The maxima and minima of DoG functions are calculated by comparing pixels (X) with its 26 neighbors (green dots) in 3x3 regions in the current and adjoining scales [41].

Transforming image points

What is needed is a transformation of specific points from a picture A (x_a, y_a) to a picture B (x_b, y_b). This affine transformation is defined as

$$\begin{bmatrix} x_a \\ y_a \end{bmatrix} = \begin{bmatrix} m1 & m2 \\ m3 & m4 \end{bmatrix} \begin{bmatrix} x_b \\ y_b \end{bmatrix} + \begin{bmatrix} tx \\ ty \end{bmatrix} \tag{49}$$

where (tx, ty) describes the translation between the points and the parameters m_i the affine rotations, scales and stretches. In order to solve this linear equations, eq. (49) is rewritten as

$$\begin{bmatrix} x_b & y_b & 0 & 0 & 1 & 0 \\ 0 & 0 & x_b & y_b & 0 & 1 \\ \dots & & & & & \\ \dots & & & & & \end{bmatrix} \begin{bmatrix} m1 \\ m2 \\ m3 \\ m4 \\ tx \\ ty \end{bmatrix} = \begin{bmatrix} x_a \\ y_a \\ . \\ . \end{bmatrix} . \tag{50}$$

Regarding this, it is only possible to find the 6 unknown transformation parameters, if at least three points are identified in both pictures. This linear system can be rewritten in the form of

$$T\hat{\xi} \approx a \tag{51}$$

where T is the $m \times n$ translation matrix, containing the points of picture B. Vector $\hat{\xi}$ is the searched for $n-$dimensional parameter vector and a the $m-$dimensional

vector containing the points of picture A. To solve eq. (51) a little trick is needed and the so-called normal equation (see [41]) is used as

$$T^T T\hat{\xi} = T^T a \; . \tag{52}$$

By rearanging the equation to the form of

$$\hat{\xi} = (T^T T)^{-1} T^T a \tag{53}$$

the solution is found by multiplying the pseudoinverse of T with the measurement vector a, which also is the least square solution [41].

3.5.2 Back projection method

The basic idea was to use the GNSS data to locate the rover in three dimensional space and correct it with the Kalman filter. Moreover, to measure the rover's orientation. To accomplish this, a global coordinate system was defined to describe the measurements of the IMU directly, moreover, a local (body) system was defined to transform the values (compare to Fig. 2.13) from the rotated IMU to the global system. The global system is the matrix $S_g(\vec{x_g}, \vec{y_g}, \vec{z_g})$ containing three normalized unit vectors $\vec{x_g}$, $\vec{y_g}$ and $\vec{z_g}$, where the z-direction is defined as the normalized gravitation, the x-direction the horizontal north, and the y-direction is the normalized cross product of these two. The local system S_l is built up from the same, but current measurement vectors.

The acceleration sensor has some considerable fluctuations, that is why before every update of the global system, the software checks the value of the acceleration deviation. If the deviation reaches a specified boundary value, a weighing factor w increases and the new global system is calculated in slight modification as

$$S_g = S_g(1 - w) + S_{g,fresh} w \; . \tag{54}$$

where $S_{g,fresh}$ is defined as a new global system. The transformations from local- to global system are implemented by simply multiplying the measured values (acceleration, magnetization, gyroscope) with S_g. The rotation of S_g is realised by multiplying it with the product of the angular velocity tensor Ω and the timestep Δt which is in the range of $33\,ms$. The angular velocity tensor is defined as

$$\Omega = \begin{bmatrix} 0 & -\omega_z & \omega_y \\ \omega_z & 0 & -\omega_x \\ -\omega_y & \omega_x & 0 \end{bmatrix} \; . \tag{55}$$

Finally, the searched for system, containing the angular information, is found as

$$S_g = S_g \cdot \Omega \cdot \Delta t \; . \tag{56}$$

Knowing the location and orientation of the rover and also the distance to the object, the images can be rotated and projected to a particular plane as it is shown in Fig. 3.14. The position of the camera is $O : \vec{o}$, which is also called eye point. An object point P is backprojected to the point $P' : \vec{p'}$ and $\vec{n_0}$ is the vector pointing from the so-called main point $H : \vec{h}$ to O at a right angle. The two planes, that are the camera plane and the image plane, are stated as ε_c and ε. The normal vector is defined as $\vec{n_0} := (cos\, u\, cos\, v, sin\, u\, cos\, v, sin d\, v)$ where $u \epsilon [0, 2\pi]$ and v $[-\pi/2, \pi/2]$ [42].

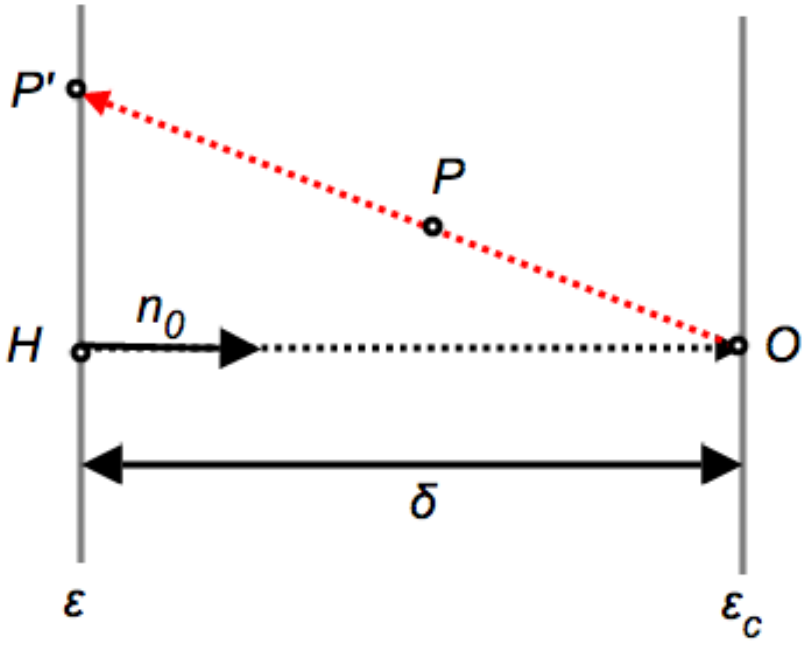

Figure 3.14: A point P is back projected to a plane ε.

The eye point can be written as

$$O = h + \delta \vec{n_0} \tag{57}$$

where δ is the distance from H to O. Two more unit vectors e_1 and e_2 are needed to build up an orhtonormal system $\{\vec{e_1}, \vec{e_2}, \vec{n_0}\}$ as it is shown in Fig 3.15. The central projection can then be excecuted in two steps. First, the coordinates of the point $P : \vec{p} = (x, y, z)$ has to be transformed to the system $(H, \vec{e_1}, \vec{e_2}, \vec{n_0})$ as

$$\vec{p} = (x, y, z) \rightarrow \vec{p'} = (x', y', z') \tag{58}$$

$$x' = (\vec{p} - \vec{h}) \cdot \vec{e_1}\ ,\ \ y' = (\vec{p} - \vec{h}) \cdot \vec{e_2}\ ,\ \ z' = (\vec{p} - \vec{h}) \cdot \vec{n_0}\ . \tag{59}$$

The second step is to perform the central projection in the system of $(H, \vec{e_1}, \vec{e_2}, \vec{n_0})$ to the $x'y'$-plane as

$$\vec{p'} = (x', y', z') \rightarrow \left(\frac{x'}{1 - z'/\delta}, \frac{y'}{1 - z'/\delta} \right) \tag{60}$$

[42].

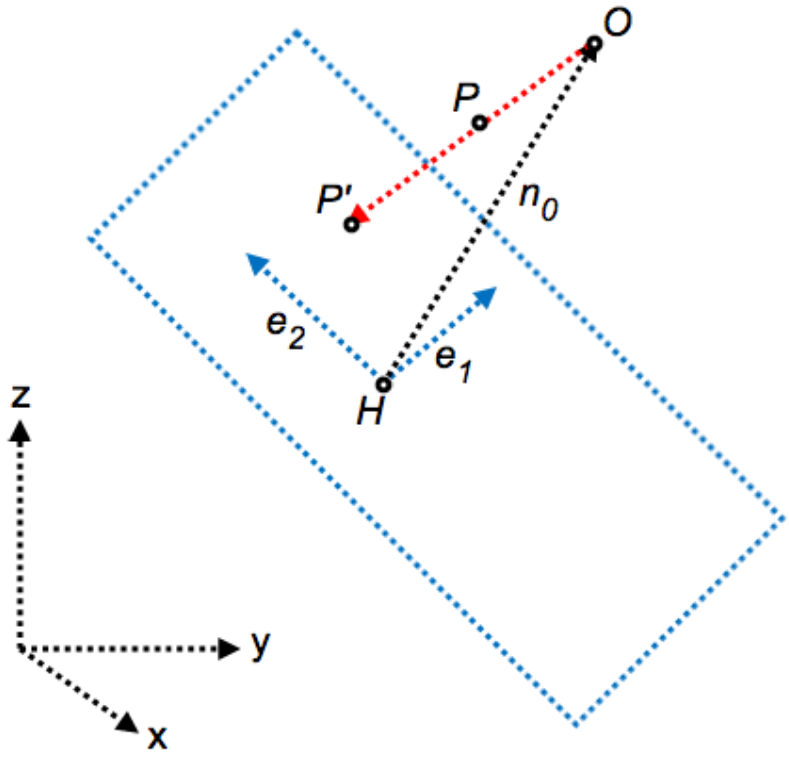

Figure 3.15: Central projection of a point P.

3.5.3 Correcting lens distortions

A vital point in processing the images is the effect of lens distortion. The two most common types of distortion, barrel- and pinscushion distortion, are represented in Fig. 3.16. Ideally, one would use a very small-angle lens to minimize the distortions, but on the other hand, what is wanted are many modules on one picture to minimze the amount of work, therefore, a wide-angle lens will be preferred.

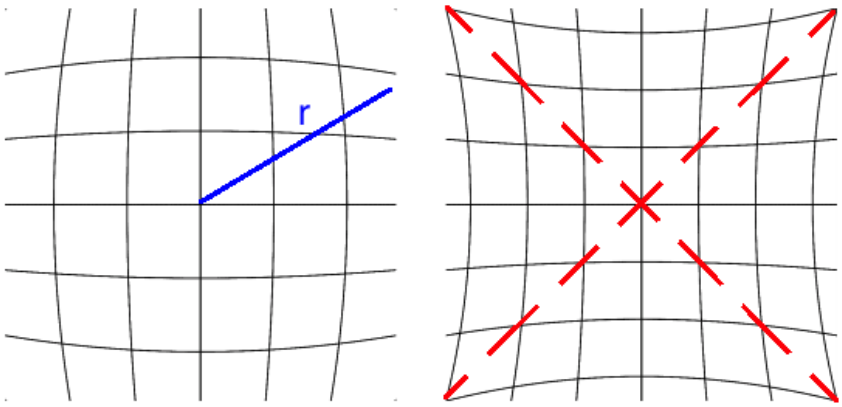

Figure 3.16: The image on the left side represents the barrel distortion, where image magnification is decreasing with distance from the center point of the image. For pincushion distortion (left image) it is the other way around. Delineated is the real distance r from the center, which has to be transformed. The red lines indicate that there is no distortion for the diagonal elements [43].

From a mathematical point of view, it makes sense to treat this problem in polar coordinates, because of the radial symmetrie of the lens. The main axis is placed in the center of the image and a right angle is assumed. A correction function $f(r)$ has to be defined. This so-called distortion function is camera specific, as a result of manufacturing tolerances in regard to the mutual mounting of the camera sensor and the lens. The relationshsip between the physical coordinates of a pixel (x, y) and the coordinates of the real perspective are described by

$$\hat{r}^2 = \hat{x}^2 + \hat{y}^2 \tag{61}$$

$$\hat{r} = f(r)r \tag{62}$$

where the pixel $(\hat{x}, \hat{y})$ describes the actual point of the ideal perspective, $\hat{r}$ the corresponding distance from center and r the measured distance of the pixel in the distorted picture. A polynomial approach is used for the correction function

$$f(r) = 1 + a_1 r^2 + a_2 r^4 + a_3 r^6 \tag{63}$$

wheras a_i are the camera specific parameters. Only even powers are used, which is leading to best results [43].

3.6 Measurement procedure

The steps of the measurement process are graphically illustrated in Fig. 3.17. As it is indicated, the base station is used to perform the carrier phase measurements and, therefore, delivers the static GNSS data. Also, the pressure data is important, because low- or high pressure areas can lead to pressure-, and hence altitude changes in the range of multiple meters within a few hours (see Fig. 3.11). Before starting to take images it is important to wait for at least 3 min, so the RTK system can solve the integer ambiguity resolution and a position fix is found.

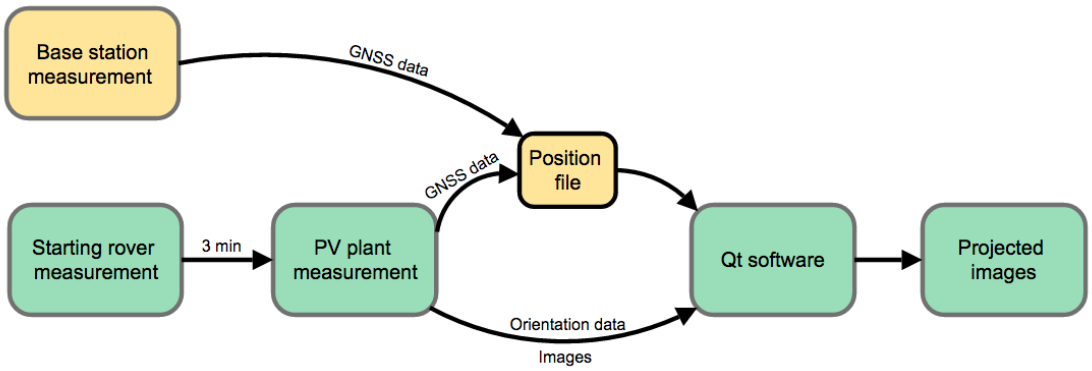

Figure 3.17: The basic steps of a measurement with the developed system.

The data from both components, rover and base station are stored on a SD-card. Before it is processed in a Qt software, a position file containing the coordinates of the three dimensional position and the GNSS time has to be generated by using the RTKLIB software. The API RTKCONV is used to produce the Rinex observation files. These files are then used to calculate the position file with the API RTKPOST, where the options discussed in section 3.2.3 are used. Finally, the developed Qt application makes it possible to load all relevant data and process it in a graphical user interface.

4 Results

In the following sections, first the results of the sensor characterisations and the process of reaching the most efficient settings for the built system are shown. In the second part, the results of the integration measurements and the implemented Kalman filter are discussed. The last part consists of a field measurement where all developed software was tested including the backprojection algorithm.

4.1 GNSS measurement

To test how accurate the used GNSS module is, position and satellites in view were logged onto a SD card over a weekend at a measurement frequency of 1 Hz. In total 250000 measurements are plotted in Fig. 4.1 what roughly corresponds to 2.9 days. Longitude and latitude were converted to meters for better visibility of measurement deviations. It was caluculated assuming the earth was a sphere, then calculating the arc length at an earth radius of $R_{Earth} = 6371$ km.

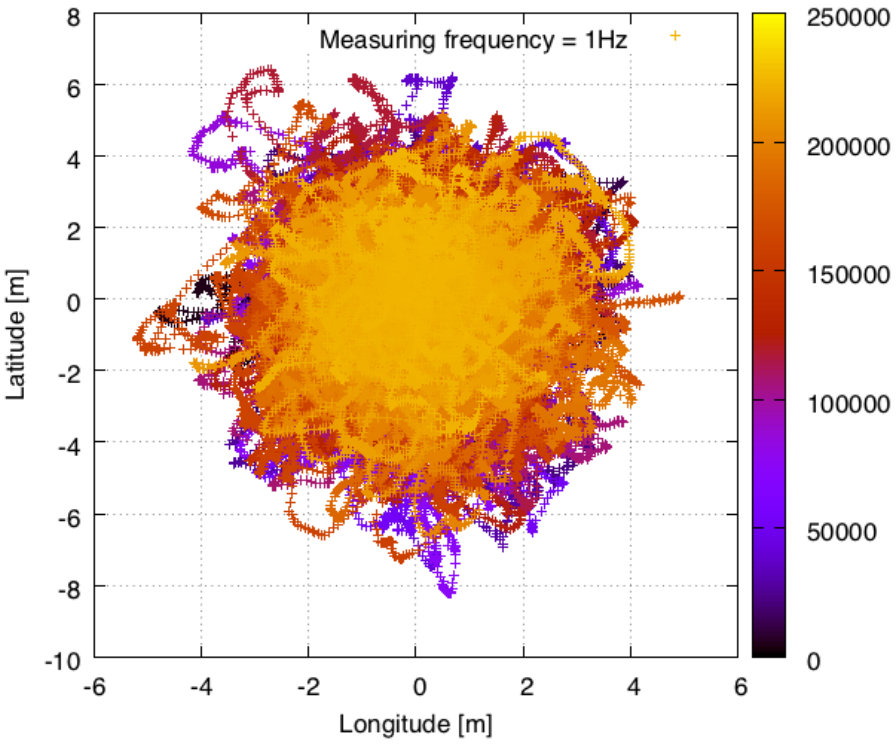

Figure 4.1: Weekend position measurement at a frequency of 1 Hz for a fixed location on the roof of AIT building. It corresponds to the worst case of a single detector measurement.

For converting the longitude, the arc length was multiplied by the cosine of lati-

tude in degrees to compensate the effect, that the perimeter is changing with higher angles. The mean measured positioning value was shifted to the zero point in the graph. The position deviations are in the range of 4-6 meters. A little deeper look into the data showed, that the position measurements are normally distributed around the fixed location (48°16'7.06"N, 16°25'37.72"E) . The calculated standard deviations are $\sigma_x = 1.173\,m$ for longitude and $\sigma_y = 1.682\,m$ for latitude. In Fig. 4.2 the position measurement is plotted with subtracted means for longitude and latitude. The plot shows that the first result in Fig. 4.1 is a bit misleading, as it indicates a wide distribution. This is not really the case, as $\pm\sigma$ is defined as the interval where 68.27 % of the measured values are found.

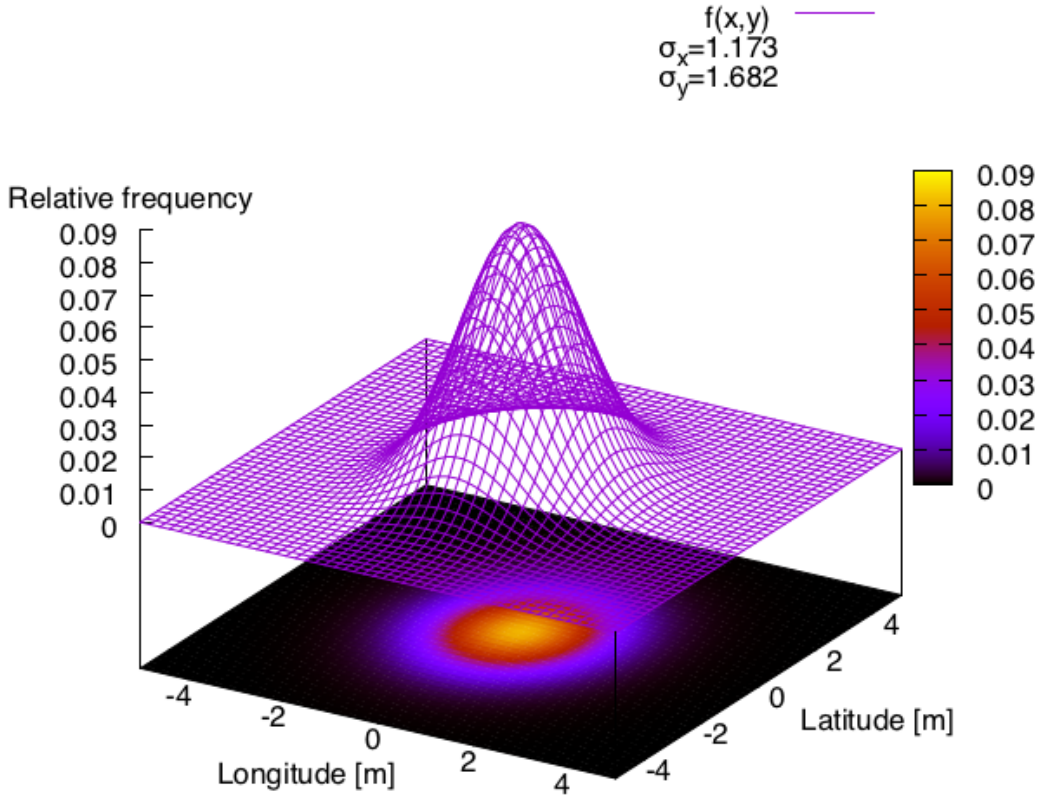

Figure 4.2: The gaussian distribution of position measurement in two dimensions. The standard deviation for latitude σ_y is higher than for the longitude σ_x by more than 0.5 m.

4.2 Differential carrier phase measurements

To minimize the drift, the carrier phase full cycles were measured and compared by two GNSS modules (base and rover), as it is explained in the theory section 2.5. For static base and rover, at a baseline of 1 m, an accuracy of around 2 cm was reached. In fact standard deviations of $\sigma_x = 0.0050\,m$ (east), $\sigma_y = 0.0046\,m$ (north) and $\sigma_z = 0.0110\,m$ (up) were achieved. The measurment is depicted in Fig. 4.3. On the top right section of the plot the statistics of the position measurement are shown, where the most important parameters are the standard deviations (STD) for the three dimensions of space. This result could be achieved without any metallic shield, when the GNSS sensors were lying in a gras field. It has to be emphasised that the RTK measurement was only running for about 13 min (780 measuring points), in contrast to the conventional GNSS measurement (Fig. 4.2), which was conducted for 69.4 hours.

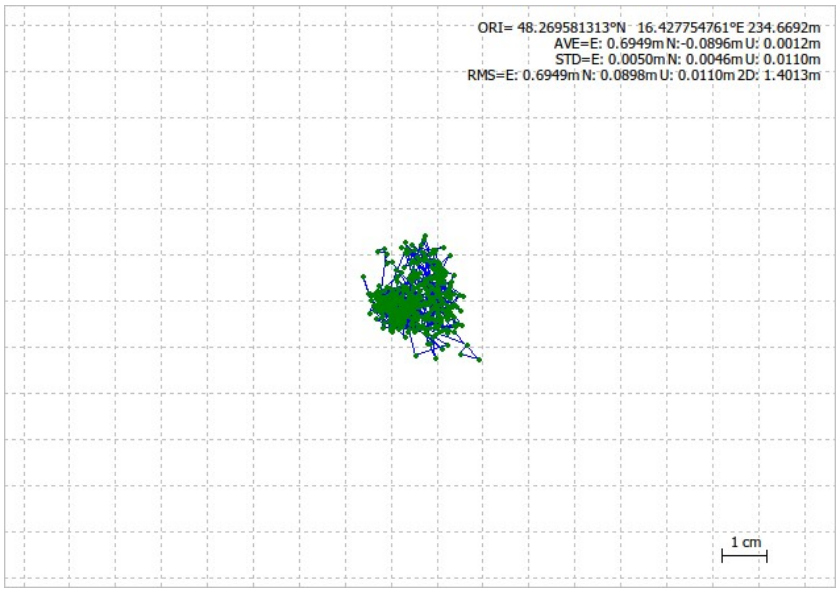

Figure 4.3: First RTKLIB test for static base station and rover at a baseline of 1 m.

The signal was stable at this position for more than 10 min. Such high precission couldn't always be reached, because of the many possible influences like TEC, weather changes, wind gusts, MP-effects and so on. The result was achieved using the RTKLIB application STRSVR (streamserver) for both microcontroller systems. Later results are produced by making use of specifically written arduino software. A problem which appeared, but is not visible in the plot was the time it took to get this clean positioning fix, which is discussed in the next section.

4.2.1 Time to fix position

The first differential carrier phase measurements showed that it needs some time to get an accurate positioning fix, when starting a new measurement. Fig. 4.4 shows

the deviation of the signal and as it slowly finds the actual position. It was found, that it depends a lot on the number of available satellites and their location on the sphere of space.

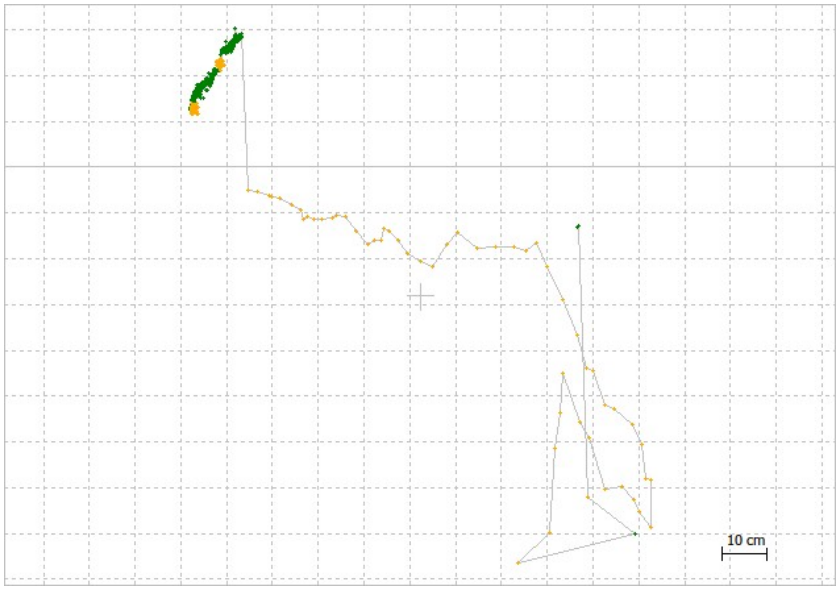

Figure 4.4: The drifting signal before it finds the true position of the rover.

In this measurement the position fix was lost again after about a time of 3 minutes. This was due to multiple cycle slips in the phase measurements. The good thing is that it took only 1.5 minutes to find a position fix again. Anyway, it is clearly visible that the believed position is moving for multiple centimeters, even if a fix is produced. Such offset movings were only observed, when the rover was held still.

However, to make sure that the rover is located at an accurate position, it is necessary to wait for at least three minutes, as it is floating around. The measurements showed that after this timeframe it can still happen that the position is lost, due to cycle slips or other irregularities, but in general the position then is known quite accurately. The progressions of the curves look different every time proceeding to all different directions. It can be stated that the algorithm, comrpsing a Kalman filter, needs around 3 minutes to converge.

4.2.2 Comparison of single GNSS sensor and DGNSS

In Fig. 4.5 the blue line indicates the assumed location of the rover, considering only conventional GNSS. It is embedded in the grey, dashed ellipse. The yellow (float) and the green (fix) line indicate the position, calculated through the carrier phase measurement. The color of the line again changes from yellow to green after a position fix is found. Then the rover is located very precisely, but also before that, the position is known much better than the one of the conventional GNSS

measurement. The black dot in the top center of the plot indicates the position of the base station. In this measurement, both the base station and the rover were held still at a distance of 70 cm.

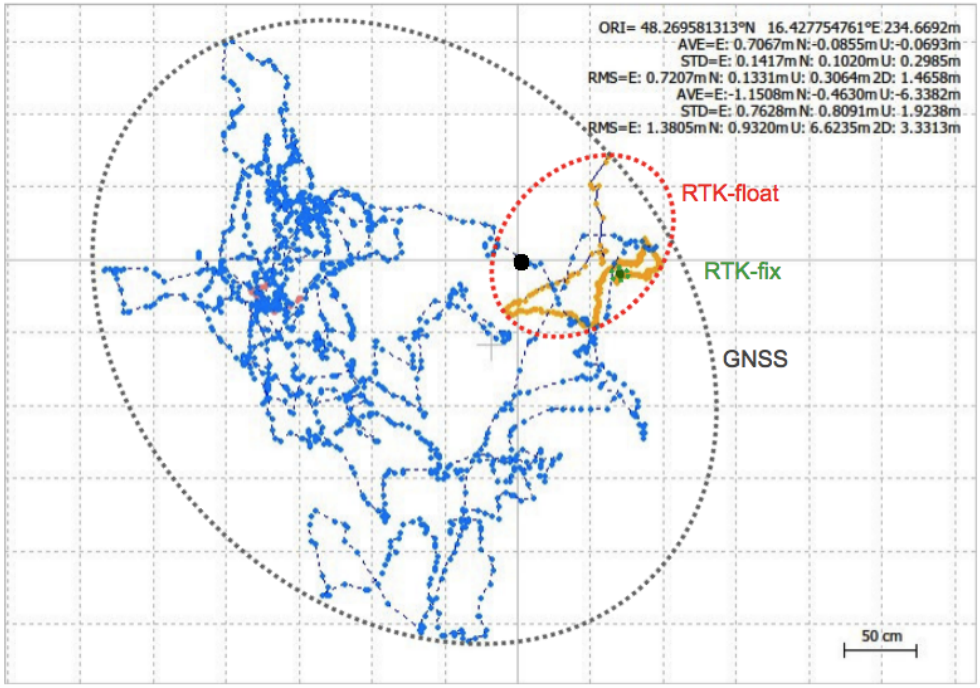

Figure 4.5: The comparison of the conventional GNSS- and the DGNSS measurement shows much higher accuracy for DGNSS. Especially, when a fix is found, the position is known very accurately.

Even if including the floating position measurements in the carrier-phase measurement and therefore the deviations from the real position the standard deviation in all three dimensions is smaller by a factor of 0.185 m. In the graph it is also shown that the single GNSS measurement for this case is very inaccurate as the most measurement points are shifted to the left from the actual position. It is conceivable that disruptive ionospheric conditions lead to the detected offset, which could be corrected by the method of differentiating the signals.

4.2.3 Moving rover

In the next step, the rover was carried in the hand and slowly moved on defined lines. It was attempted to hold the rover at a constant altitude of about 1.1 m. Before it was taken from the ground it was placed on the ground and held still for some minutes, so it was much easier for the system to solve the ambiguity problem and find the position. The result as a two dimensional (x-y) representation is shown in Fig. 4.6. The grey ellipses indicate the uncertainties of the measured positions. They are getting smaller with each measurement until the almost exact position from the rover is found, which at this point is not yet moving. The GNSS sensor was then

taken from the ground at the time of 10:40 (see also Fig.4.7) and slowly moved around. The position fix is only lost at one edge of the moved line, anyway, the uncertainty does not grow too fast and is not even visible in the plot. Already after one second, a position fix could be established again. This is possible because only the signals with the best signal quality are incorporated into the position solution.

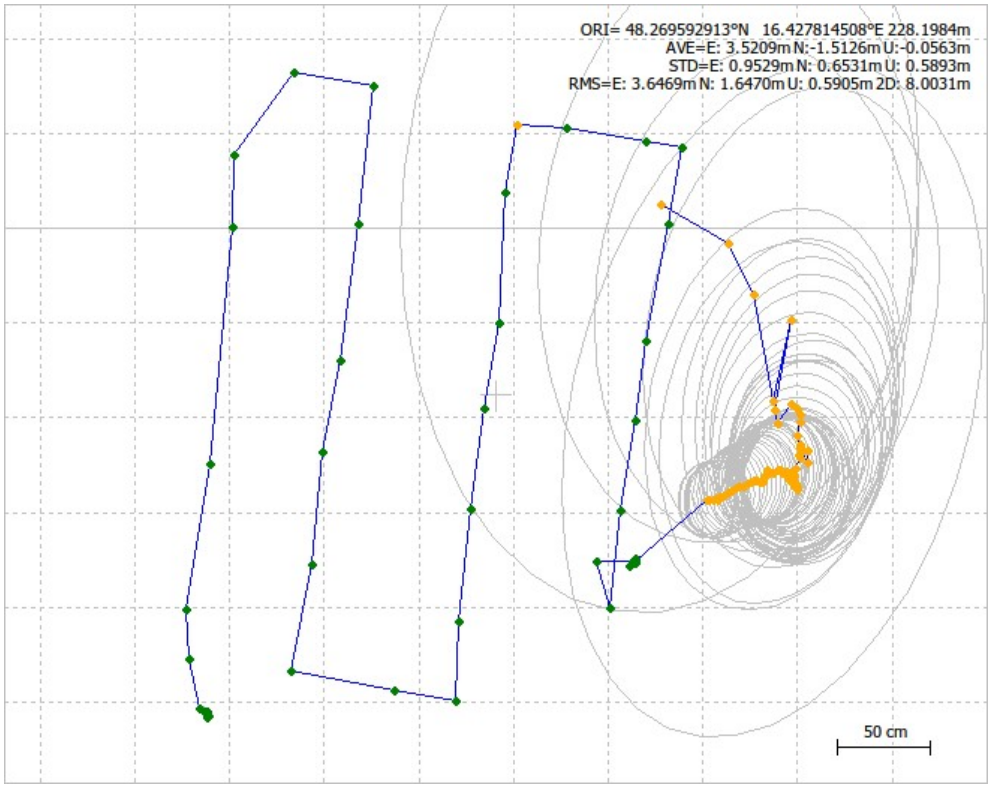

Figure 4.6: Result of a moving rover at a baseline of 1-3.5 m. The uncertainties initially decrease with every timestep of 1 s.

The same measurement is represented in altitude presentation in Fig. 4.7, where it is properly visible how long the rover was lying still and when it was picked up and moved around. This result shows that not only the position in two-dimensions, but also in three dimensional space can be figured out pretty accurately.

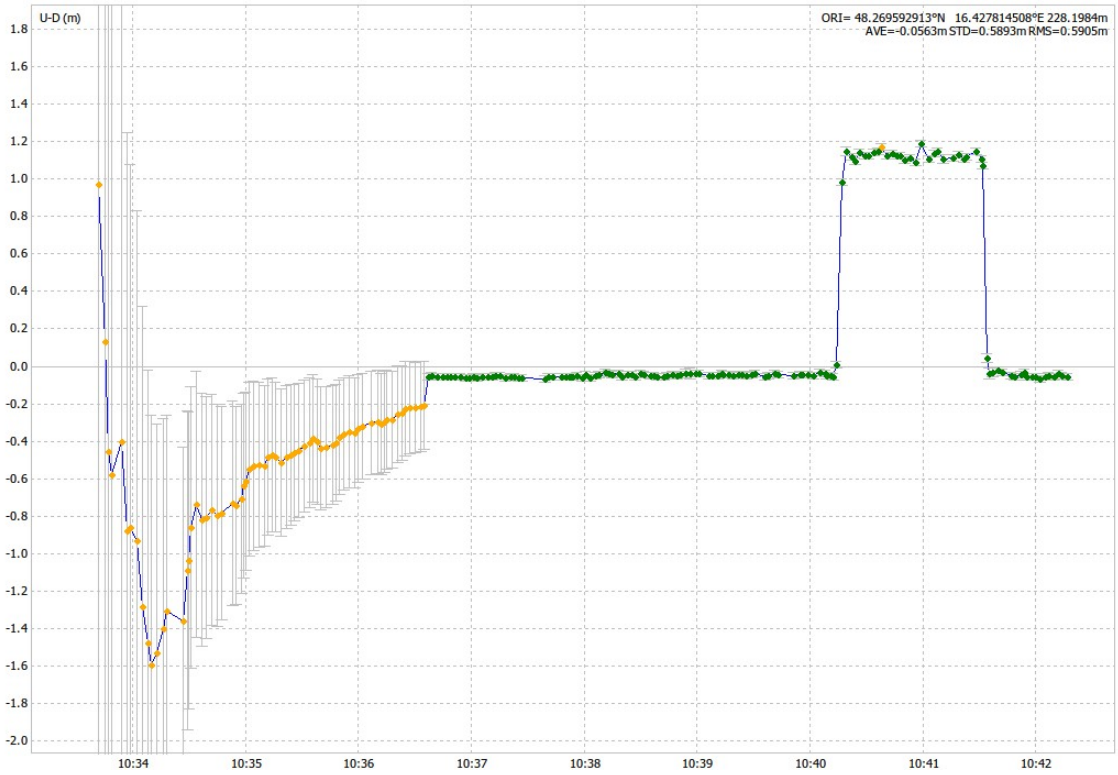

Figure 4.7: The altitude representation in the case of a moving rover on specific lines. It was placed on the ground at the beginning of the measurement, so it could find a position fix (∼10:36:30). At the time of ∼10:40:10 it was picked from the ground and carried around on the lines.

4.2.4 Error analysis

In principle, the GNSS system is working as it is supposed to be, but some delicate circumstances can appear and have to be considered.

Cycle slips (CS)

Discontinuities in the carrier-phase measurement lead to cycle slips and worsen the position measurment tremendously. Therefore, several different undergrounds and their impacts were tested to make sure the GNSS module is shielded optimally from multipath rays and other interference radiation. In the first test the GNSS module was placed on concrete for two minutes, then, an aluminium plate was slided in underneath for another two minutes. In the last step, the module was placed in grass. The results are shown in Fig. 4.8, where the black lines indicate the time frames of two minutes. Every horizontal line stands for a specific satellite. The ones indicated with ”G” are the GPS satellites, the ones starting with ”R” are the russian GLONASS and the ones only composed by a number are SBAS satellites. In this measurement, the GPS satellites were found very quickly but containd far

too many cycle slips for an accurate evaluation. Only after one minute the first GLONASS satellites are located. After the aluminium shield was placed underneath the module, a lot less CS appeard and a usefull measurement could be performed. Anyway, some of the satellites, GPS as well as GLONASS, contain CS which worsen the phase measurements. As the module was placed in the grass, only a few of the GLONASS satellites produce usefull information, where the GPS satellites are not able to provide the module with a stable signal. There are many different reasons for CS to appear, which are discussed in more detail after further results.

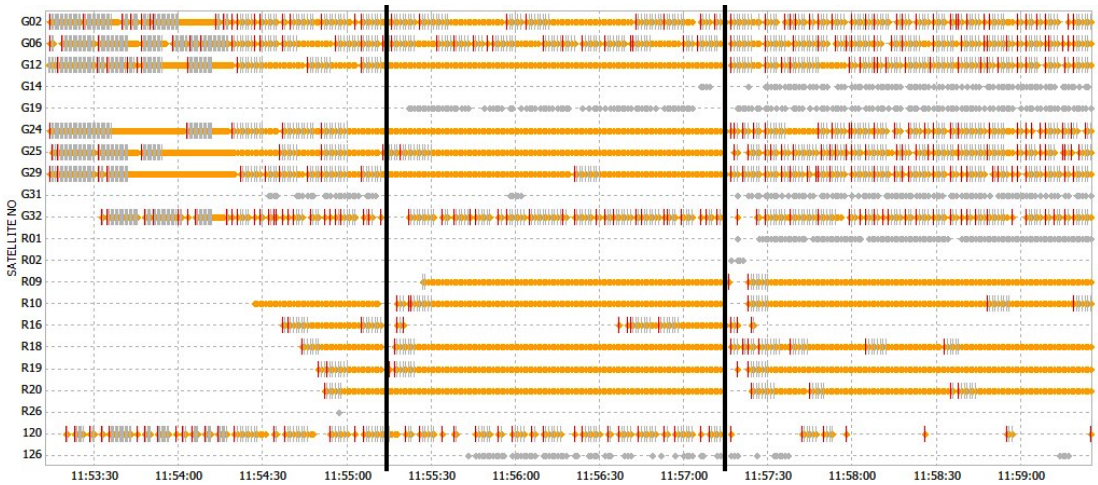

Figure 4.8: Occurrance of CS at different undergrounds. The first two minutes (until the black line) the GNSS antenna was lying on concrete. In the middle part, an aluminium disk was placed underneath it. For the last two minutes the antenna was placed in grass.

In the next step, different materials were tested for their abbilities to block of GNSS multipath rays and scattered radiation coming from the microcontroller itself or from other sources. Three different metallic plates were tested as groundplates for the GNSS module. That were (a) $35\,\mu m$ copper, (b) $3\,mm$ dibond composite and (c) $2\,mm$ aluminium. Every measurement was executed for 20 min as it is shown in Fig. 4.9. The best results could be achieved using the copper plate, whereby it is important to keep in mind, that the measurements were not carried out simultaneously, but one material was testet after another. This means that the constellations of satellites, TEC (2.4.2), atmospheric humidity and other stray radiation had already changed.

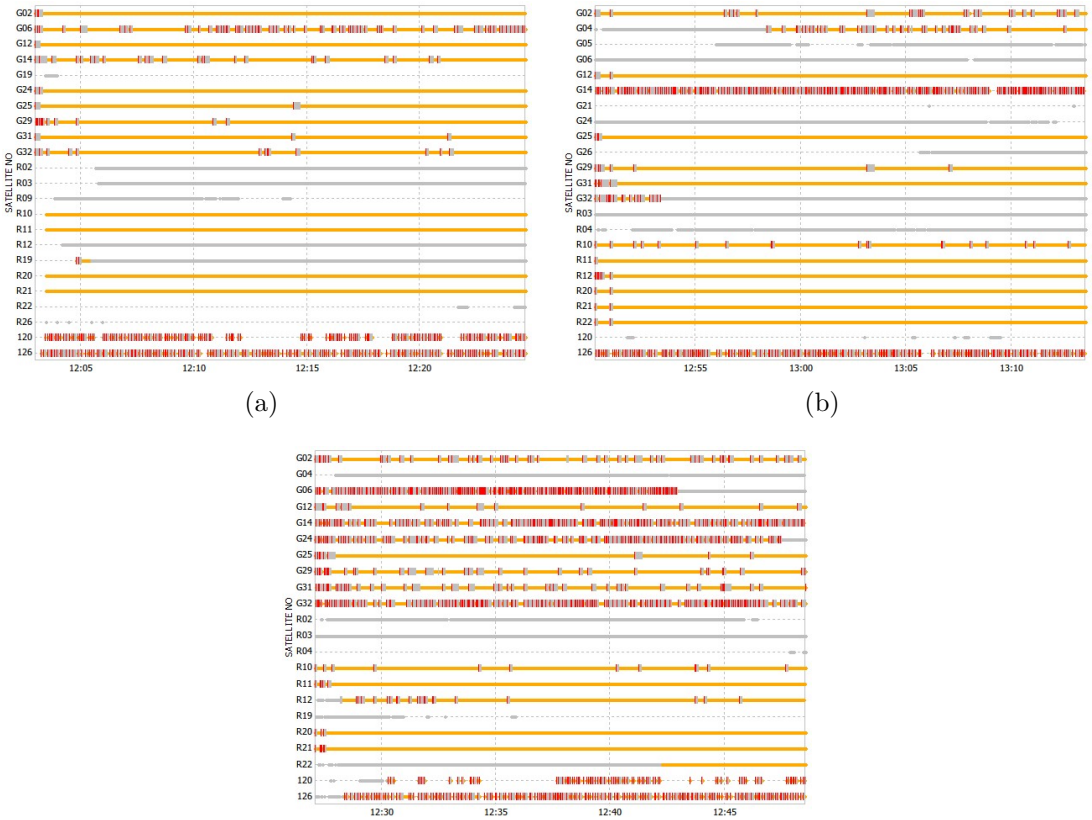

Figure 4.9: Received data streams for multiple different used shielding plates: (a) copper, (b) dibond, (c) aluminum.

For a more illustrative comparison the amount of CS per minute was calculated for the three different plates. This could be done by using a script, looking for the appeared cycle slips, which can be found in the observation file. The results are presented in table 2. Copper cleary delivered the best results with only about 5.8 CS/min. These values are summed up for all visible satellites. The SBAS satellites were omitted, because they weren't used in the post processing. If more satellites are visible at a specific time frame, the chance is higher that CS are measured. For this reason, CS/min only delivers meaningful results, when different shielding plates are tested back to back, therefore the visible satellites approximately are the same in every measurement.

Table 2: Amount of cycle slips for different underground shielding plates.

Shielding plate	CS/min
Copper	5.8
Dibond	14.2
Aluminium	36.4

It is remarkable that, for example, the GPS satellite G14 delivered a pretty good result with only a few CS, when the copper plate was placed beneath it. Contrary to that, the same satellite produced CS over the whole time frame of 20 min, when the dibond plate was used as the shielding. It was not possible to find out what lead to this result.

Dilution of position (DOP)

Dilution of precision is not just dependent on the constellation of the satellites, but also changes with different undergound shieldings. The comparison of copper and aluminium as undergounds is shown in Fig. 4.10 and Fig. 4.11, respectively. The different colors indicate the different DOP parameters explained in table 1, where the yellow points indicate GDOP, pink stands for PDOP, red for VDOP and blue for HDOP. Consequently, the paramters of DOP are directly dependent to the amount of appearing cycle slips and are increasing with them.

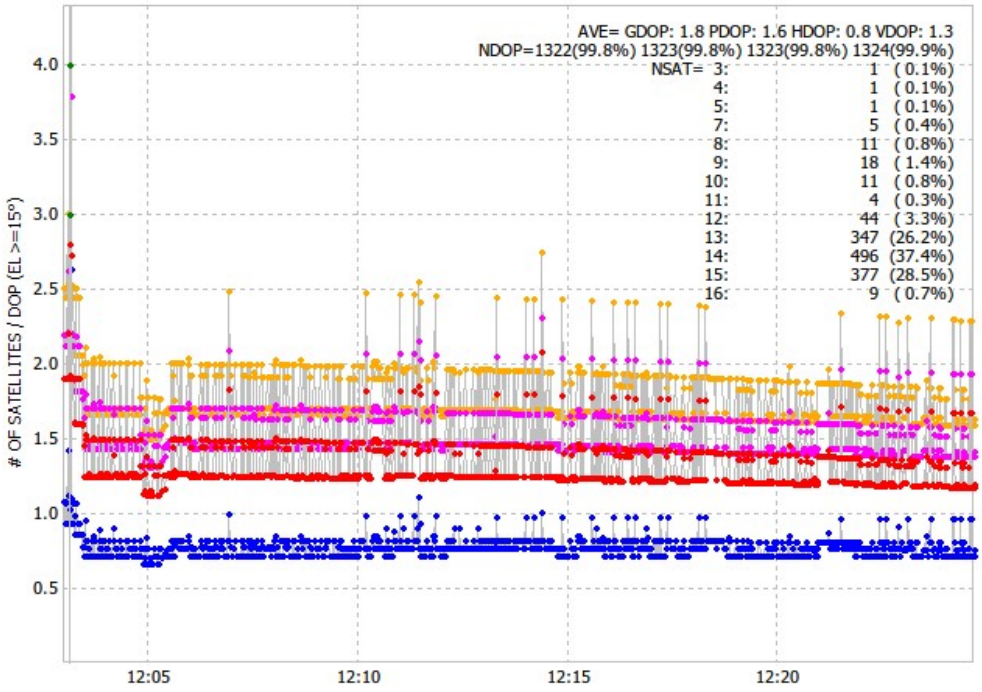

Figure 4.10: Copper plate: Representation of signals from all operating GPS- and GLONASS satellites in earths orbit. Every line idicates one satellite, where the grey parts represent the time, when the elevation angle of a satellite was smaller than 15°.

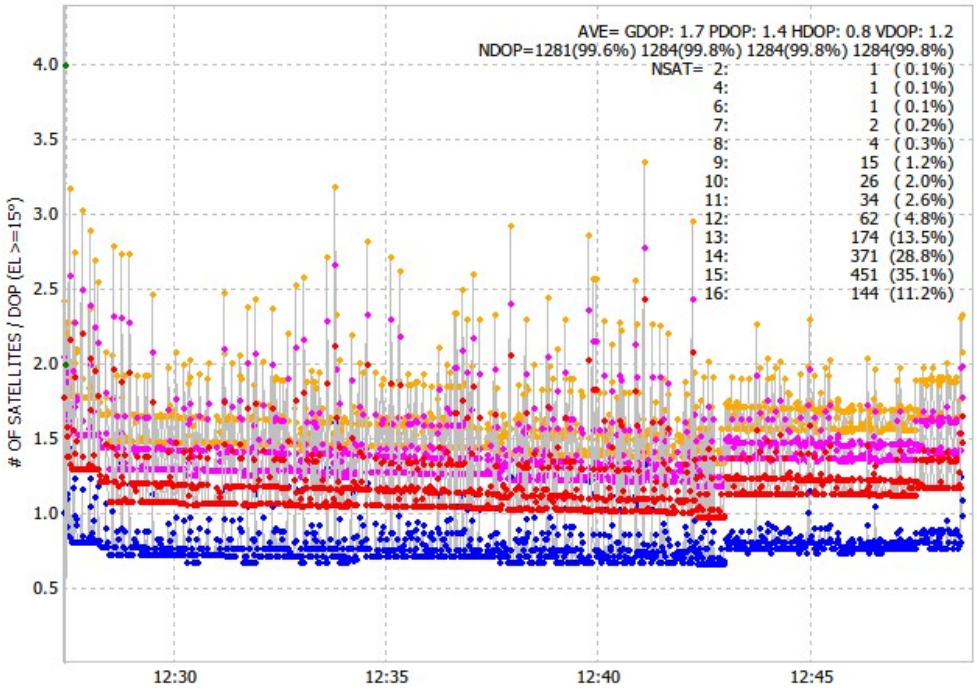

Figure 4.11: Aluminum plate: Representation of signals from all operating GPS- and GLONASS satellites in earths orbit. Again, every line idicates one satellite, where the grey parts represent the time, when the elevation angle of a satellite was smaller than 15°.

The statistics depicted on the top right corners of the plots indicate how many satellites were in use while the measurements were happening. For example, in Fig. 4.10 15 satellites were active, which contributed to 377 position measurements, what means that for 28.5 % of the time, 15 varying satellites were in use.

The DOP values are a lot smaller and, therefore, much better for the copper plate, although the constellation of the satellites have only changed slightly. The most important parameter is GDOP (yellow points), as it describes the accuracy of geometric position plus time. It was a lot more stable for the copper plate, where it is noticeable that all different DOP values reduce for the aluminium plate, after another stable satellite signal is received at the time between 12:42 pm and 12:43 pm.

4.2.5 Long term measurements

A long term measurement was conducted overnight to see and analyze the behaviour of the system and the signals from different satellites. As it is shown in Fig. 4.12, over the time frame of around 10 hours, all 32 GPS satellites, which are currently flying in the orbit of earth, could be tracked. Also, all 24 operating GLONASS satellites

were traced by the microcontroller system. The signals for GLONASS satellites contain a lot more cycle slips, this was not the continous case for the conducted measurements and was actually only observed at night. During the day it was often the case that the GLONASS satellites delivered better and more stable signals than the GPS satellites.

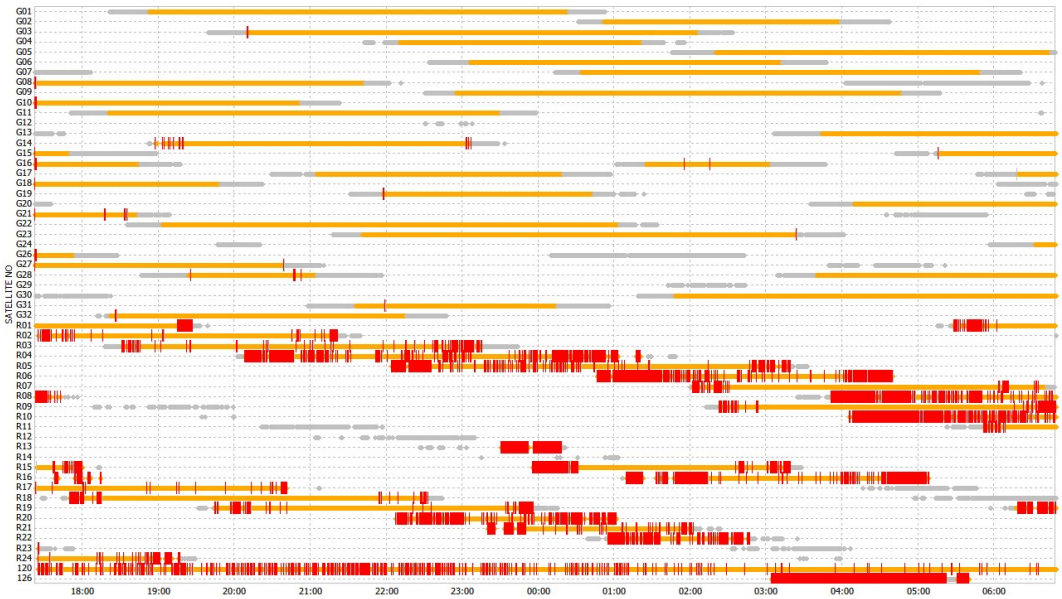

Figure 4.12: Representation of signals from all operating GPS- and GLONASS satellites in earths orbit. Every line idicates one satellite, where the grey parts represent the time, when the elevation angle of a satellite was smaller than 15°.

The satellite orbits are represented for the same overnight measurement in Fig. 4.13. The circle illustrates the earths sphere, where the last area of the sphere, which represents the satellites at an elevation angle $< 15°$, is grey, because it is not used for the evaluation. It is noticeable that the smaller the elevation angle, the more cycle slips do appear, which makes sense, because the signals have to travel more time in noisy atmosphere and are also reflected or shielded more.

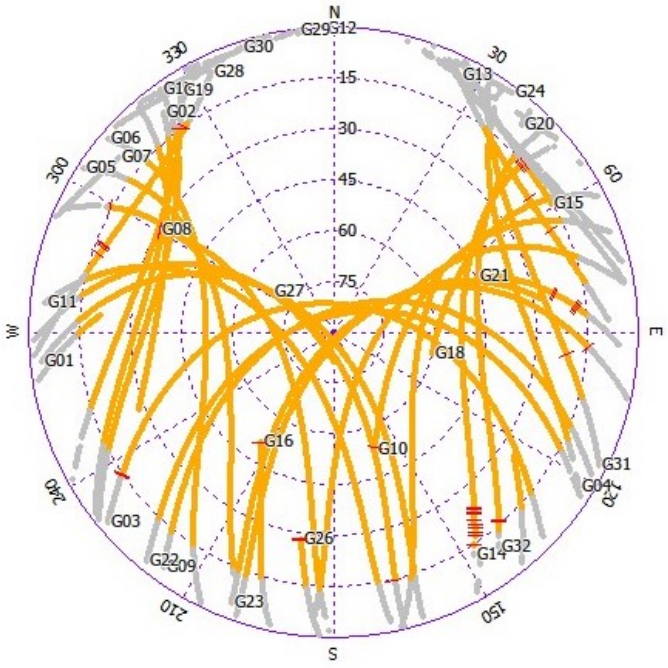

Figure 4.13: Satellites orbiting earth. The signals were very stable, but were getting weaker for smaller elevation angles.

The signal to noise ratios are in the range of 21-47 dBHz and do not really change over time. The plot at the bottom of Fig. 4.14 shows the dependency of elevation angle on SNR.

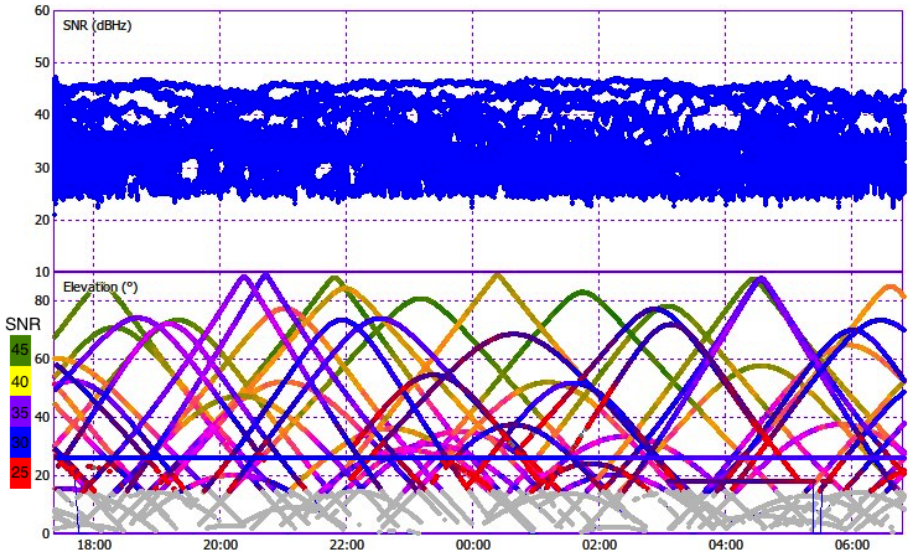

Figure 4.14: The upper plot shows the range of SNR over time. The lower graph represents the elevation angle for specific satellites at particular times, where the color indicates SNR. The blue horizontal line is the boundary line of SNR < 25.

Smaller SNR values are reached for satellites with high elevation angles, nevertheless, some can achieve SNR values > 40 even when orbiting on very low angles, like for example the satellite at 10 p.m. That means SNR is not only dependent on the elevation angle, but varies with different satellites or different atmospherics states, respectively.

More recognizable is the dependency of SNR on elevation angle in Fig. 4.15. In the end the curve drops again. The highest SNR and best signals could be reached for satellites at an elevation angle of about 75°.

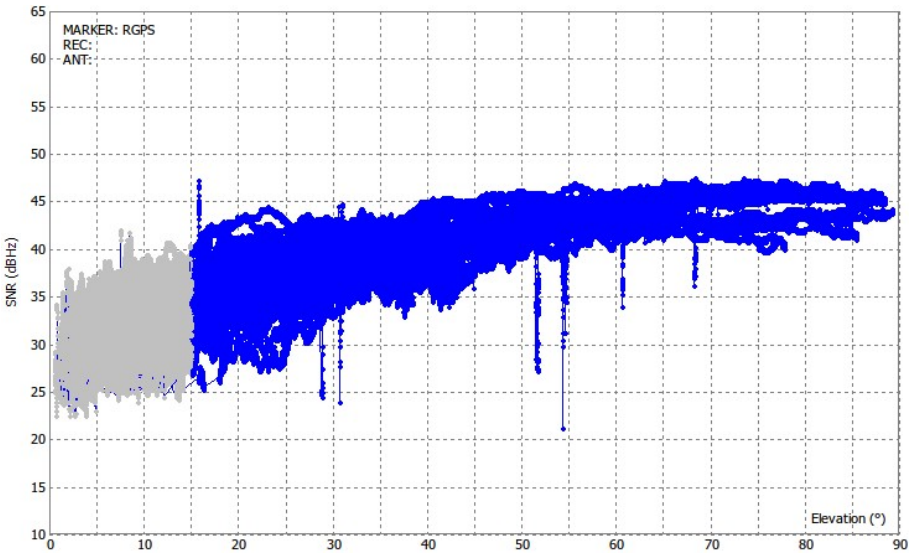

Figure 4.15: Signal to noise as a function of elevation angle, approximately, is a logarithmic function.

4.3 Integration measurements

The measurement principles explained in Fig. 2.13 were conducted to test if the acceleration signal was good enough to deliver a position measurement, which could be used in the Kalman filter, to update the location measurement.

The rover was walked slowly around the meeting room table in a rectangular path. The first evaluation approach was straightforward, where the angular information from the gyroscope was used to calculate the orientation of the rover. As the orientation was known, the acceleration values could be projected into the global coordinate system and corrected for gravity. The acceleration signals in x- and y- direction are shown in Fig. 4.16 (a), in (b) the double integrated acceleration and, therefore, the calculated position is plotted.

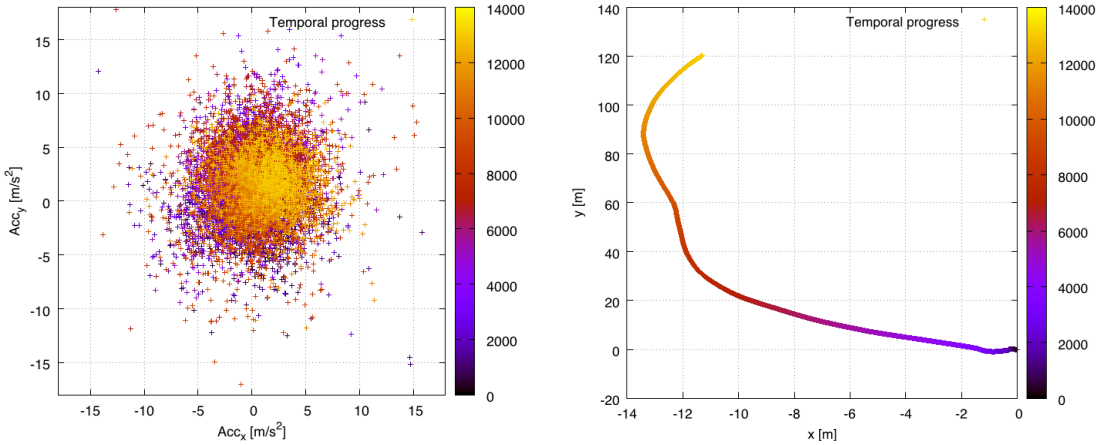

(a) (b)

Figure 4.16: In (a) the acceleration values are shown for x- and y-direction for the measurement scenario when walking around the $2.5 \times 4\,m^2$ table. In (b) the evaluated position is shown where the signal takes off at a certain point.

The physical starting point of the measurement was also the end point, which could not be achieved in the double integration. The signal suddenly elopes, especially in y-direction, because the orientation and therefore to projection onto the global axes was not conducted correctly. Thus, the gravity could not be subtracted as it was supposed to and a very wrong position estimation was produced. In Fig. 4.17 (a) the fluctuation of the acceleration values in z-direction around the gravitational acceleration are shown.

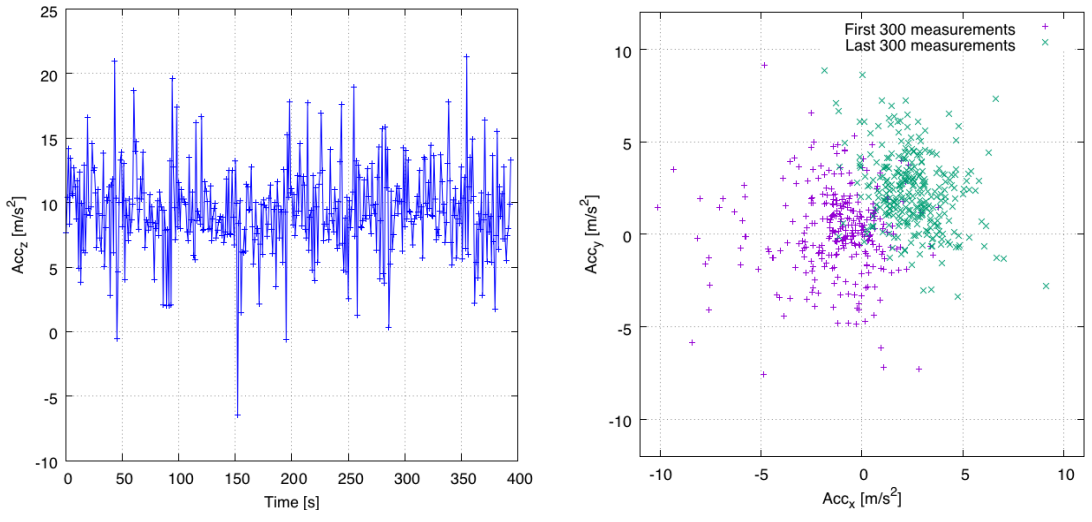

(a) (b)

Figure 4.17: Figure (a) represents the acceleration in z-direction where (b) shows the acceleration values of x- and y- direction for the first and last 300 measurements.

The big problems are not high accelerations in both directions, as long as they are symmetric, but this was not the case or could not be achieved as it is shown in Fig. 4.17 (b) for the x- and y-direction. Where at the beginning of the measurement the values are distributed symmetrically around the point of origin, for the last 300 measurement samples the gyroscope had generated an offset and misestimated the orientation. Thus, the gravitational acceleration is not subtracted correctly and it was integrated to a wrong direction.
The evaluation code was improved by introducing a verification parameter checking the value of acceleration for significant fluctuations:

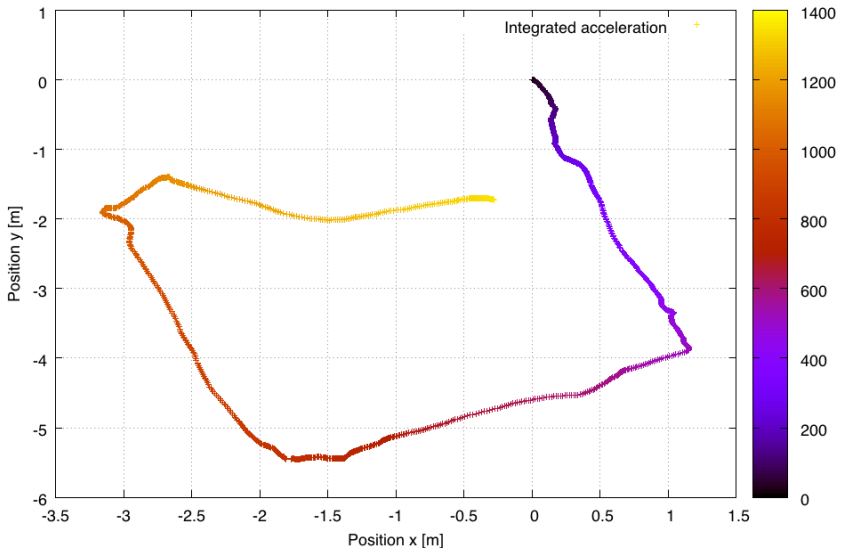

Figure 4.18: Position measurement calculated by double integration of the acceleration signals. The data was corrected with a verification parameter checking for high magnitudes of acceleration and setting a new normalized coordinate system after about every two seconds.

If very high absolute acceleration values were measured, a new normalized current system was calculated and the integration process went on from there. With this method, highly erroneous measurements and also the offset error which lead to the drift of the signal, shown in Fig. 4.16 (b), could be excluded. This lead to the result represented in Fig. 4.18. The scale of the result is realistic, anyway, on the last straight line coming back to the starting point, the signal went off to a false direction.

4.4 Altitude Kalman-filtering

The implementation of the Kalman-filter was a crucial point of this work, as it is very important to know the altitude for combining the pictures correctly as exact as possible. Different tests were performed, where two descriptive tests are shown and discussed in the following section.

Car measurement

To generate some pressure and altitude variations, the rover was placed under the front window of a car and transported up to a little hill near Stammersdorf, as it is shown in Fig. 4.19. While driving, the base-station was placed at the starting point of the measurement on a field. RTK positioning fixes could only be found a few times, because the road was obstructed with trees and other things, however, a high geometric accuracy could be achieved.

Figure 4.19: The RTK measured positions represented in Google Maps for driving around in the car.

The standard deviations of position measurements are represented in Fig. 4.20 or in the zoomed in version of Fig. 4.21. The purple line indicates the altitude measurements by the RTK evaluation, the green is the position calculated through pressure measurements and the blue line is the filtered signal. At the time of 17:36:00 the RTK measurements started to get inaccurate, because a bridge shielded the sensor and the sky was obstructed by trees much more than before. After that, the car was driven up to a little hill, the rover was taken out from the car and placed on a grapevine where it was held still for some minutes, before it was moved around again. Down hill, the RTK evaluating software had the same problem at the bottom of the hill that again detoriated the filtered signal.

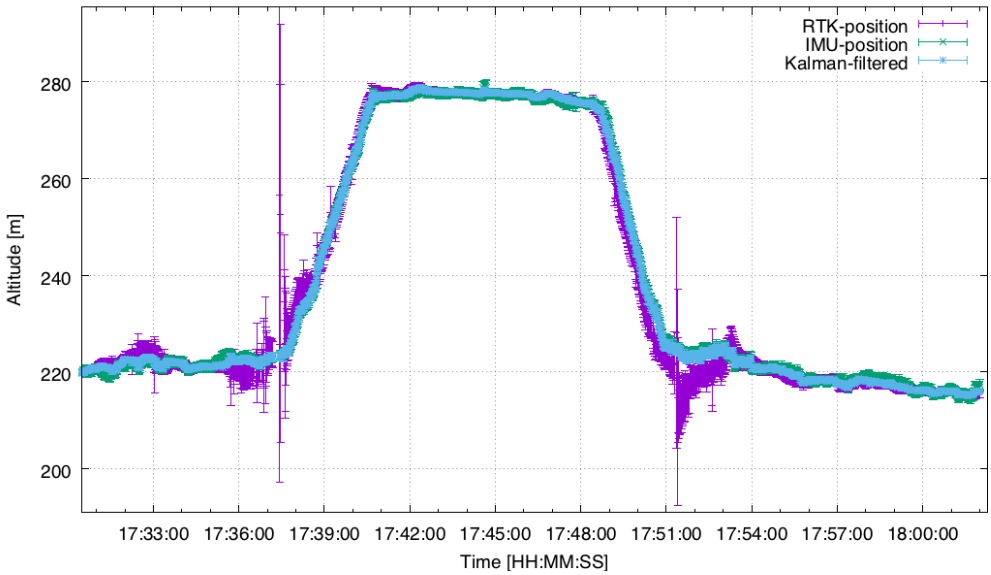

Figure 4.20: Altitude measurements by the RTK system, pressure values and the corrected signal by the Kalman-filter.

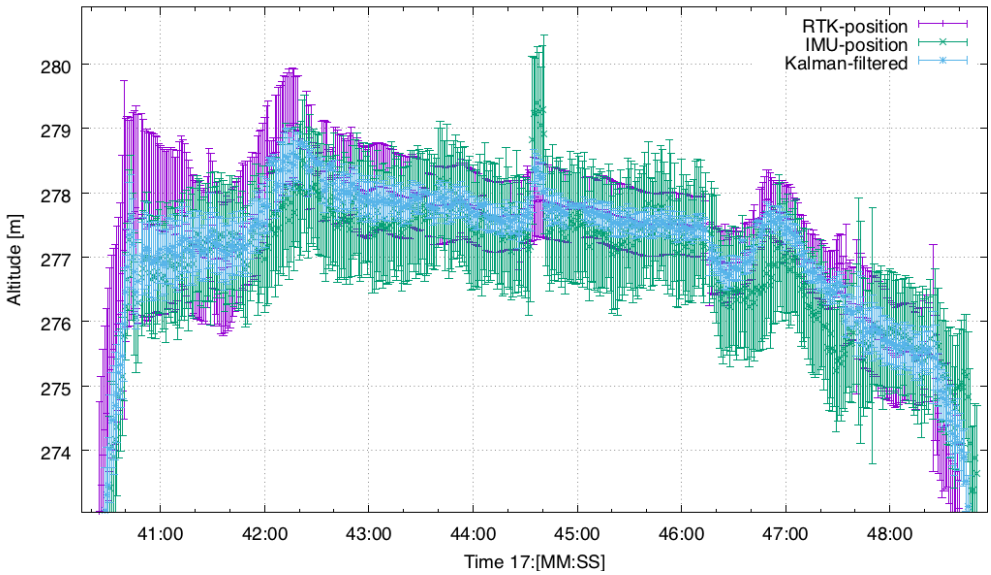

Figure 4.21: Zoom into Fig. 4.20 when the rover was taken out from the car on the hill.

In Fig. 4.21, the signals and filtered altitudes are illustrated for the time on the hill, where one can better see the variations of standard deviations and accuracy of the Kalman-filter approach. The filtered standard deviation could be decreased to $\sigma_k \approx 0.25\,m$. The reason for the peak of the IMU measurement at 17:44:40 is not clear. A wind gust is not the reason, as the peak would not point upwards but

downwards. Also to emphasize is that the peak is stable for almost 15 s. It shifts the Kalman-filtered position up to about one meter, which is significantly bad and should be corrected.

Field measurement

In another measurement, the more realistic scenario of walking on a field was executed. The pathway is illustrated using the application Google Earth and represented in Fig. 4.22. At the top center one can see the reference position, which is the location of the base station and also the starting point of the measurement. The procedure was a slow walk, where the rover was not held on a fixed altitude continously.

Figure 4.22: Google Earth view of the measurement scene which is a field with a straight horizontal road.

In Google Earth it is possible to zoom in and represent the measured values from all directions. This simplifies the evaluation and makes it more overseeable. The measurment scenario from Fig. 4.22 is presented in side view in Fig. 4.23.

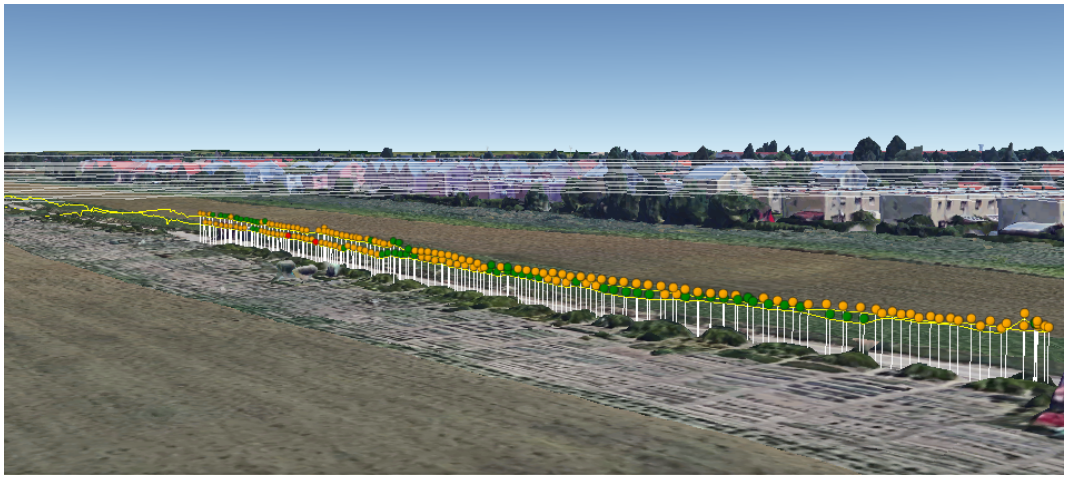

Figure 4.23: Google Earth side view of the measurement scene on the field. Delineated are the changing RTK altitude measurements.

The results and the comparison of altitude measurements calculated through RTK and pressure are represented in Fig. 4.24. The filtered signal is depicted as the blue points combined with the orange line.

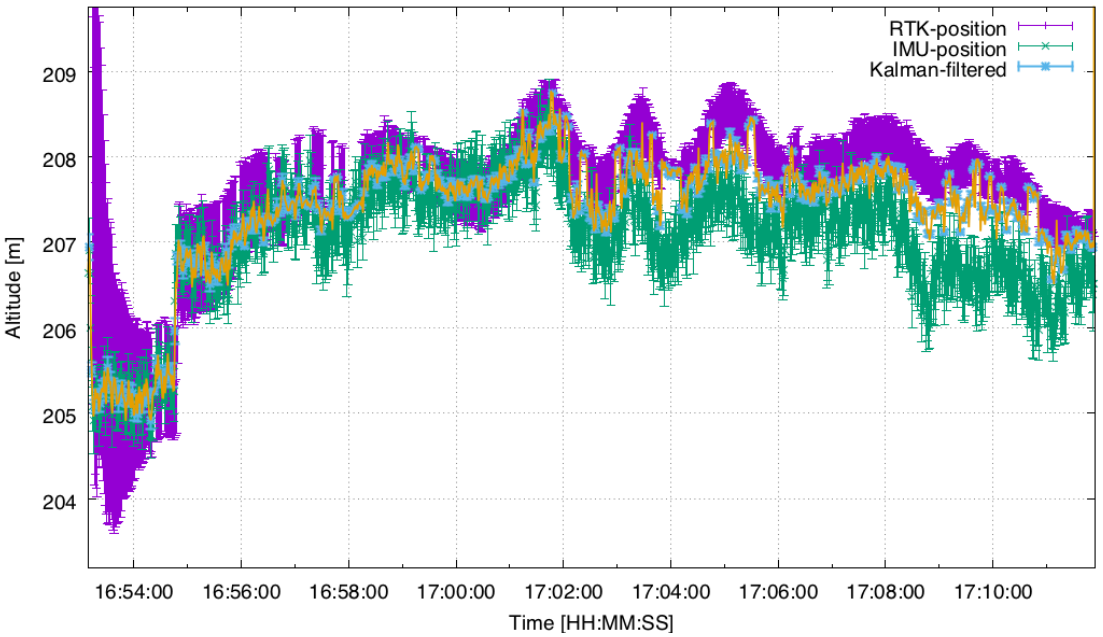

Figure 4.24: Comparison of RTK-, pressure- and Kalman filtered signal on a straight line walking test.

As it is shown in the graph, the inital time to find the position of the rover was again about 3 min. Then a sudden altitude increase was measured by both of the sensors, the RTK system and the pressure sensor, induced by grabing the rover

from the ground. Until around 17:02 the signals were almost identical, but then, abruptly, an offset gets in and the IMU delivers smaller altitudes in the range of 1 m. As for the standard deviations of the Kalman filter only the deviations of the measured signals are relevant and a random error is not included, such an incident can worsen the evaluation very much. An assumption is that the RTK followed a wrong position, because of an occuring cycle slip and, therefore, a lost of lock appeared. Then, it found a wrong lock on another altitude. Also, there are huge oscillations in the filtered signal, because as soon as the RTK evaluation has found a fix, the standard deviations get increasingly small and therefore the filter believes the RTK measurement a lot more.

4.4.1 Back projection

The completed system was tested in a field photographing an advertismend board. It was a mostly horizontal field with no obstructions around. Therefore, accurate and strong GNSS signals were expected. The rover, as it is shown in Fig. 3.6, was moved along the line shown in Fig. 4.25, starting at the bottom. Again, at the beginning of the measurement, the blue circles which respresent the standard deviations (σ) were big, but decreased to $\sigma \approx 25\,cm$ for most of the time. This was the best value, which could constantly be reached for the moving rover in the scope of this work.

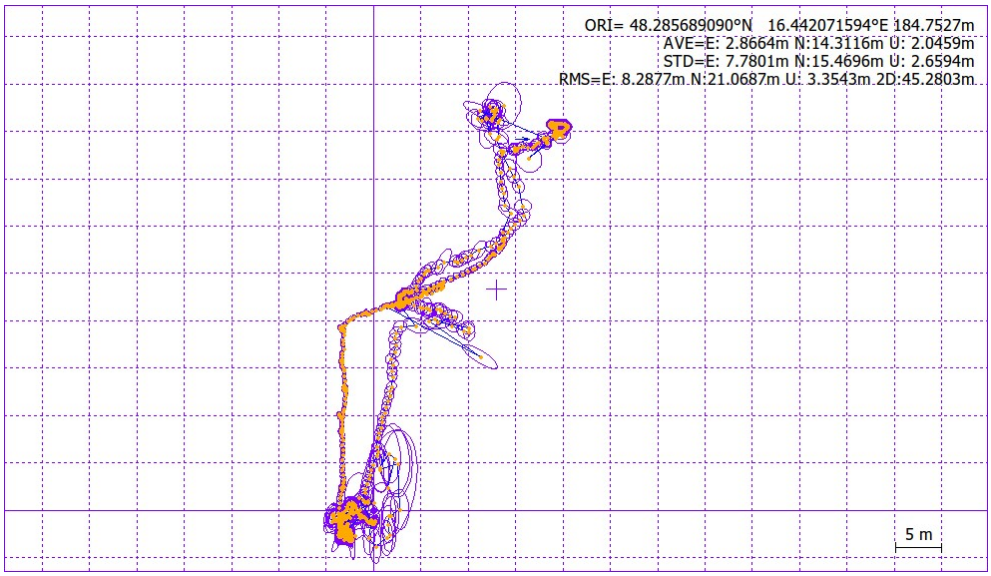

Figure 4.25: The path of the field experiment, when taking pictures of the advertisment board which is located at the delineated cross in the middle.

The altitude evaluation and the Kalman filtering delivered the results shown in Fig. 4.26. The altitude is plotted as a function of time.

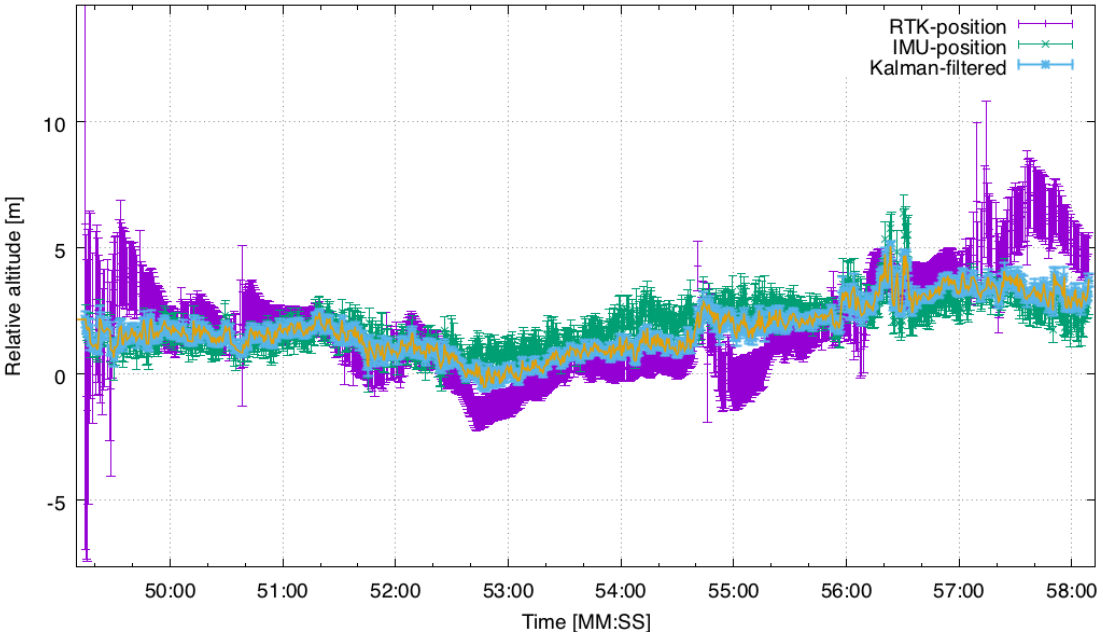

Figure 4.26: Altitude measurements using RTK and the pressure sensor. Furthermore, the Kalman filtered signal is represented as the orange line with its standard deviations in blue.

As it was the lowest point on measurement path, it does not make any sense that the RTK outputed a negative altitude in the time frame of 52:30 and 53:30. As it believed that the rover was at a negative altitude compared to the base station, which is not possible, and meanwhile still not increased the standard deviations enough, the Kalman filter follows it and worsens the measurement a lot. At the time of 56:30 there is another strange behaviour, as the RTK suddenly jumps up from 2.5 m to almost 5 m and at the same time also the pressure values started oscillating. Following also the filtered signal to oscillating strongly. The RTK signal then even started to drift up and away, but as the deviations increased, the filter was able to correct that.

Pictures were taken all along the path, but the backprojection did not produce acceptable images for all of them. In Fig. 4.27, the first part of the path is depicted, where the green and blue vectors indicated the unit vectors in the global system, calculated by the magnetic and the gravitational field. After projection of the local coordinate system to the global system, the rover knows how it is orientated in the field. The black line with its middle at (10,20) is the advertisment board to which direction the camera was pointed when taking the pictures. It was tried to move slowly and wait for around three seconds on the spot when taking a picture to guarantee accurate GNSS positions.

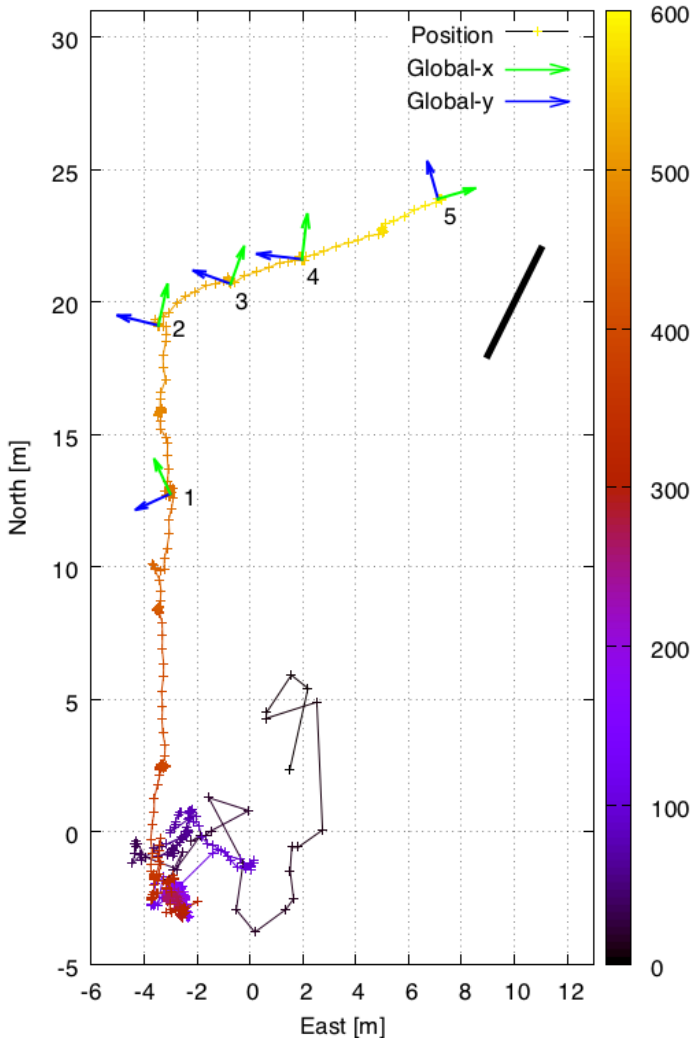

Figure 4.27: The measurement path, where the green and blue unit vectors indicate where the camera was pointing when taking a picture.

Table 3 indicates which picture corresponds to which location depicted in the graph of Fig. 4.27.

Table 3: The measured locations of where to pictures were taken.

Marks in Fig. 4.27	Fig.
1	4.32
2	4.29
3	4.30
4	4.28
5	4.31

The following figures represent the raw pictures as a comparison with the back-

projected images to the defined plane. The advertisment board is of the size $504\,cm \times 238\,cm$. The size of the indicated red squares is $50\,cm \times 50\,cm$, these serve as indicators if the backprojection was performed correctly. The ideal results would have been perfectly aligned and turned advertisment posters to a correct angle in respect to the camera and placed on the defined plane at the same spot with the exact same magnification for every picture.

(a)

(b)

Figure 4.28: (a) Original picture when the camera was tilted about 45°. (b) The rotation of the tilted picture worked fine, but the projection to the plane is too far away.

(a)

(b)

Figure 4.29: Again the rotation worked pretty well and the projected image looks similar to Fig.4.28, but the distance is overestimated a lot. Comparing the projection with the red grid, an amplification factor of about two is missing in width and height.

(a)

(b)

Figure 4.30: The closer one gets, the better it works to adjust the images, but still, the distance is overrated. This is not because of an GNSS issue, but probably because of an error in the evaluation code.

(a)

(b)

Figure 4.31: The only picture where the magnitude of the defined plane comes close to the projected pictur at a distance of $\approx 5\,m$.

(a)

(b)

Figure 4.32: Picture from further away. The backprojection delivered a highly distorted image, but the tilting worked fine. Again, the distance is much overrated and the grid of the defined plane does not match with the projection.

The rotation of the pictures worked well, as the orientation of the rover could be calculated precisly by using the magnetic- and gravitational field to define a coordinate system. Also, the GNSS delivered good results, but the distance was overrated continuously for the pictures, unless the rover was very close to the advertisment board. A lot more pictures were taken to test the system and it was seen, that when the camera is tilted more than 75°, the GNSS signals worsens significantly, therefore, the position and the altitude measurements get much more inaccurate. Fast movements and vibrations also worsen the measurements, that was why the rover was held still at a new spot for some seconds, before taking another picture. It has to be said that vibrations introduced by wind are much more significant than just walking or quick movements.

5 Discussion

The implemented RTK-DGNSS system delivered highly accurate results when both the base station and the rover were held stationary. The standard deviations of a fixed location measurement could be decreased from $\sigma_{x,GNSS} = 1.173\,m$ and $\sigma_{y,GNSS} = 1.682\,m$ for the conventional GNSS measurement to $\sigma_{x,RTK} = 0.0050\,m$ and $\sigma_{y,RTK} = 0.0046\,m$ for the implemented RTK system. This is equivalent to an enhancement factor higher than 200, which is a good result. Unfortunately, very accurate results like these could only be achieved when the rover was on the ground and not moved. As soon as it was moved, the standard deviations of position measurement increased, but was still in the range of 40 cm for the horizontal position. On the other side, the altitude measurements really suffered from moving and the standard deviations increased to nearly 80 cm. Several tests were performed when the rover was carried around and it became clear that the accuracy of the GNSS measurement really depends on the continuity of the signals. GPS- and GLONASS satellites deliver equally good signal. Cycle slips worsen the position measurement accuracy noticeably.

Several undergrounds like concrete, gras, and metallic undergound shielding plates were tested on amount of appearing cycle slips, where the copper plate produced the best results. From an electrodynamical point of view, all metallic plates should have been leading to similar results. High frequency electromagnetic fields can only be shielded by fully closed covers, as electromagnetic waves will always diffract around edges of shieldings. Potentially, the size of the aperture where the cable of the GNSS sensor was put through to connect it to the microcontroller was an issue, considering a possible penetrativeness of the electromagnetic field. The main intensity of the electric field is shielded, as the extent of the aperture does not exceed the half wavelength, but because of the induced current on the plates is flowing around the aperture, electric fields corresponding to that of dipols or multipoles could emerge. It is noteable that the pattern of a dipole and that of the slot is the same. The smaller the aperture the better, but potentially the length of it should not be higher than a fiftieth of the wavelength, what was exceeded in terms of the design of both, base-station and rover [44].

Another point, which has to be mentioned, is the time to a position fix, which is around three minutes. IThe system initially needs to solve the ambiguity problem. Fortunately, this is not a big downside, but has to be considered for measuring in the field. The fastest way to get a position fix is to choose the option of static-start in the post processing tool of RTKLIB, so the system can identify different disturbences. The problem is that in case of the applied post-processing workflow it is not possible to see if the system already found a fix. So it can happen that one starts to measure and take pictures too early and the rover will lock on a false fix, what can worsen the measurements strongly.

The attempt of integrating the acceleration twice to calculate the new position worked only for very small timespans after an verification factor was introduced checking for fallacious signals. A drifting offset signal introduced by the gyroscope is difficult to handle. If the method of resetting new normalized systems is used too frequently, acceleration information is lost. However, it was not good enough to use it for an additional Kalman filter to correct the position measurement by RTK.

The Kalman filter was implemented for the altitude measurement, where the altitude signal from the RTK measurement was updated with the calculated altitude signal from pressure data. The accuracy could be increased by a factor of 2-3 as it is shown, for example, in Fig. 4.21. The filtered signal reviews the standard deviations and trusts either the RTK or the pressure data more. Through this way, high fluctuations of the filtered signal can be avoided. Nevertheless, if the signal suddenly increases, as it was the case in Fig. 4.21 at the time of 17:44:40, the filtered signal follows and an error of 1 m was produced. This should be prevented with some additional code. The reason for the peak is not clear, but probably was introduced by some internal error, as it was only stable for 10 s and droped to the initial position again. It also is conceivable that the peak was produced by a lasting wind gust or a passing high pressure area respectively.

The Kalman filtered solution shown in Fig. 4.24 delivered good results for the start of the measurement, but as the RTK-position and the IMU-position started to drift apart, the Kalman-filtered signal was not very stable anymore. Potentially, the signals were drifting away from each other, because the RTK system was locked on a false fix. Also it is conceivable that it was because of an air pressure variability, which can already lead to altitude miscalculations up to 2 m after 15 min, as it is shown in Fig. 3.11. These variabilities can be subtracted by using the data from the base station, but it can not be guaranteed that the pressure sensor from the base station and the rover will always produce high correlating results. The good thing is that the Kalman filter still produced acceptable results, as it is assumed that the real altitude is somewhere between the two lines on the same value, like it was at the start of the measurement, because of the flat field. Comparing the result with the low hysteresis curve from Fig. 3.4, it is noteable that the correlation of the two different pressure sources was very high driving up the hill, but for coming down the IMU source delivered higher values then the Kalman source in the range of 2-5 m, which is also an imaginable error source.

The backprojection method was tested on a field by taking pictures of an advertisment board and backprojecting them to a defined plane, by using RTK position- and IMU orientation measurements. The method worked as long as the distance from the photographed object was not too far. Rotated pictures were projected to correct orientations, but the magnification factors were probably not calculated

correctly, that is why most of the pictures were not projected to the desired size. It was figured out that the rover must not be tilted more than 75°. This is due losses of satellites, because the antenna was not pointed upwards anymore and therefore had a smaller sky view.

In conclusion, the low cost system can be used to get precise position- and orientation tracks of the rover, but unfortunately loses a lot of its accuracy when moving around. To achieve higher stability, external antennas for both, base station and rover, could already increase the precision a lot. Also, the magnetic sensor is quite failure-prone and interacts with electromagnetic stray radiations. The acceleration sensor delivered good results, is very much stable and serves as an ideal source to define the z-direction of the local coordinate system. Unfortunately, its sudden deviations are too high to use it as a navigation tool by integrating its signals. The gyroscope can be integrated to measure the orientation of the rover.

6 Conclusions

To perform carrier-phase and pseudorange measurements, there are only a few low-cost GNSS receivers available. The Ublox NEO-M8T is another chip from the same generation of the NEO-M8 series, which is slightly more expensive at a price of around 50 $, but especially designed for the purpose of RTK measurements. Because this sensor, not like the NEO-M8N used for this work, is specifically constructed for these measurements, it should perform better. Also, it is capable of receiving raw Galileo data, which could be an advantage, as they will be state-of-the-art satellites providing strong signals and also because more available satellites are always better. It would be beneficial to test it and check if it has a reduced amount of cycle slips. There is even another sensor of the same series, the NEO-M8P, which already has a built-in RTK solution, however it is pretty expensive, starting at a price of about 250 $. Also, there are external antennas available which are probably capable of increasing the signal strenght and reducing cycle slips. As these are available starting at a price of 20 $ it would of course make sense to test them as well.

The design of the rover could be reconsidered, as strong wind gusts can lead to oscillations of the shielding plate, which could downgrade the evaluation. The problem is that the GNSS chip should not be mounted directly on the side of the camera, as the camera itself could disturb the measurement. An external antenna attached on top of the camera might be the solution. Moreover, an external antenna could guarantee the best possible sky view at any time. What's more, also the design of the base station should be thought over as it would make sense to make it much more stable against wind gusts. Therefore, it would be conceivable to exchange the plastic box with a box of wood, or just to place some weights on the bottom of the box under the sensor.

Another approach could be to use the commercial Austrian Positioning Servies (APOS) as reference stations, instead of the self-built base station used for this work. The benefits are that the locations of the reference stations are measured higly accurate and that they use high-quality sensors. A disadvantage may be that the 35 reference stations do not cover the entire area of Austria and the quality of the evaluated position with DGNSS decreases with distance to the reference stations [45].

A prospective step could be to mount the system on a drone, which then undertakes the task to fly over the PV plants and takes thermographic pictures. Defect modules can be identified pretty easily. There are already a few companies offering PV inspections by drones, the drawbacks are that everything has to be performed manually and the analysis of the modules is only a rough one. A measurement system like the one developed in this work could increase the accuracy of those systems. Also it is possible to automatise these measurements even more and let a drone fly

on accurately defined paths over the PV plants. After the drone is finished with taking images and arrives at the base station, all the data could be evaluated more automatized. As drones become less expensive each year and the process of high precission GNSS analysis and inertial navigation can be performed with low cost components, as it was shown in this work, future combined drone systems could help to achieve long-term outputs of PV plants on a high level.

References

[1] Renewable Energy Policy Network for the 21st Century. *Renewables 2016 - GLOBAL STATUS REPORT*. Technical report, REN21, 2016.

[2] Peter Biermayr, Manuela Eberl, Monika Enigl, Hubert Fechner, Christa Kristöfel, Kurt Leonhartsberger, Florian Maringer, Stefan Moidl, Christoph Schmidl, Christoph Strasser, Werner Weiss, Elisabeth Wopienka. *Innovative Energietechnologien in Österreich - Marktentwicklung 2014*. Technical report, Bundesministerium für Verkehr, Innovation und Technologie, 2015.

[3] Brian Kahn. Scientific american - climate central. *What 4 Million Solar Panels Look Like from Space*, 2017.

[4] Wircon GmbH. *Approximately 61-megawatt solar park the foundation for further projects in Denmark*. https://wirsol.com/en/, 2016.

[5] Antonio Luque, Steven Hegedus. *Handbook of Photovoltaic Science and Engineering*. John Wiley & Sons Ltd, 2003.

[6] Swapnil Tiwari and G. N. Dubey. *Fundamentals of Photovoltaic Modules and their Applications*. RSC Pubslishing, Indian Institute of Technology (IIT) New Delhi, India, 2010.

[7] Salahuddin Qazi. *Standalone Photovoltaic (PV) Systems - For Disaster Relief and remote Areas*. Elsevier Inc., State University of New York Polytechnic Institute, Utica, NY, United States, 2017.

[8] Reinhold Bertlmann, University of Vienna. *Script: Theoretical physics 2 (Quantum physics)*. http://homepage.univie.ac.at/reinhold.bertlmann/pdfs/T2_Skript_Ch_4.pdf, 2017.

[9] National Instruments Ges.m.b.H. *Theorie zur Charakterisierung von Fotovoltaikzellen mittels Strom-Spannungs-Kennlinie*. http://www.ni.com/white-paper/7230/de/, 2009.

[10] Samlex America Inc. *Solar (PV) Cell, Module, Array*. http://www.samlexsolar.com/about/default.aspx, 2017.

[11] Solarinvert GmbH. *Reihen- und Parallelschaltungen von Solarzellen*. http://www.solar.lucycity.de/index.php/reihen-und-parallelschaltung.

[12] Pantelis N. Botsaris and John A. Tsanakas . *Infrared Thermography as an Estimator Technique of a Photovolta Module Performance via operating Temperature Measurements*. Democritus University of Thrace, School of Engineering, Greece, 2017.

[13] Carosena Meola, Simone Boccardi and Giovanni Maria Carlomagno. *Infrared Thermography in the Evaluation of Aerospace composite materials*. Woodhead Publishing (Imprint of Elsevier), 2017.

[14] Bernhard Kubicek. *Private correspondence*. AIT - Austrian Institute of Technology, 2017.

[15] Oliver J. Woodman. *An introduction to internal navigation*. Technical report, University of Cambridge, August 2007.

[16] Rob O'Reilly, Kieran Harney and Alex Khenkin. *Sonic Nirvana: MEMS Accelerometers as Acoustic Pickups in Musical Instruments*. Analog Devices Inc., http://www.analog.com/articles/mems-accelerometers, 2009.

[17] Lisa Jogschies, Daniel Klaas, Rahel Kruppe, Johannes Rittinger, Piriya Taptimthong, Anja Wienecke, Lutz Rissing and Marc Christopher Wurz. *Recent Developments of Magnetoresistive Sensors for Industrial Applications*. Sensors (Basel, Switzerland) http://www.mdpi.com/1424-8220/15/11/28665, 2015.

[18] Dunzhu Xia, Cheng Yu and Lun Kong . *The Development of Micromachined Gyroscope Structure and Circuitry Technology*. Sensors ISSN 1424-8220 https://www.ncbi.nlm.nih.gov/pmc/articles/PMC3926620/, 2014.

[19] Collin Wells Peter Semig and Miro Oljaca. *Design tips for a resistive-bridge pressure sensor in industrial process-control systems*. Analag Applications Journal, http://www.electronics-tutorials.ws/blog/wheatstone-bridge.html, 2015.

[20] Tim Stombaugh, Doug McLaren, and Ben Koostra. *The Global Positioning System*. University of Kentucky - College of Agriculture, 2005.

[21] Paul D. Groves. *Principles of GNSS, Inertial, and Multisensor Integrated Navigation Systems*. Artech House, 2008.

[22] Nicola Crocetto, Folco Pingue, Salvatore Ponte, Giovanni Puglianoa and Vincenzo Sepe. *Ionospheric error analysis in GPS measurements*. Dipartimento di Ingegneria Civile, Seconda Università di Napoli, Aversa (CE), Italy, 2008.

[23] Ying D. Liu, Janet G. Luhmann, Primož Kajdič, Emilia K.J. Kilpua, Noé Lugaz, Nariaki V. Nitta, Christian Möstl, Benoit Lavraud, Stuart D. Bale, Charles J. Farrugia and Antoinette B. Galvin. *Observations of an extreme storm in interplanetary space caused by successive coronal mass ejections*. Nature Communications 5, Article number: 3481, 2014.

[24] Ralf Drescher. *Präzise und echtzeitnahe Positionierung in einem Mixmode-GPS-Netz mit großen Höhenunterschieden*. Schriftenreihe Fachrichtung Geodäsie Fachbereich Bauingenieurwesen und Geodäsie Technische Universität Darmstadt, ISBN 978-3-935631-27-3, 2013.

[25] Paul Collins and Richard B. Langley. *Tropospheric delay: Prediction for the WAAS User*. University of New Brunswick, 1999.

[26] Josua Stähli and Stefan Keller. *Präzise Positionsbestimmung mit Low-Cost-GPS und Postprocessing*. Hoschschule für Technik Rapperswil HSR, 2013.

[27] Leica Geosystems AG. *Einführung in die GPS Vermessung (Global Positioning System)*. Heerbrugg (Switzerland), 2000.

[28] QLS Henri B. Ayers CLS. *GNSS (GPS and GLONASS) Positioning used in Land Surveying and Engineering*. Leica Geosystems, 2011.

[29] P. J. G. Teunissen. *Least-Squares Estimation of the Integer GPS Ambiguities*. Delft Geodetic Computing Centre (LGR) Department of the Geodetic Engineering Delft University of Technology, 1993.

[30] Paul de Jonge and Christian Tiberius. *The LAMBDA method for integer ambiguity estimation: implementation aspects*. Publications of the Delft Geodetic Computing Centre, 1996.

[31] Malek O. Karim et al. *Innovation: Cycle Slips, Detection and Correction Using Inertial Aiding*. GPS World: http://gpsworld.com/innovation-cycle-slips/, 2014.

[32] Rudolph Emil Kalman. *A New Approach to Linear Filtering and Prediction Problems*. Transactions of the ASME–Journal of Basic Engineering, 1960.

[33] R. E. Kalman and R. S. Bucy. *New Results in Linear Filtering and Prediction Theory*. Transactions of the ASME–Journal of Basic Engineering, 1961.

[34] Dipl.-Ing. Enrico Kurtenbach. *Entwicklung eines Kalman-Filters zur Bestimmung kurzzeitiger Variationen des Erdschwerefeldes aus Daten der Satellitenmission GRACE*. PhD thesis, Institut für Geodäsie und Geoinformation der Universität Bonn, 2011.

[35] Peter S. Maybeck. *Stochastic models, estimation, and control*, volume 141 of *Mathematics in Science and Engineering*. 1979.

[36] G. Welch and G. Bishop. *An Introduction to the Kalman Filter*. University of North Carolina - Department of Computer Science, 2001.

[37] P. A. Bromiley. *Products and Convolutions of Gaussian Probability Density Functions*. School of Medicine, University of Manchester, 2014.

[38] SparkFun Electronics. *Serial Communication*. https://learn.sparkfun.com/tutorials/serial-communication, 2017.

[39] SparkFun Electronics. *I2C*. https://learn.sparkfun.com/tutorials/i2c, 2017.

[40] Tomoji Takasu. *RTKLIB: An Open Source Program Package for GNSS Positioning.* Tokyo University of Marine Science and Technology http://www.rtklib.com/, 2013.

[41] David G. Lowe. *Distinctive Image Features from Scale-Invariant Keypoints.* Computer Science Department University of British Columbia, 2004.

[42] Erich Hartmann. *Computergestütze darstellende und konstruktive Geometrie.* Technische Universität Darmstadt, 1998.

[43] Wolfgang Hugemann. *Correcting Lens Distortions in Digital Photographs.* Ingenieurbüro Morawski + Hugemann, 2010.

[44] Delaware Water Gap PA Ron Brewer, Laird Technologies. *Design Considerations for Minimizing Large Aperture Effects in Shielding.* Item Media https://interferencetechnology.com/design-shielding, 2002.

[45] APOS Austrian Positioning Service. *Datenerfassung und -verarbeitung.* http://www.bev.gv.at/portal/page?_&_schema=PORTAL, 2017.

List of Figures

List of Tables